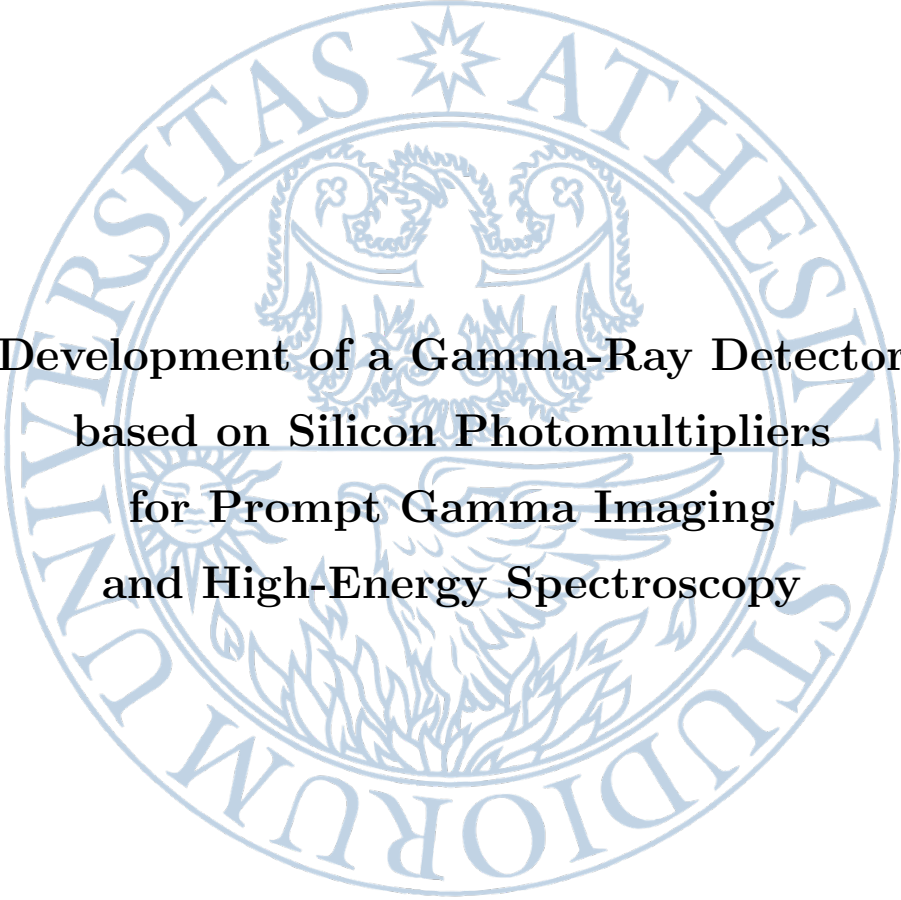UNIVERSITY OF TRENTO
DEPARTMENT OF PHYSICS
DOCTORAL PROGRAMME IN PHYSICS

# Development of a Gamma-Ray Detector based on Silicon Photomultipliers for Prompt Gamma Imaging and High-Energy Spectroscopy

Doctoral Dissertation of:

**Veronica Regazzoni**

Supervisor:

**Dr. Alberto Gola**

2017 – XXX Cycle

# Development of a Gamma-Ray Detector based on Silicon Photomultipliers for Prompt Gamma Imaging and High-Energy Spectroscopy

Thesis submitted to the Doctoral Program in Physics in partial fulfillment of the requirements for the degree of *Doctor of Philosophy in Physics* by

**Veronica Regazzoni**

Examination Committee:

**Prof. Dr. Carlo Ettore Fiorini** (Politecnico di Milano)

**Dr. Gabriela Llosá Llácer** (Universitat de València)

**Dr. Lucio Pancheri** (University of Trento)

December 2017

*To my parents.*

*To my beautiful...*
*...beautiful hubby!*

# Abstract

Proton therapy is a recent type of radiotherapy that uses high-energy proton beams, and more recently carbon ion beams, to benefit of their physical selectivity. The energy deposited by these particle beams is inversely proportional to their velocity. Therefore they release most of the energy at the end of their path into the tissue. The energy is deposited in a few millimeters, in a zone called the Bragg peak. Before and after the Bragg peak the energy deposition is minimal. The depth and the width of the Bragg peak depends on the beam energy and on the density of tissues located along the beam path. By setting the beam energy, the Bragg peak can be positioned in the tumor site, avoiding the healthy tissues. Because of the sharpness of the Bragg peak zone, proton therapy is advantageous for tumors located near to important body part, such as the brain, spine, and neck. The drawback is that small uncertainties on particle range can have a serious impact on treatment and limit the efficiency of the proton therapy.

To obtain more effective treatments in proton therapy real-time range verifications are necessary to perform on-line corrections of the delivered treatment. Among different techniques presented in the literature, positron emission tomography (PET) and prompt gamma imaging (PGI) are the most promising methods for *in vivo* range verification. PET and PGI are indirect approaches to measure protons penetration depth inside patients because they aim to detect secondary particles resulting from the interaction between proton beams and tissue nuclei. PET imaging detects coincidence gamma rays due to the production of positron emitters and requires some minutes to achieve enough statistics to have a sufficient signal to noise ratio. PGI instead uses prompt gamma rays generated by de-excitation of target nuclei; the quantity of these rays and their temporal emission (few nanoseconds) allow to perform a range verification during treatment with the PGI. Several research groups are evaluating different approaches to realize a prompt gamma imaging system suitable

for the use in clinical condition and the optimization of a gamma-ray detector for PGI is still ongoing.

The Gammarad project works in this direction and aims to develop an high-performance and solid-state gamma ray detection module (GDM) with a slit camera design. The project is based on a collaboration among Fondazione Bruno Kessler (FBK, Trento, Italy), Politecnico di Milano (Milano, Italy), the Trento Institute for Fundamental Physics and Applications (TIFPA, Trento, Italy ), and the Proton Therapy Center of Trento (Italy). The project is divided into two parts. The first part focuses on the technological development of a gamma-ray imaging module. This module is composed by a gamma-ray detector, based on a solid-state silicon sensor, and an integrated circuit. They are assembled into a compact module with data and control systems. The second part of the project will be dedicated to the experimental validation of the system both in laboratory with radioactive sources and in a real environment, that of proton therapy.

The most innovative part of the gamma-ray detector developed for the project is the photo-sensor used for the scintillation light readout. In traditional applications it is a photomultiplier tube (PMT). However, in recent years, Silicon Photomultiplier (SiPM) has become increasingly popular in a variety of applications for its promising characteristics. Among them, current-generation SiPMs offer high gain, high Photon Detection Efficiency (PDE), excellent timing performance, high count-rate capability and good radiation hardness. Due to these characteristics they are used as PMTs replacement in several applications, such as in nuclear medicine (PET), in high-energy physics (calorimeters), astrophysics (Cherenkov telescopes) and in others single-photon or few-photon applications.

For its characteristics, the SiPM is also very promising for the scintillator readout in prompt gamma imaging and in high-energy gamma-ray spectroscopy. Detectors for these applications must be compact, robust, and insensitive to the magnetic field. They have to provide high performance in terms of spatial, temporal, and energy resolution. SiPMs can satisfy all these requirements but typically they have been used with relatively low energy gamma rays and low photon flux, so manufacturers have optimized them for these conditions. Because of the limited number of micro-cells in a standard SiPM, 625 cells/mm$^2$ with 40 $\mu$m cells, the detector response is non-linear in high-energy conditions. Increasing the cell density is extremely important to improve the linearity of the SiPM and to avoid the compression of the

energy spectrum at high energies, which worsens the energy resolution and makes difficult the calibration of the detector. On the other hand, small cells provide a lower Photon Detection Efficiency (PDE) because of the lower Fill Factor (FF) and as a consequence a lower energy resolution. Summarizing, the energy resolution at high energies is a trade-off between the excess noise factor (ENF) caused by the non-linearity of the SiPM and the PDE of the detector. Moreover, the small cell size provides an ultra-fast recovery time, in the order of a few of nanosecond for the smallest cells. A short recovery time together with a fast scintillator such a LYSO, reduces pile-up in high-rate applications, such as PGI.

Based on the above considerations, the aim of this thesis is to develop an optimized gamma-ray detector composed of SiPMs for high-dynamic-range applications, such as the scintillation light readout in prompt gamma imaging and in high-energy gamma-ray spectroscopy. SiPMs evaluated for the detector are High-Density (HD) and Ultra-High-Density (UHD) SiPM technologies recently produced at Fondazione Bruno Kessler (FBK). Instead of standard SiPMs, HD and UHD SiPMs have a very small micro-cell pitch, from 30 $\mu$m down to 5 $\mu$m with a cell density from 1600 cells/mm$^2$ to 46190 cells/mm$^2$, respectively.

HD SiPMs are produced using a lithography technology with smaller critical dimensions and designed with trenches between SPADs. Small cells have a lower gain, which helps to reduce correlated noise, such as after-pulse and cross-talk. The trenches provide an optical and electrical cell isolation, and a smaller dead border around cells increasing the fill factor (FF) and thus limiting Photon Detection Efficiency (PDE) losses. UHD SiPMs push the limits of the HD technology even further, by reducing all the feature sizes, such as contacts, resistors, and a border region around cells. UHD SiPMs have hexagonal cells in a honeycomb configuration that generate a circular active area and a dead border around cells lower than 1 $\mu$m. The reduction of this dead border can improve the FF in smaller cells although FF usually decrease as cell size decreasing. It is necessary understand how these significant layout changes affect the optical properties of SiPMs to evaluate which SiPM technology provides best performance in high-energy gamma-ray applications.

In the first part of the thesis, we present the characterization of HD and UHD SiPM technologies in terms of PDE, gain, dark count rate, and correlated noise for the cell sizes between 30 and 7.5 $\mu$m. The most important markers of SiPM performance in gamma-ray spectroscopy are however the energy resolution and the lin-

earity when coupled to the scintillator for the detection of high-energy gamma-rays. A typical characterization of the energy resolution of SiPMs, coupled to scintillator crystals, is performed with radioactive source of up to 1.5 MeV. However, PGI features gamma ray-energies of up to 15 MeV which are not easily provided by the usual laboratory calibration sources. Extrapolating the behaviour of the detector from the "low" energy data is not correct and leads to unreliable data for calibration and performance estimation. Therefore, we developed a novel setup that simulates the LYSO light emission in response to gamma photons of up to 30 MeV. A LED (emitting at 420 nm) is driven by a pulse generator, emulating the light emitted by a LYSO scintillator when excited by gamma rays. The pulse generator parameters (amplitude, duration, rise and fall time constants) are adjusted so that photons emitted by the LED match the intensity and time distribution of the LYSO emission. The number of photons in each light pulse is calibrated from measurements at 511 keV obtained with a $^{22}$Na source and a LYSO crystal coupled to the SiPMs. Using this LED setup we characterized the energy resolution and non-linearity of HD and UHD SiPMs in high-energy gamma-ray conditions. The second part of the thesis provides a detailed description of the scintillator setup and of the setup for the simulation of high-energy gamma-ray response, followed by the results of the characterization performing with these setups.

Summarizing the results, the lowest non-linearity is provided by the technology with highest cell density, the RGB-UHD. For the 10 and 12.5 $\mu$m-cells, we obtained values of 4.5% and 5% respectively, at 5 MeV and 6 V over-voltage. On the other hand, we measured the best energy resolution for the largest SiPM cells, without the intrinsic term of the scintillator crystal, i.e. 2.6% for the 20 $\mu$m-cell and 2.3% for the 25 $\mu$m-cell, at 5 MeV and 6 V over-voltage. This is due to the dependence of the energy resolution on the PDE, which increases with the size of the SiPM cell. Optimal performance of the detector in high-dynamic-range applications, which depends on the several SiPM parameters, such as excess noise factor, photon detection efficiency, and cell size of the SiPM, is a trade off between non-linearity and energy resolution. At 5 MeV, the best trade-off for prompt gamma imaging application is obtained with the 15 $\mu$m-cell. At 10 MeV the 12.5 $\mu$m-cell provides the best trade-off, because of the higher number of photons emitted by the scintillator. In addition, it was possible to distinguish the different components of the energy resolution (intrinsic, statistical, detector and electronic noise) as a function of cell size,

over-voltage and energy, by combining the results of the scintillator and LED setups. The estimation of the intrinsic contribution of the scintillator crystal, coupled to the HD SiPMs, provides consistent results among the various cell sizes.

On the basis of previous characterization, HD SiPMs with dimensions of 4x4 mm$^2$ and 15 $\mu$m-cell were chosen to produce the photo-detector module of the gamma camera, optimized for an energy range between 2 MeV and 8 MeV. This module is a 8x8 array of SiPMs, which is called a tile. The production of the tile requires research on packaging techniques to solve two main challenges: the maximization of the photo-sensitive area, and the application of a protective resin transparent in the near UV to maximize light collection from the LYSO. After some R&D on packaging, we obtained a fully functional tile with 64 SiPMs with a fill factor, i.e. ratio between the photo-sensitive area and the total area, of ~86%. This fill factor is comparable to the values obtained when a Through Silicon Vias (TSVs) technique is used to connect SiPMs but without the high production cost and the additional fabrication process complexity of the TSV. It should be highlighted that packaging operations are very critical because it is necessary to produce a tile with all working SiPMs, since defective items can not be replaced in the tile. The last part of the thesis presents the packaging procedure that we have defined to produce photo-detector modules and the characterization of the photo-detector array in terms of energy resolution, position sensitive and non-linearity. The measurements on the tile were carried out jointly with the Gammarad partner of Politecnico di Milano, who provided the ASIC and DAQ for the readout. In conclusion, the R&D activity carried out during this thesis has provided the final photo-detection module with state of the art performance for high-energy gamma-ray spectroscopy to Gammarad project. The characterization of the module also shows a position sensitivity that matches the SiPM dimensions, and a proper acquisition of high-energy gamma-ray events from 800 keV to 13 MeV. This module will be tested for prompt gamma measurements in an experimental treatment room at the Proton therapy facility in Trento by the Gammarad project partners.

# Contents

# Chapter 1

# Introduction

In this chapter, we introduce proton therapy, the problem of range uncertainty, and the importance of developing an *in vivo* range control technique that can be used during a treatment. We briefly report the work carried out by several research groups on various techniques for beam monitoring. Then we focus on prompt gamma imaging and on different approaches that are currently under investigation to realize a prompt gamma imaging system. In the last part of the chapter, we present the Gammarad project and its purposes.

## 1.1   Proton therapy and range uncertainties

Radiotherapy is widely used to treat cancer patients, usually in combination with surgery or chemotherapy [1]. Radiation interacts with tissues through different mechanisms and prevents the correct cellular functioning, partially or totally, by damaging the cellular DNA. Conventional radiotherapy techniques use photon or electron beams, which have their maximum energy deposition at the surface of tissues. The dose is deposited along the entire beam path and decreases with the penetration depth in the tissues following an exponential law. For this reason, it is impossible to avoid the irradiation of healthy tissues located around the tumor. An ideal radiotherapy technique should be able to destroy cancerous tissues without damaging healthy tissues. Nowadays, tumor treatments are planned to maximize the ratio between the damage to cancerous tissues and the damage to healthy tissues located around them. An improvement in this ratio can be obtained with proton therapy.

Proton therapy is a recent type of radiotherapy that uses high-energy proton beams to benefit of their physical selectivity [2]. The energy deposited by these charged particle beams is inversely proportional to the velocity of the particles. Therefore, they release most of the energy at the end of their path into the tissue. The energy is deposited in few millimetres, in a region called the Bragg peak. Before the Bragg peak the energy deposition is minimal. The depth and the width of the Bragg peak depends on the beam energy and on the density of the tissues located along the beam path. By adjusting the beam energy, the Bragg peak can be positioned in the tumor site, avoiding the healthy tissues. Because of the sharpness of the Bragg peak zone, proton therapy is advantageous for tumors located near to sensitive anatomical structures, such as the brain, the spine, and the neck. The drawback is that small uncertainties on the particle range can have a serious impact on a treatment, limiting the efficiency and precision of the proton therapy. Fig. 1.1 (top) shows the potential dose benefit of a proton treatment compared to a photon treatment. In addition, it also shows a Spread-Out Bragg Peak (SOBP), which is generated by proton beams of different energies to cover the entire tumor preserving healthy tissues [3]. Fig. 1.1 (bottom) compares the variation in the delivered doses of a photon (left) and a proton (right) treatments in case of uncertainties due to the density heterogeneity along the beam path. This heterogeneity causes a variation
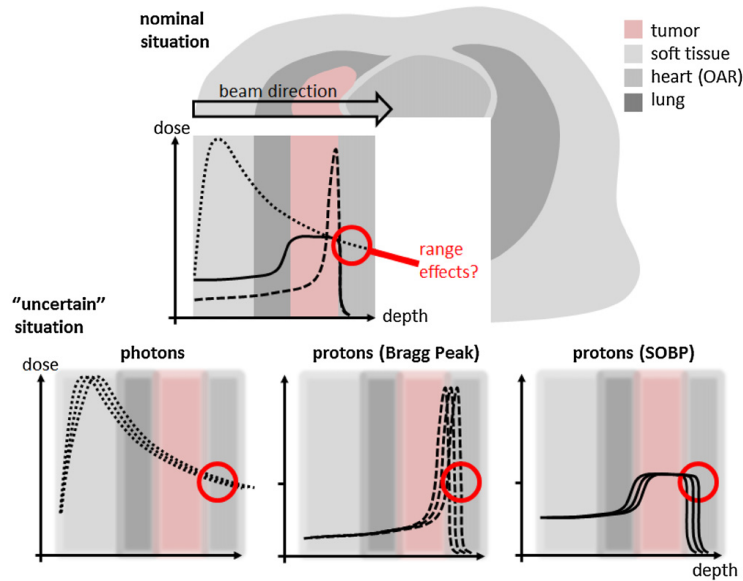
**Figure 1.1:** Top: Comparison of a depth dose curve of a photon treatment (dotted line), a depth dose curve of a mono-energetic proton treatment (dashed line), and a Spread-Out Bragg Peak (SOBP)(straight line). Bottom: influence of uncertainties on these depth dose curves. Picture from [3], reproduced by permission of IOP Publishing, all rights reserved.

on the photon dose curves after the tumor of a few percent, whereas the proton dose curves are heavily modified.

Uncertainties on the proton range can be systematic or random. The systematic uncertainties are due to the computed tomography (CT) images used to calculate the applied dose distribution. CT data could induce systematic errors since they are expressed in Hounsfield units (HU), which provide the relative attenuation coefficients of x-rays in the tissues in relation to the linear attenuation coefficient of water. To calculate the dose distribution and define the proton ranges, HU must be converted to relative proton stopping power, which describes the energy loss in the tissue by the protons as a consequence of Coulomb interactions. This conversion is based on calibration curves obtained with sophisticated algorithms and thus presents unavoidable uncertainties [4]. This conversion can introduce estimated errors of 1.1% and 1.8% in soft tissues and bones, respectively [5]. The second type of uncertainties, the random uncertainties, are instead unpredictable and can be different every day. They are caused by patient mis-positioning, organ motion (breathing), and anatomical changes of the patient (treatments usually last many weeks). These error sources can generate significant range uncertainties. Nowadays, the approach to

the range uncertainty issue is to perform a robust treatment planning by applying
generic range uncertainty margins [6]. As Fig. 1.2 shows, these margins depend on
the specific treatment scenarios and on the proton therapy facility: at Massachusetts
General Hospital they are 3.5% of the prescribed range + 1 mm, at MD Anderson
Proton Therapy Center in Houston, at the Loma Linda University Medical Cen-
ter, and at the Roberts Proton Therapy Center at the University of Pennsylvania
they are 3.5% + 3 mm, and at University of Florida Proton Therapy Institute they
are 2.5%+ 1.5 mm. The first factor takes into account the uncertainties caused by
the CT image and the unit conversion. The second factor considers the patient
setup, detection of the skin surface, and compensator design [6]. Fig. 1.2 compares
the safety margins estimated with Monte Carlo dose calculation with the applied
margins currently used in proton therapy facilities. It is clear that proton therapy
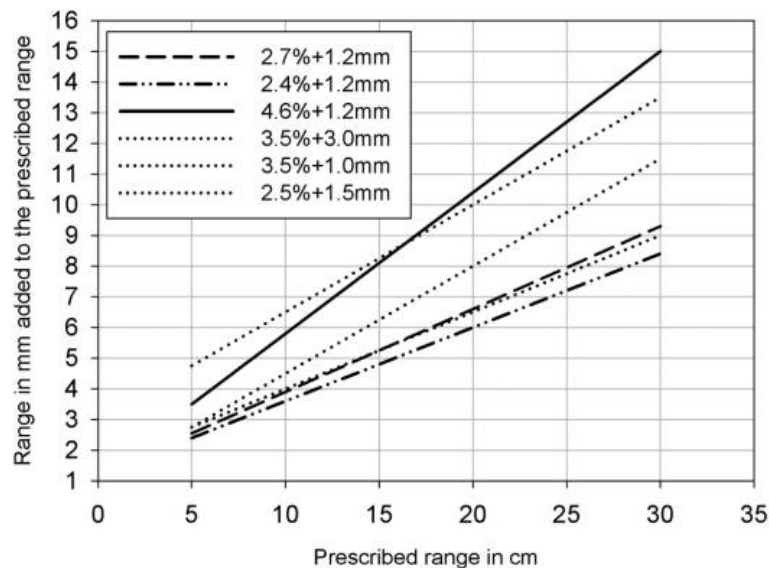facilities maintain a conservative behaviour. Simulations can be a useful tool to



**Figure 1.2:** Typically applied range uncertainty margins currently used in proton therapy facili-
ties (dotted lines) [6]. Estimated margins without (dashed and solid line) and with (dashed-dotted
line) the use of Monte Carlo dose calculation. Picture from [6], reproduced by permission of IOP
Publishing, all rights reserved.

minimize range uncertainties of proton beams inside the patient but to optimize the
precision of proton therapy [3] *in vivo* range verifications are necessary.

## 1.2   In vivo range verification

This section summirizes the different approaches to *in vivo* range verification [3]. The measurement techniques for range verification can be direct or indirect.

### 1.2.1   Direct methods

Direct methods obtain proton ranges from direct measurements of a dose or fluence, and involve implantable dosimeters, range probes or proton radiography.

Implantable dosimeters with wireless readout are used for point dose measurements. Range determination is possible because the time dependence of a delivered SOBP is unique at every point in depth. By acquiring this time dependence at a point in the patient, the residual range of the beam at this position can be obtained. This method was tested with a small ionization chamber [7] and with a semiconductor diode [8]: both detectors provided sub-millimetres precision for the proton range determination. Limits of the point dose measurement approach are a low spatial resolution, a limited number of points in which the range is verifiable, and the need to insert the dosimeter inside the target volume (possible only for few tumor types).

An alternative to the use of implantable dosimeters is the range probe concept. This method measures the residual range of a single-energy proton pencil beam that has sufficient energy to pass through the patient [9]. This approach is simple because requires only commercial detectors, such as a multiple layer ionization chamber(MLIC) [10], to measure a complete Bragg peak. The drawbacks are the necessity to use high energy protons (higher than 230 MeV), a low spatial resolution, and moreover the measured range is not the range at the tumor position but the total range through the whole patient.

Another direct method is proton radiography that provides 2D information, differently from the two previous methods. For this technique, a high energy (attenuated) proton beam is used and for each proton of the beam its entrance and exit coordinate and its residual energy are measured [11]. The main advantage in the context of range verification is that proton radiography directly provides stopping power values of the different tissues. This is very interesting for proton therapy that bases the treatment planning on these values [12], since it makes possible to eliminate the uncertainties due to the conversion of HU into stopping power, see Paragraph 1.1. Despite this advantage, the development of proton radiography is hampered by the

limited spatial resolution that can be obtained with this technique, since protons undergo to multiple Coulomb scattering. Protons, which interact with the Coulomb field of the nuclei of the materials they are passing through, are deflected with small angles that produce uncertainties in the proton trajectory reconstruction [11].

### 1.2.2 Indirect methods

Indirect methods estimate the particle range from secondary effects caused by the interaction between protons and tissues. A first type of indirect approach is based on the reconstruction of the proton range from a measurement of the secondary particles resulting from the interaction between the proton beams and the tissues in which they travel. Possible techniques of this type are PET imaging, which detects coincidence gamma rays due to the production of positron emitters [13], and prompt gamma imaging (PGI), which uses instead prompt gamma rays generated by de-excitations of target nuclei [14]. The second type of indirect method is MRI imaging, which measures the changes in the tissue after the exposition to radiations [15] and thus can be performed only after the treatment. The advantages of this method are the high spatial resolution and the possibility to use MRI scanners. A drawback is that the location of the most intense MRI signal does not correspond to the point where the highest dose was delivered. Thus, an MRI image is not sufficient to verify the proton range [16].

Range verification with PET imaging uses coincidence gammas generated by the annihilation of positrons with electrons. Positrons are emitted by the $\beta^+$-decay of isotopes ($^{11}$C, $^{13}$N, and $^{15}$O) origintated from the interaction between protons and patient tissues. This approach gives information without exposing the patient to an additional dose but the signal changes over time for the wash-out phenomenon occuring in perfused tissues [17]. Furthermore, the induced activity distribution in a tissue depends strongly on its elemental composition [18], thus different activity distributions can be provided by the same dose distribution delivered to different inhomogeneous tissue geometries. For this reason, the range verification requires a comparison between the measured activity distribution and a modelled activity distribution. PET imaging can be performed during the treatment (on line) or after the treatment (off line). The on line measurements do not require the repositioning of the patients but need some minutes to collect enough statistics to have a

sufficient signal to noise ratio, limiting the possibility to do on line corrections of the treatment. Furthermore, there are geometrical constraints to integrate the PET imaging system into the treatment room [19]. The off line measurements have the advantage that commercial PET scanners can be used with satisfactory results in terms of reproducibility and sensitivity [20]. *In vivo* PET range verification had a clinical implementation for intracranial and cervical spine target sites: for example, for head and neck patients it was demonstrated that the beam range can be verified with an accuracy of 1-2 mm in specific structures [17]. However, this approach has not yet provided an accurate range verification for every type of tumor and for all possible locations of the tumors[21].

The second indirect method for indirect range verification is PGI. It uses the gamma cascade emitted by excited target nuclei returning to their ground state after an interaction with an high-energy proton [22]. Table 1.1 presents the most common gamma-ray lines obtained from the interaction of high energy protons with $^{12}$C and $^{16}$O nuclei, together with the corresponding de-excitation transition and nuclear reaction that originates them [23]. A specific nuclear de-excitation produces a discrete line in the prompt gamma emission spectrum which has an energy range from 1 to 15 MeV. Fig. 1.3 shows an example of prompt gamma spectrum generated by a 160 MeV proton beam on a PMMA target [24]. Interactions between protons and target nuclei occur along the penetration path of protons and finish 2-3 mm before the Bragg peak beacuse the energy of the protons decreases along the penetration path. The dose deposited by the protons along their penetration path in tissue is correlated with the distribution of the emitted prompt gamma rays, thus measuring prompt gamma rays it is possible estimate the proton range. This correlation was initially observed with Monte Carlo simulations [22] and then experimentally verified [25, 26, 27, 28]. Fig. 1.4 shows this correlation between depth-dose profiles and photon production profiles for different energies of a proton pencil beam. Main advantages of prompt gamma imaging are the large amount of emitted gamma rays and their prompt temporal emission (few nanoseconds after the nuclear interactions), which allow to perform a real-time verification of the treatment. Furthermore, prompt gamma imaging does not require additional dose because an application of a therapeutic dose of 2 Gy/min has a high production rate of prompt gammas. As an example, a single spot beam of $10^8$ protons produces about $1.5 \times 10^7$ prompt gamma rays [30]. As a drawback, standard SPECT modules

**Table 1.1:** Gamma ray lines from proton reactions with $^{12}$C and $^{16}$O. Data from [23].

| Energy (MeV) | Transition | Reaction |
|:---:|:---:|:---:|
| 0.718 | $^{10}B^{*0.718} \rightarrow g.s.$ | $^{12}C(p,x)^{10}B^*$ |
|  |  | $^{16}O(p,x)^{10}B^*$ |
| 1.022 | $^{10}B^{*1.740} \rightarrow {}^{10}B^{*0.718}$ | $^{12}C(p,x)^{10}B^*$ |
|  |  | $^{16}O(p,x)^{10}B^*$ |
| 1.635 | $^{14}N^{*3.948} \rightarrow {}^{14}N^{*2.313}$ | $^{16}O(p,x)^{14}N^*$ |
| 2.000 | $^{11}C^{*2.000} \rightarrow g.s.$ | $^{12}C(p,x)^{11}C^*$ |
| 2.124 | $^{11}B^{*2.125} \rightarrow g.s.$ | $^{12}C(p,x)^{11}B^*$ |
| 2.313 | $^{14}N^{*2.313} \rightarrow g.s.$ | $^{16}O(p,x)^{14}N^*$ |
| 2.742 | $^{16}O^{*8.872} \rightarrow {}^{16}O^{*6.130}$ | $^{16}O(p,p')^{16}O^*$ |
| 3.684 | $^{13}C^{*3.685} \rightarrow g.s.$ | $^{16}O(p,x)^{13}C^*$ |
| 3.853 | $^{13}C^{*3.853} \rightarrow g.s.$ | $^{16}O(p,x)^{13}C^*$ |
| 4.438 | $^{12}C^{*4.439} \rightarrow g.s.$ | $^{12}C(p,p')^{12}C^*$ |
|  |  | $^{16}O(p,x)^{12}C^*$ |
| 4.444 | $^{11}B^{*4.445} \rightarrow g.s.$ | $^{12}C(p,2p)^{11}B^*$ |
| 5.105 | $^{14}N^{*5.106} \rightarrow g.s.$ | $^{16}O(p,x)^{14}N^*$ |
| 5.180 | $^{15}O^{*5.181} \rightarrow g.s.$ | $^{16}O(p,x)^{15}O^*$ |
| 5.240 | $^{15}O^{*5.241} \rightarrow g.s.$ | $^{16}O(p,x)^{15}O^*$ |
| 5.269 | $^{15}N^{*5.270} \rightarrow g.s.$ | $^{16}O(p,x)^{15}N^*$ |
| 5.298 | $^{15}N^{*5.299} \rightarrow g.s.$ | $^{16}O(p,x)^{15}N^*$ |
| 6.129 | $^{16}O^{*6.130} \rightarrow g.s.$ | $^{16}O(p,p')^{16}O^*$ |
| 6.175 | $^{15}O^{*6.176} \rightarrow g.s.$ | $^{16}O(p,x)^{15}O^*$ |
| 6.322 | $^{15}N^{*6.324} \rightarrow g.s.$ | $^{16}O(p,x)^{15}N^*$ |
| 6.337 | $^{11}C^{*6.339} \rightarrow g.s.$ | $^{12}C(p,x)^{11}C^*$ |
| 6.476 | $^{11}C^{*6.478} \rightarrow g.s.$ | $^{12}C(p,x)^{11}C^*$ |
| 6.741 | $^{11}B^{*6.743} \rightarrow g.s.$ | $^{12}C(p,x)^{11}B^*$ |
| 6.790 | $^{11}B^{*6.792} \rightarrow g.s.$ | $^{12}C(p,x)^{11}B^*$ |
| 6.916 | $^{16}O^{*6.917} \rightarrow g.s.$ | $^{16}O(p,p')^{16}O^*$ |
| 7.115 | $^{16}O^{*7.117} \rightarrow g.s.$ | $^{16}O(p,p')^{16}O^*$ |
| 7.299 | $^{15}N^{*7.301} \rightarrow g.s.$ | $^{16}O(p,p')^{15}N^*$ |
| 15.10 | $^{12}C^{*15.11} \rightarrow g.s.$ | $^{12}C(p,x)^{12}C^*$ |
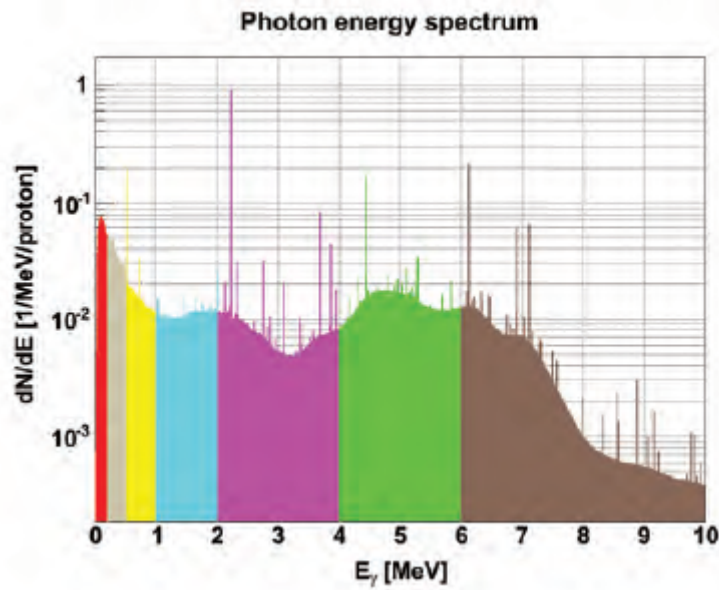
**Figure 1.3:** Energy spectrum of prompt gammas generated by a 160 MeV proton beam on a PMMA target [24].
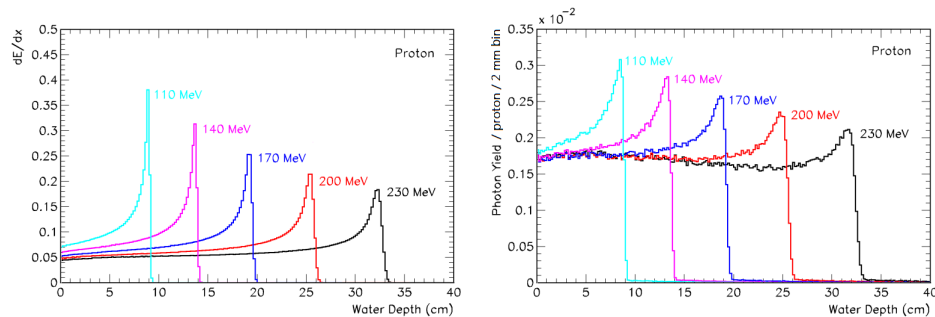


**Figure 1.4:** Depth-dose profiles (left) and photon production profiles (right) for pencil beams of protons incident along the axis of a cylindrical water target [29].

can not be used for PGI because they are designed for gamma-ray energies lower than of 1 MeV and for count rates lower than the rates required by PGI.

## 1.3 Prompt Gamma Imaging

This paragraph presents the state-of-the-art of prompt gamma imaging. Several research groups are evaluating different approaches to realize a prompt gamma imaging system. As mentioned in the previous paragraph, the goal of PGI is the measurement of the proton penetration depth inside the patient through the detection of the

prompt gamma-rays emitted along the beam path. The emission point of prompt gamma-rays can be calculated by reconstructing:

- the coordinates of interaction between the gamma-rays and the detector;

- the incident directions of the gamma-rays.

A position sensitive detector is necessary to measure the interaction coordinates. Usually, this detector is a scintillator detector, with pixelated or monolithic crystals. Instead, to discriminate the incident directions, a collimator to select gamma-rays is the simplest solution. Another solution is a multi-layer detector that has a first layer to generate a Compton scattering, and other layers to detect the scattered photons. In this way, the incident directions of the prompt gamma-rays can be found by employing Compton kinematics.

In addition to the prompt-gammas, also photons and neutrons uncorrelated with the beam can reach the camera. In particular, neutrons, which are generated in the interactions between protons and the patient's body, as well as with the components of the delivery system, contribute to the background signal and must be distinguished from the prompt gammas. For example, as neutrons and prompt gamma rays have different spectra, it is possible to discriminate the two contributions by selecting a proper energy window. Neutrons have a continuous spectrum with an energy range between their thermal energy and the incident proton beam energy. Instead prompt gammas have an energy range between 1 MeV and 8 MeV. Another discrimination criterion exploits the difference in the travelling times of photons and neutrons in a medium. As an example, photons in vacuum cover a distance of 30 cm in 1.0 ns, 10 MeV neutrons cover the same distance in 21.7 ns, and 100 MeV neutrons in 6.9 ns. Thus, the use of a fast scintillator combined with a time of flight (ToF) technique is suitable to select events corresponding to the desired time window of PG photons only. The ToF technique requires a trigger signal coincident with the beam to determine when the bunches of protons hit the patient. This signal can be obtained directly from the cyclotron or, alternatively, from a dedicated detector crossed by the proton beam before its interaction with the patient.

These considerations point out the various ways to build an effective gamma detector for PGI. Many research groups have investigated different solutions for the reconstruction of a 1-D profile of the beam path, which are listed here:

- Scanning system and multi-slit camera

- Compton camera

- Knife-edge slit-camera

Additional techniques to improve these detection systems are:

- Measure of the discrete prompt gamma lines

- Use of the ToF technique

A brief description of each technique is presented in the following paragraphs.

**Scanning system and multi-slit camera**

The first experimental results of prompt gamma imaging were obtained using a scanning system [14]. The setup, shown in Fig. 1.5, consists of a Prompt Gamma Scatter (PGS), and a collimator. The collimator is designed to select gammas and
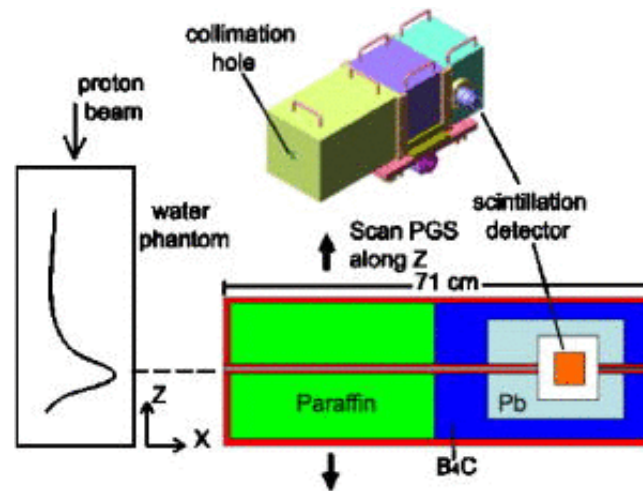


**Figure 1.5:** Prompt gamma scanning system. Picture from [14], reproduced by permission of AIP Publishing, all rights reserved.

to block out fast neutrons. The PGS is made of three layers of shielding to stop neutrons generated from the phantom. The core of the PGS is a gamma detector, consisting of a photomultiplier tube that collects the light of a CsI(Tl) scintillator. The setup is positioned to count the gammas emitted in a perpendicular direction with respect to the beam direction. Fig. 1.6 shows the correlation between prompt gamma peaks and Bragg peaks measured with this setup and with a ionization
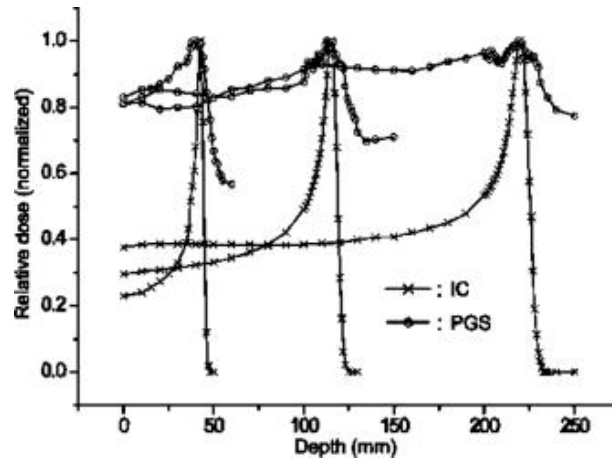
**Figure 1.6:** Comparison of the depth-dose distributions measured by the ionization chamber with the PGS measurements at three different proton energies of 100, 150 and 200 MeV. Picture from [14], reproduced by permission of AIP Publishing, all rights reserved.

chamber, respectively. The use of a scanning system is not practical for clinical routine because the full Field of View (FoV) can not be measured by a single position. To scan the full FoV, it is possible to shift the system in various positions but this operation takes a long time. Despite this drawback, the use of such a detection system demonstrated that the prompt gammas can be used to verify the proton range in proton therapy.

To avoid moving the scanning system, a proposed solution is the use of a linear array of scintillator detectors in combination with a multi-slit collimator [31]. Fig. 1.7 shows an example of an array-type prompt gamma detection system. This system has multiple CsI(Tl) scintillator detectors coupled to photo-diodes and each separated by a 6 mm-thick lead shield, and a collimator with 4 mm-wide collimation slits. Each scintillation detector counts prompt gammas passing through their respective collimation slits. The acquired profile of a multi-slit camera system is a one-dimensional projection of the emission profile along the beam path. Being this projection direct, the parallax effect can be avoided. To determinate the proton range from a profile, it is necessary to measure the location of the Bragg peak and the projection of the point where the beam enters into the patient. A multi-slit camera can be made large enough to cover the desired FoV, and thus to measure both positions. Even considering these advantages, no experimental results have been published yet.
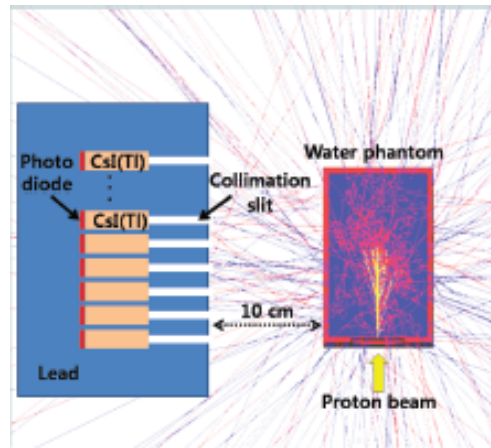
**Figure 1.7:** Schematic diagram of an array-type prompt gamma detection system, based on a multi-slit collimator and CsI scintillators coupled to photo-diodes. Picture from [31], reproduced by permission of John Wiley and Sons, all rights reserved.

**Compton camera**

Another method for prompt gamma imaging uses a multi-stage detector known as Compton camera. The initial energy and the direction of a gamma ray are measured through Compton scattering in the different stages of the detector. A traditional Compton camera has one scatter detector and one absorber detector [32]. Photons scatter in the first detector and are absorbed in the second one. By measuring the interaction positions in the scattering stage and the energy in the absorber, it is possible to reconstruct cones which contain the incident trajectories. The intersection of all cones provides the photon's emission point. It have been studied various types of Compton cameras which use detector layers of different materials and geometries. In addition, it is possible use a Compton camera in combination with a beam hodoscope [33]. This last device provides a time reference for time of flight measurements (to discriminate the gamma signal from the background) and a spatial tagging of the incident ions in the plane transverse to the beam. Fig. 1.8 shows a schematic example of a Compton camera, with three detectors and a hodoscope, studied with Monte Carlo simulations. In this example the camera has two silicon scatter detectors to make a direct analytic reconstruction of the direction, and one LYSO scintillation absorber detector which has a sufficient time resolution for time of flight measurements. The prompt gamma emission points can be deduced from the position measurements in the three detectors, and the energy measurements can be obtained from the two scatter detectors.
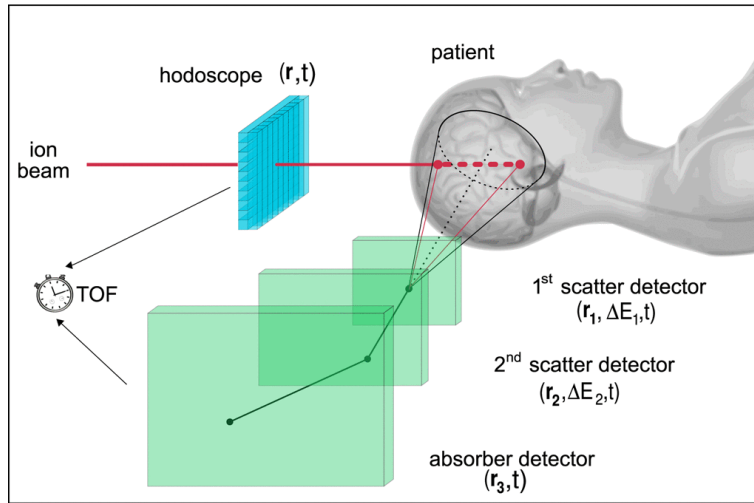
**Figure 1.8:** Configuration of the detection system for prompt gamma imaging with a Compton camera and a hodoscope. Picture from [33], copyright 2011, IEEE.

Compton imaging technique has not been applied during proton irradiation yet but in the literature are presented some promising studies of Compton cameras [34, 35, 36].

**Knife-edge slit-camera**

The slit-camera technique is based on a pin-hole collimator [28], and is an alternative to the scanning system with a parallel-hole collimator, which has been presented in the first part of this paragraph. Fig. 1.9 shows an example of setup which has a gamma camera combined with a slit collimator [29]. This geometry focuses on the measurements of the depth at which the beam stops in the patient. The slit collimator is made in tungsten and is 4 cm thick. The slit angle is $63^o$ and the slit aperture is 6 mm. This configuration was experimentally verified with a first prototype based on a gamma detector for low energy SPECT applications [28], and with a detector which has been designed to provide high counting statistics for prompt gamma rays of several MeV [37]. With this setup a measurement of range control at two different beam energies of 100 MeV and 160 MeV was performed. To emulate a range shift of the Bragg peak, the target was moved along the beam axis at 8 different positions with respect to a central position. Fig. 1.10 (a) shows the detected profiles at the different positions of the target, at 100 MeV. Instead, Fig. 1.10 (b) shows the position of the target with respect to the central position as a function of the detected profile shift, at 100 MeV and 160 MeV. At 100 MeV the measured shift
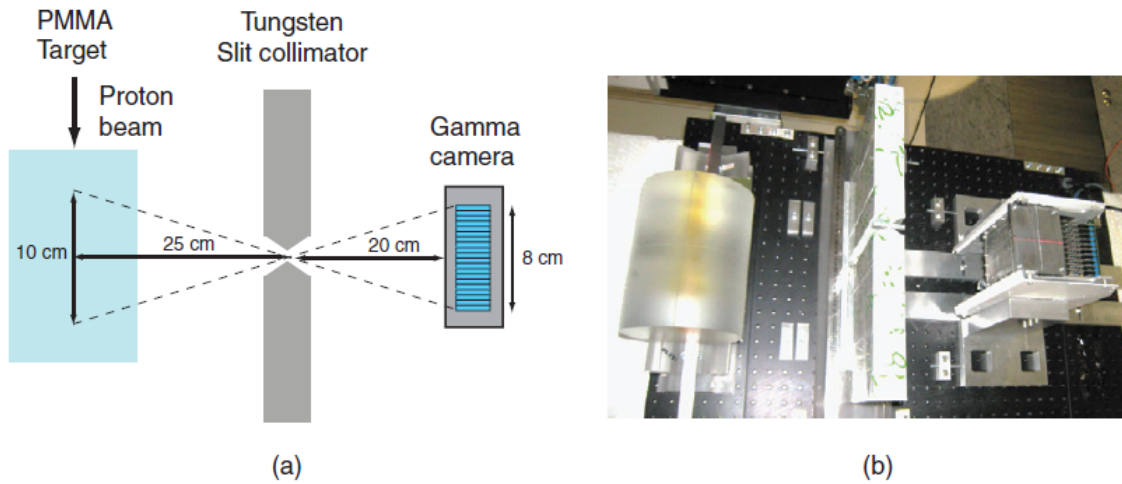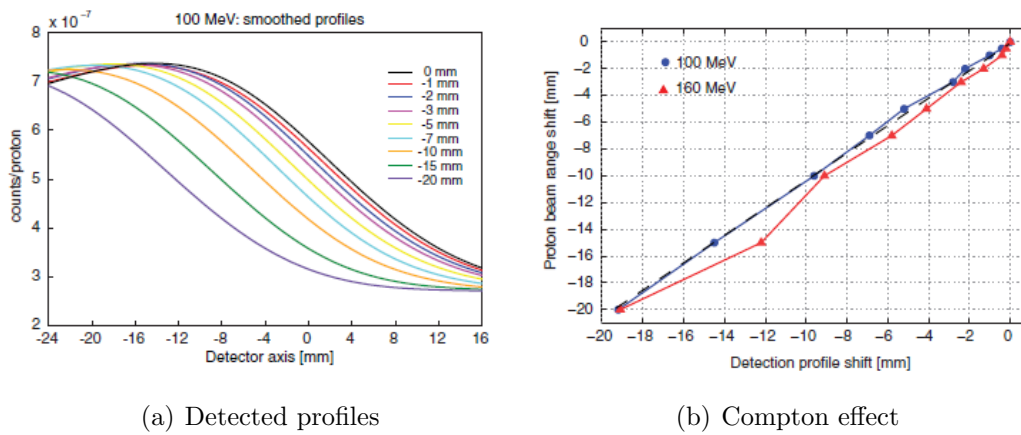
**Figure 1.9:** Schematic (a) and picture (b) of a setup for prompt gamma imaging with a slit camera. This type of collimator gives a 1D projection of prompt gamma emission on a scintillation detector. Picture from [37], reproduced by permission of IOP Publishing, all rights reserved.



(a) Detected profiles                    (b) Compton effect

**Figure 1.10:** Detected profiles measured at 100 MeV (a) as the target is moved along beam axis to induce the detection of range shifts by the camera. Exact shift of the proton beam range as a function of the shift of the acquired profiles for pencil beams of 100 MeV (the blue line in (b)). Picture from [37], reproduced by permission of IOP Publishing, all rights reserved.

follows the expected shift, while at 160 MeV the measured shift is lower than the expected shift. The knife-edge slit-camera concept has been also used with the time of flight technique which improves the detection of small ($\sim$1 mm) range shift [38]. Both these studies show the feasibility of the prompt gamma profile acquisitions for *in vivo* range verifications, and the possibility to integrate the camera in a proton therapy treatment due to its compact design.

**Measure of the discrete prompt gamma lines**

A technique to improve the accuracy and sensitivity of range verification uses discrete prompt gamma lines from the energy spectrum, more precisely the 4.44 MeV and 6.14 MeV lines due to $^{12}$C and $^{16}$O, respectively. The total PG emission per incident proton and per Gray of absorbed dose for these two lines, depends on the concentration of carbon and oxygen in the target [39]. Each discrete gamma line is generated by specific nuclear level transitions and has a unique correlation with the proton energy. Therefore, the identification of these lines improves the accuracy and sensitivity of the range verification. In fact, the proton energy is known and the nuclear reaction cross sections can be used as prior knowledge in the range verification. Thus, from the cross sections for the production of the prompt gamma-rays for these two specific gamma emissions can be estimated the concentrations of target nuclei in the irradiated tissue. This makes the range verification more robust if the proton beam stops in tissue with an uncertain composition. Fig. 1.11 shows the setup used to successfully perform range verification with this technique. A
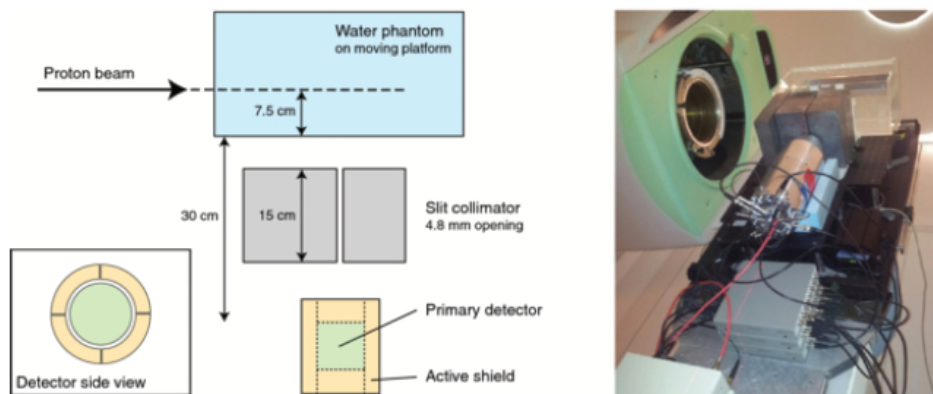


**Figure 1.11:** Setup for energy and time-resolved detection of prompt gamma rays for proton range verification. Picture from [26], reproduced by permission of IOP Publishing, all rights reserved.

photomultiplier tube (PMT) is coupled to a cylindrical scintillator LaBr$_3$ to form

the primary detector. Around this detector there are four optically separated BGO crystals, which act as a shield to reduce both the Compton background and the neutron-induced gamma-ray background. To collimate the prompt gamma rays is used a slit collimator. To acquire data it is necessary to use a digital data acquisition system suitable for high count rates. Whit this setup, the magnitude of the gamma lines at 4.44 MeV, 5.2 MeV and 6.13 MeV are quantified for 27 positions along the path of proton beams and compared with the proton depth-dose curve. The results are presented in Fig. 1.12 and show a clear correlation of the prompt gamma-ray emission with the proton depth-dose curve. This technique is suitable
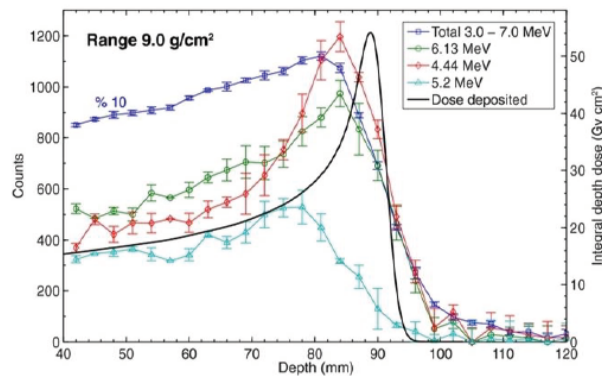


**Figure 1.12:** Energy-integrated and discrete prompt-gamma ray emissions along the path of proton pencil-beams in water. Picture from [26], reproduced by permission of IOP Publishing, all rights reserved.

for clinical routine but it is necessary to improve the detector design and the scale of the prototype.

**Use of the ToF technique**

As explained in the introduction of this section, one of the main problems of prompt-gamma imaging is the presence of photons and neutrons uncorrelated with the beam range. This effect is well explained by an example of simulated prompt gamma ToF spectrum, which is presented in Fig. 1.13 [40]. The prompt gamma ToF spectrum forms a narrow peak in time, which occurs earlier than the maximum of the much broader neutron ToF spectrum. ToF technique for proton beams has been improved experimentally using a single-slit camera [41]. Fig. 1.14 shows the camera which is composed by a tungsten collimator with a single parallel-edge slit and a LYSO scintillator detector. The target was moved along the beam axis to acquire the whole prompt gamma emission profile with the single-slit collimator. The arrival
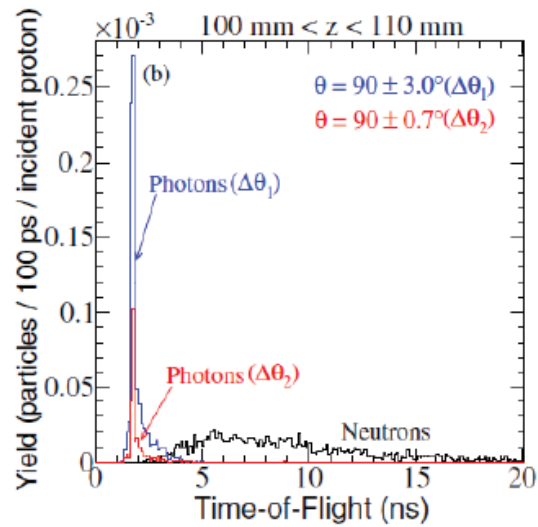
**Figure 1.13:** Simulated ToF spectra of the prompt gamma photons (blue and red) and neutrons (black) for a 200 MeV proton beam. Picture from [40], reproduced by permission of IOP Publishing, all rights reserved.

time of the particle is related to proton bunches, the hit in the detector was used as a start signal and the frequency signal of the cyclotron was used as stop signal. Fig. 1.15 shows how much the TOF discrimination is effective in the reduction of the background without modifying the falloff signal amplitude. Although ToF discrimination requires additional data elaboration and changes the design, it represents a powerful option to include in a prompt gamma camera.

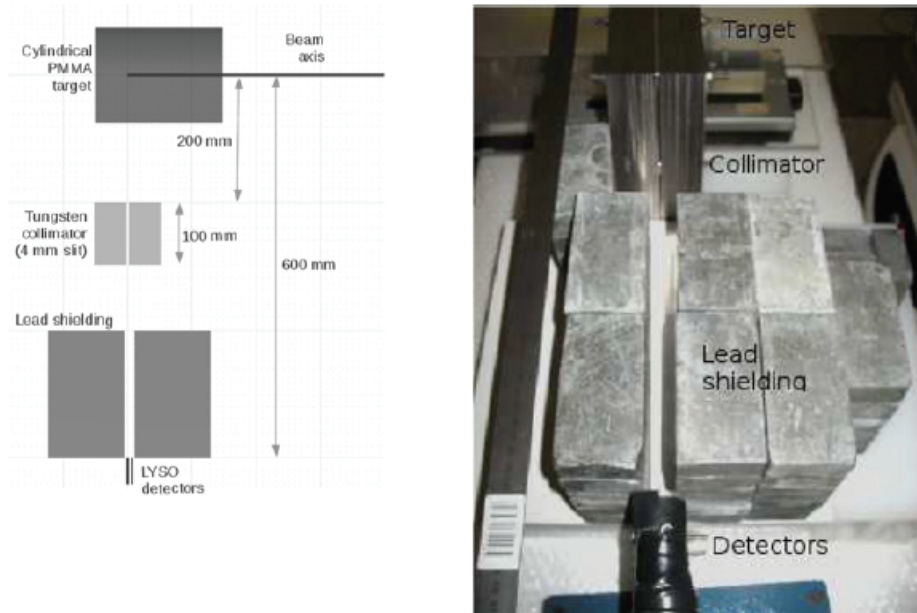**Figure 1.14:** Setup used for prompt gamma imaging with a single-slit collimator and ToF technique. Picture from [41], reproduced by permission of IOP Publishing, all rights reserved.
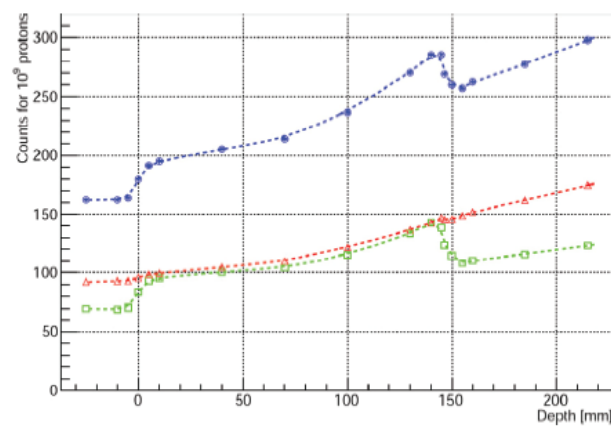


**Figure 1.15:** Comparison between a profile without (blue line) and with (green line) ToF. The red line is the difference between the two profiles. Picture from [41], reproduced by permission of IOP Publishing, all rights reserved.

## 1.4 Gammarad project

From the previous paragraph it is clear that prompt gamma imaging has become more popular in recent years. Several research groups are evaluating different approaches to realize a prompt gamma imaging system suitable for the use in clinical conditions and the optimization of a gamma-ray detector for PGI is still ongoing.

The Gammarad project works in this direction and aims at developing a high-performance and solid-state gamma ray detection module (GDM) to be used in a slit-camera [42]. Fig. 1.16 shows the concept of the slit-camera technique for prompt gamma imaging, which provides a 1-D projection of emitted prompt gamma-rays on the GDM. The slit design is simpler and cheaper than the other techniques reported throughout this paragraph.
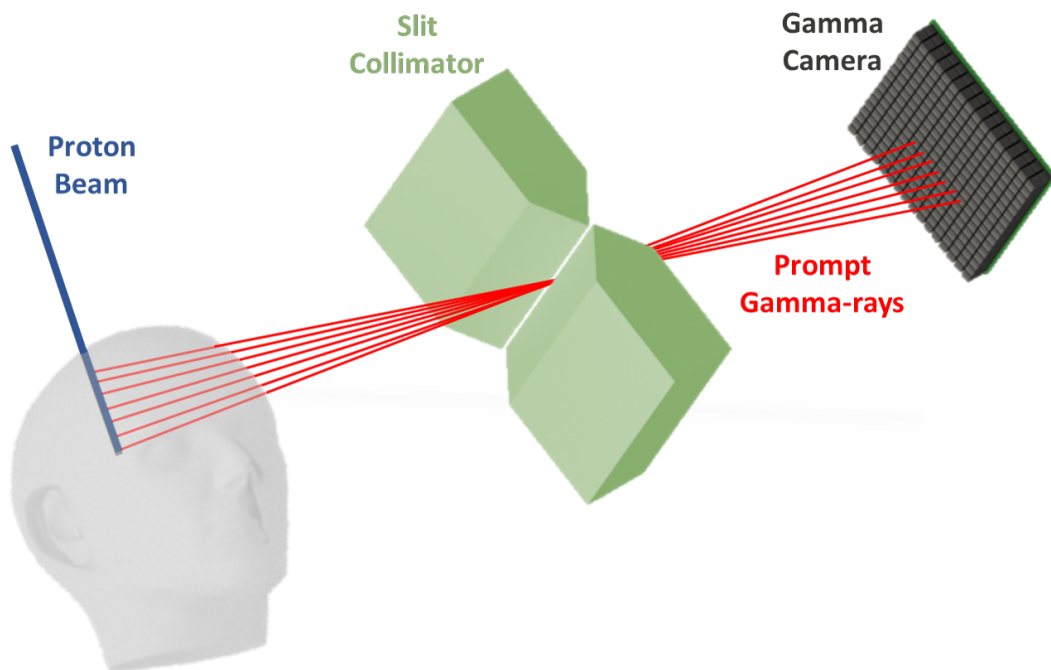


**Figure 1.16:** Concept of the slit-camera technique for prompt gamma imaging.

The complete position sensitive gamma detector, in Fig. 1.17, will have nine single GDMs. A single GDM, shown in Fig. 1.18, consists of a tile of 64 photo-sensors coupled to a LYSO crystal with 64 pixels. The project is based on a collaboration among Fondazione Bruno Kessler (FBK, Trento, Italy) [43], Politecnico di Milano (Milano, Italy) [44], the Trento Institute for Fundamental Physics and Applications

**Figure 1.17:** Detailed picture of Gammarad position sensitive detector. The complete detector consists of nine single modules.



**Figure 1.18:** Assembled view of a single module (right) and exploded view (left).

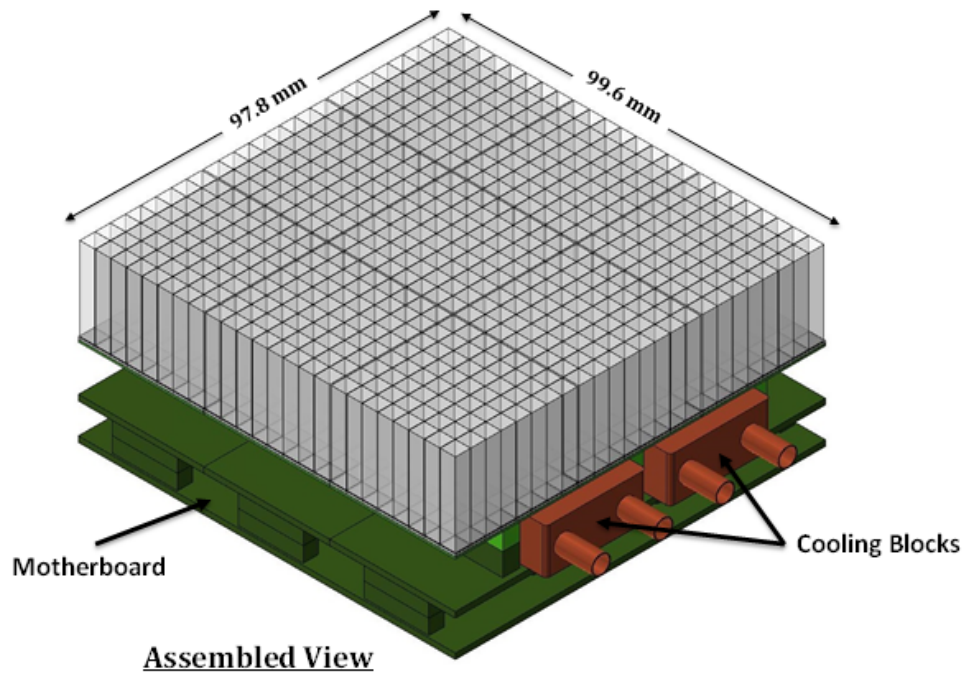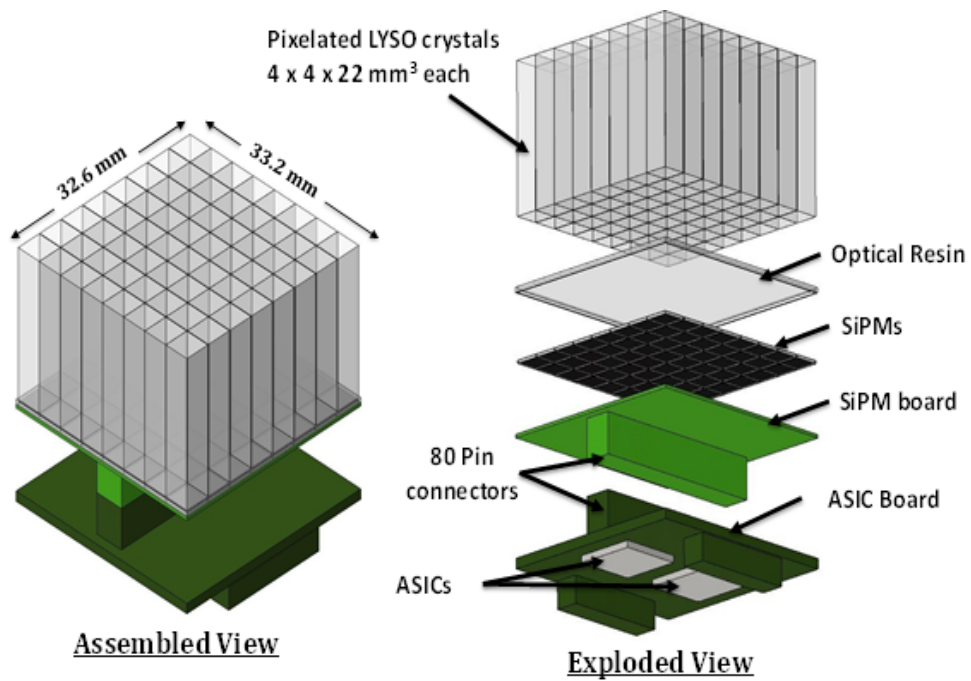(TIFPA, Trento, Italy) [45], and the Proton Therapy Center of Trento (Italy) [46]. The project is divided into two parts. The first part focuses on the technological development of a gamma-ray imaging module. This module is composed by a gamma-ray detector, based on a solid-state silicon sensor, and an integrated circuit. They are assembled into a compact module with data and control systems. The required detection module specifications are:

- High linearity at high energy: lower than 5% in the whole energy range.

- Energy range: 1-15 MeV.

- Count rate: 1-10 MHz/cm$^2$.

- Intrinsic spatial resolution: 4 mm.

- Energy resolution: 10% at 2 MeV.

The second part of the project is dedicated to the experimental validation of the system both in laboratory with radioactive sources and in a real environment, that of proton therapy.

## 1.5 Motivation of the dissertation

The most innovative part of the gamma-ray detector developed for the project is the photo-sensor used for the scintillation light readout. In traditional applications it is a photomultiplier tube (PMT). However, in recent years, Silicon Photomultipliers (SiPMs) have become increasingly popular in a variety of applications for their promising characteristics. Among them, current-generation SiPMs offer high gain [47], high photon detection efficiency [48], excellent timing performance [49, 50], high count-rate capability, and good radiation hardness [51]. Due to these characteristics they are used as PMTs replacement in several applications, such as in nuclear medicine (PET) [52, 53], in high-energy physics (calorimeters) [54], astrophysics (Cherenkov telescopes) [55], and in other single-photon or few-photon applications [56].

For their characteristics, SiPMs are also very promising for the scintillator readout in prompt gamma imaging [37], and in high energy gamma-ray spectroscopy [57].

Detectors for these applications must be compact, robust, and insensitive to magnetic fields. They have to provide high performance in terms of spatial, temporal, and energy resolution. SiPMs can satisfy all these requirements but typically they have been used with relatively low energy gamma rays and low photon flux, so manufacturers have optimized them for these conditions. Because of the limited number of micro-cells in a standard SiPM (625 cells/mm$^2$ with 40 $\mu$m cells) the detector response is non-linear in high-energy conditions. Increasing the cell density is extremely important to improve the linearity of the SiPM and to avoid the compression of the energy spectrum at high energies, which worsens the energy resolution and makes the calibration of the detector more difficult. On the other hand, small cells provide a lower Photon Detection Efficiency (PDE) because of the lower Fill Factor (FF) and as a consequence a lower energy resolution. Summarizing, the energy resolution at high energies is a trade-off between the excess noise factor (ENF) caused by the non-linearity of the SiPM and the PDE of the detector. Moreover, the small cell size provides an ultra-fast recovery time, in the order of few of nanoseconds for the smallest cells. A short recovery time together with a fast scintillator such as LYSO, reduces pile-up in high-rate applications as PGI.

Based on the previous considerations, the aim of this thesis is to develop an optimized gamma-ray detector composed of SiPMs for high-dynamic-range applications, such as the scintillation light readout in prompt gamma imaging and in high-energy gamma-ray spectroscopy. The SiPMs evaluated for the detector are High-Density (HD) and Ultra-High-Density (UHD) SiPM technologies recently produced at Fondazione Bruno Kessler (FBK). Instead of standard SiPMs, HD and UHD SiPMs have a very small micro-cell pitch, from 30 $\mu$m down to 5 $\mu$m with a cell density from 1600 cells/mm$^2$ to 46190 cells/mm$^2$, respectively.

# Chapter 2

# Silicon Photomultiplier

In this chapter, we introduce briefly Silicon Photomultipliers (SiPMs) and their working principle. Then we present the parameters that represent SiPM performance, such as photon detection efficiency, dark count rate, cross-talk, after-pulsing, and non-linearity. Then, we also describe the techinques used to measure these parameters. In the last part of the chapter we introduce the SiPM technologies which were chosen for this work: High-Density and Ultra-High-Density SiPMs. Both technologies are produced in a research foundry at Fondazione Bruno Kessler (FBK), Trento, Italy [58, 43, 59].

## 2.1   Working principle

Base components of Silicon Photomultipliers (SiPMs) are Single-Photon Avalanche
Diodes (SPADs) [47, 60].  A SPAD is a photo-diode, based on silicon junction,
that operates in the so-called Geiger mode.  In this operating mode, the diode is
biased above the breakdown voltage, thus a high electric field is generated across
its depletion region. If a photon is absorbed in this depletion region a electron-hole
pair is created. These charge carriers are accelerated by the high electric field, and
acquire sufficient energy to ionize a silicon atom during a collision. This phenomenon
is called impact ionization. From the ionization of a silicon atom is generated a new
electron-hole pair, called secondary.  These secondary charge carriers, accelerated
by the electric field, produce a new impact ionization event, and so on.  Fig. 2.1
shows the difference in the charge carrier multiplication between an Avalanche Photo
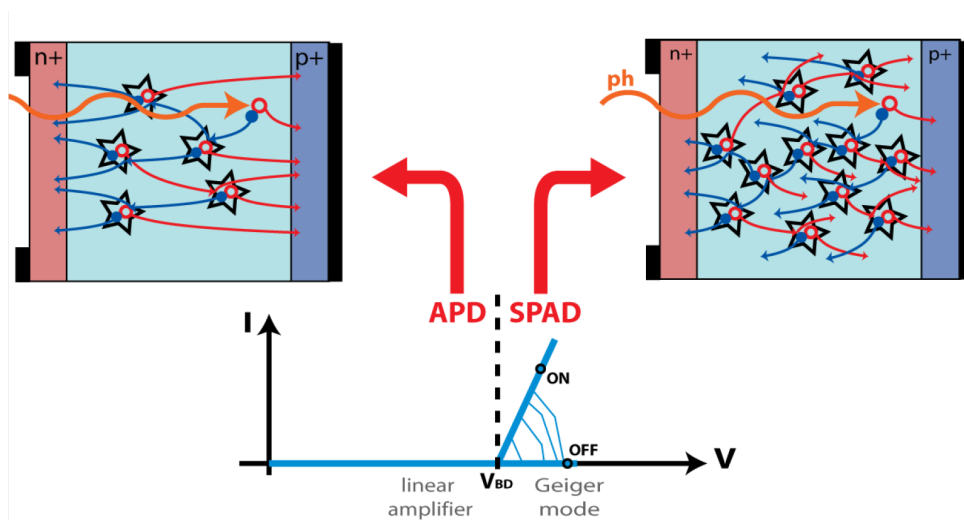Diodes (APD), which does not work in Geiger mode, and a SPAD. Thus, in a



**Figure 2.1:**   Charge carrier multiplication in a APD and in a SPAD.

SPAD a large number of secondary electron-hole pairs are created and, as results,
an avalanche of charge carriers pass through the diode generating a self-sustaining
sizable current.  At this time, a single optical photon can be detected.  To detect
another photon, it is necessary to quench the avalanche using passive or active
elements [61].  Fig. 2.2, Table 2.1, and Table 2.2 describe schematically a SPAD
avalanche evolution time in two different cases:  without a quenching system, and
with a quenching system.   During the avalanche and the quench time, a SPAD is not
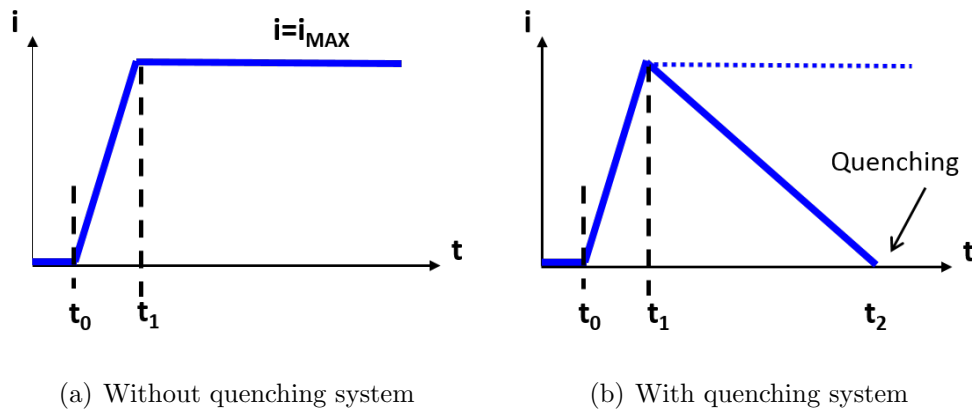
(a) Without quenching system  (b) With quenching system

**Figure 2.2:** SPAD avalanche evolution time: without quenching system (a), see Table 2.1, and with quenching system (b), see Table 2.2.

**Table 2.1:** SPAD avalanche evolution time without a quenching system

| Time | SPAD situation |
|---|---|
| $t = 0$ | $V_{SPAD}(0) = V_{Breakdown} + V_{Over-voltage}$ |
| $t < t_0$ | No photons, no signal |
| $t = t_0$ | Photon! $\rightarrow$ Avalanche initiation |
| $t_0 < t < t_1$ | Avalanche spreading across junction |
| $t > t_1$ | Self-sustaining avalanche current (limited by series resistance) |
| $t > t_2$ | - |
| **Result** | **Another photon can not be detected** |

**Table 2.2:** SPAD avalanche evolution time with a quenching system

| Time | SPAD situation |
|---|---|
| $t = 0$ | $V_{SPAD}(0) = V_{Breakdown} + V_{Over-voltage}$ |
| $t < t_0$ | No photons, no signal |
| $t = t_0$ | Photon! $\rightarrow$ Avalanche initiation |
| $t_0 < t < t_1$ | Avalanche spreading across junction |
| $t > t_1$ | Self-sustaining avalanche current (limited by series resistance) |
| $t > t_2$ | Avalanche has been quenched $\rightarrow$ $V_{SPAD}(t_2) = V_{SPAD}(0)$ |
| **Result** | **A new photon can be detected** |

able to detect other photons. Thus, if more than one photon impinges on the SPAD simultaneously, the SPAD output does not change. Fig. 2.3 shows an example of the SPAD output when one or five photons are absorbed at the same time. To avoid this
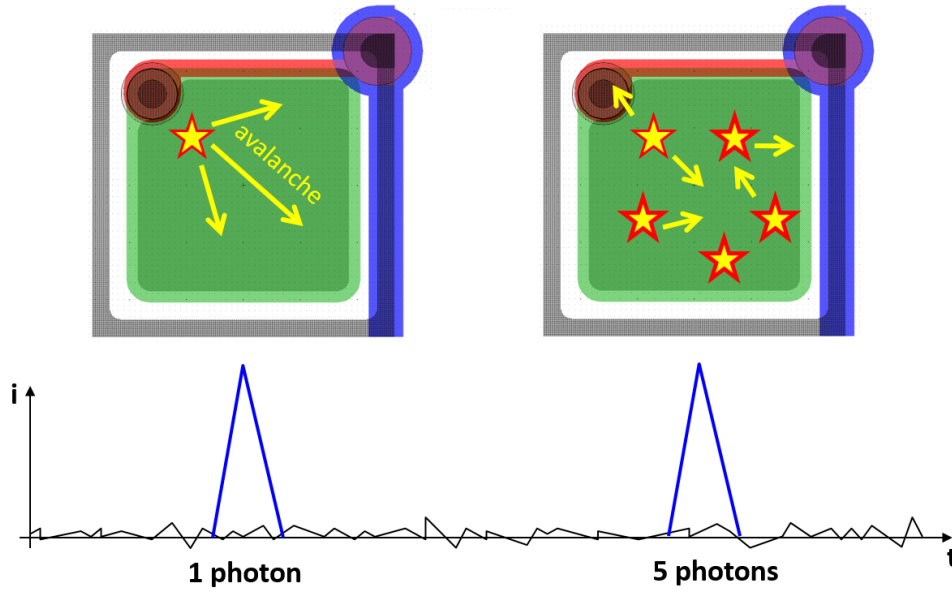


**Figure 2.3:** SPAD output when one photon (left) and five photons (right) are detected.

limitation many SPADs are connected in parallel to common anode and cathode to form a matrix: this device is called Silicon Photomultiplier (SiPM) [62, 63]. Fig. 2.4 shows the circuit diagram of a SiPM, and Fig. 2.5 shows a microscope's image of a SiPM produced in FBK. Each SPAD of a SiPM has its own quenching resistor and single photon detection capability. Fig. 2.6 shows the equivalent circuit of a SPAD, which was modeled in the '60 to study micro-plasma instabilities in p/n junctions [64, 65]. $C_D$ is the diode capacitance, $R_S$ is the series resistance, $R_Q$ is the quenching resistance, $V_{BD}$ is the breakdown voltage, and $V_{Bias} > V_{BD}$. As a first approximation, the signal shape of a SPAD depends on these terms. Fig. 2.7 shows an ideal example of the signal time dependence. The real response is complicated by parasitic capacitance contributions from both the quenching resistance and the neighbouring cells [66]. This signal is the superimposition of two components, slow and fast [67]. Usually, the predominant component is the slow component which is due to the slow recharge through to the quenching resistance. The fast component become visible in case of large $R_Q$ and it is due to fast voltage variation acorss the parasitic capacitance of the quenching resistance [67]. Fig. 2.8 shows an example of
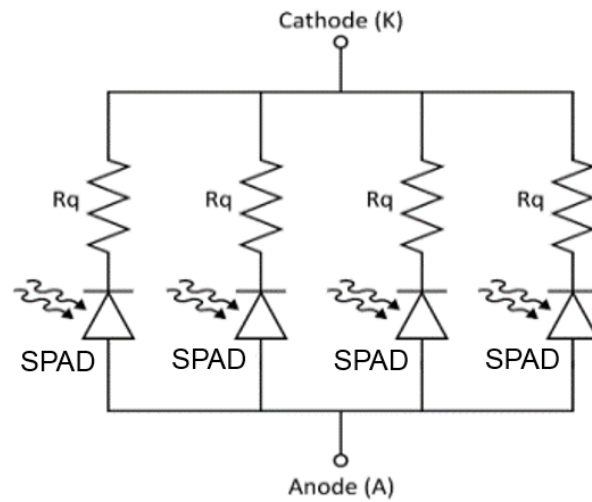
**Figure 2.4:** Schematic diagram of a SiPM. The SPAD and the quenching resistor form a single SiPM microcell.
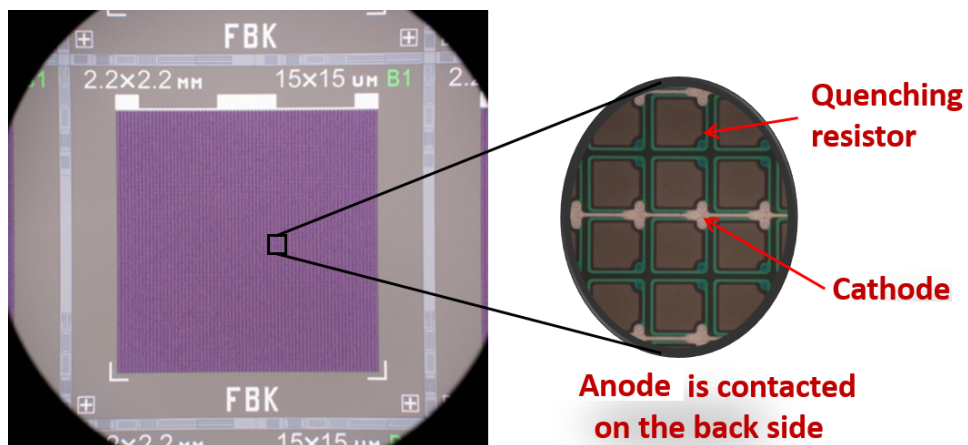


**Figure 2.5:** SiPM image with zoom on the SPAD matrix.

**Figure 2.6:** Equivalent circuit of a SPAD. $C_D$ is the diode capacitance, $R_S$ is the series resistance, $R_Q$ is the quenching resistance and $V_{BD}$ is the breakdown voltage.



**Figure 2.7:** Pulse shape of a SPAD. $C_D$ is the diode capacitance, $R_S$ is the series resistance, $R_Q$ is the quenching resistance, $V_{BD}$ is the breakdown voltage, and $V_{Bias}$ is the applied voltage.

a pulse shape with both these components.



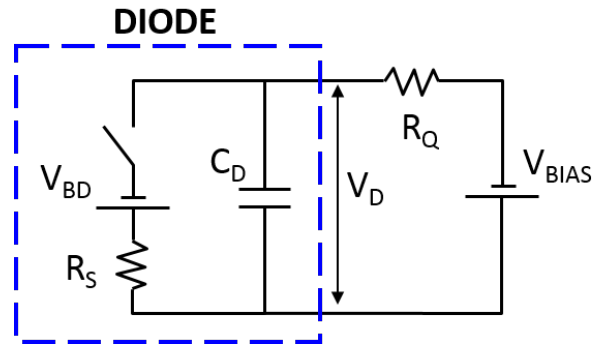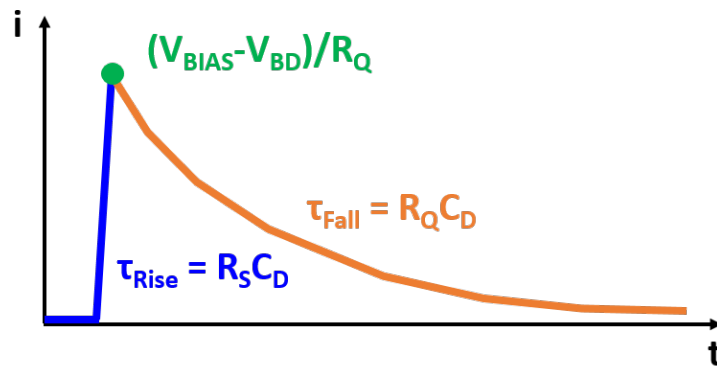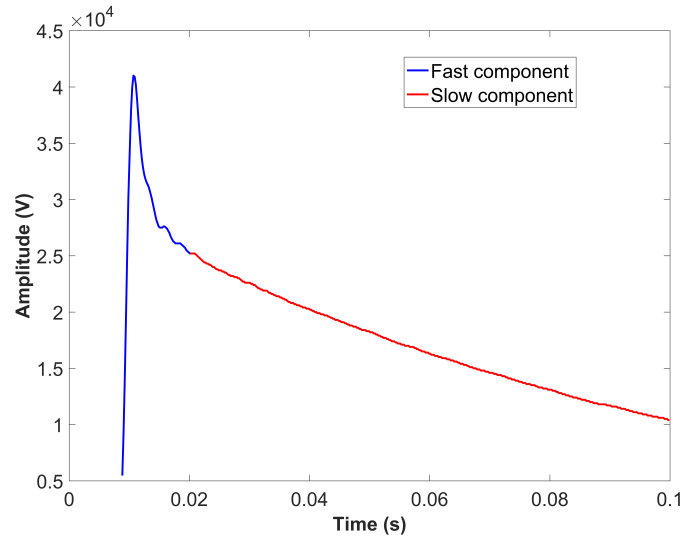**Figure 2.8:** Example of a pulse shape of a SPAD which have both components: slow and fast.

Each SPAD of a SiPM is independent and produces the same amount of charge when fired by a photon so the response of the SiPM is proportional to the number of triggered SPADs, and thus to the number of photons. Fig. 2.9 shows the SiPM output signal measured with an oscilloscope operating in persistance mode. The various signals are proportional to the number of triggered SPADs: one, two, three, and so on. The SiPM output signal is the sum of the output of its single microcells.



**Figure 2.9:** SiPM output signal. The output is proportional to the number of detected photons. When one photon triggers an avalanche in one SPAD the output charge is single. If two photons trigger an avalanche in two different SPAD the output charge is double, and so on for more photons.

## 2.2    Characterization of SiPMs

The main SiPM parameters are:

- **Breakdown voltage**: the bias voltage at which the value of the electric field, generated in the depletion region, is enough to start a self-sustaining avalanche.

- **Gain**: the number of generated electrons per detected photon.

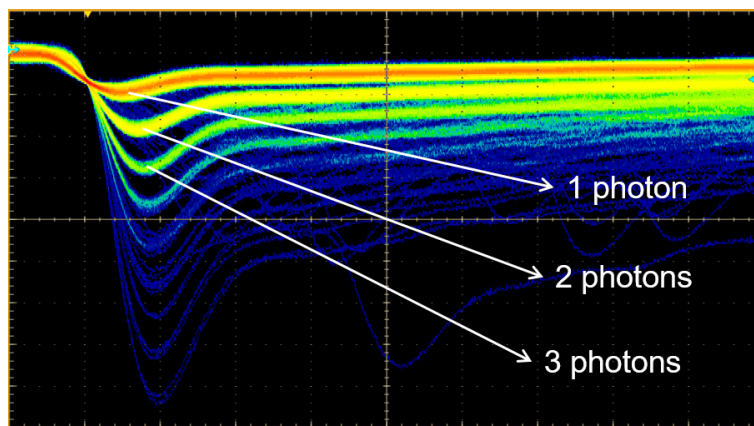- **Photon detection efficiency**: the number of detected photons over total incident photons.

- **Primary noise**: pulses generated by thermally generated carriers in the depleted region. It is also called dark count rate and it is not due to incident photons.

- **Correlated noise**: pulses generated because of a previous pulse, either photon or thermally generated. It includes two different types of noise: the after-pulsing and cross-talk. The after-pulsing is due to carriers trapped during an avalanche, and released at a later time. The cross-talk is due to photons generated in one cell during an avalanche discharge: they can be absorbed in adjacent cells, thus triggering a new avalanche.

- **Dynamic range**: linearity of the response, which is limited by the finite number of cells.

- **Single photon time resolution**: precision in the determination of photon arrival time.

These parameters are examined in detail in next paragraphs.

### 2.2.1    Breakdown voltage and gain

The breakdown voltage is the minimum voltage that should be applied to a SiPM to create a self-sustaining avalanche after a photon absorption. The breakdown voltage is clearly visible from the reverse I-V characteristic as a sudden increase in current, as shown in the example of Fig. 2.10. Its value depends on the electric field inside the SiPM, which in turns, depends on the doping profiles of the SiPM.
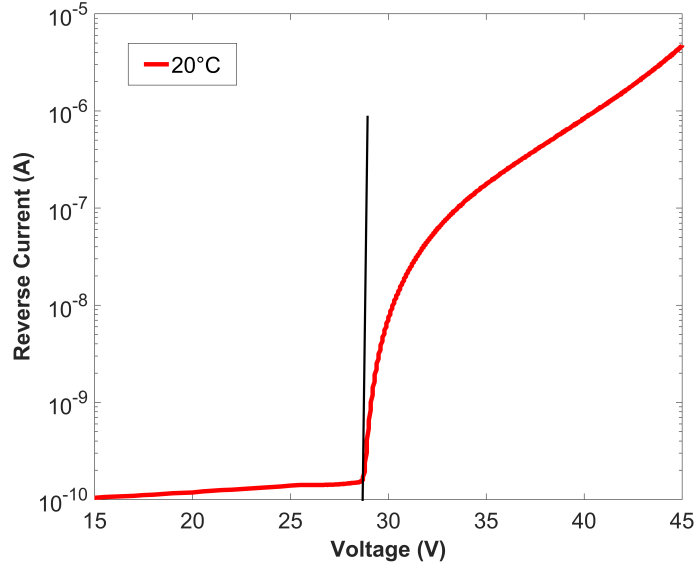
**Figure 2.10:** Reverse I-V curve of a 4x4 mm$^2$ RGB-HD SiPM with 25 $\mu$m-cell, at 20 $^o$C. The breakdown voltage is indicated with the dark vertical bar.

There is a positive shift of the breakdown voltage with the temperature increase due to variations in carrier mobility and ionization rates [68]. Fig. 2.11 shows this phenomenon for temperatures between -40 $^o$C and 40 $^o$C. This variation of the breakdown as a function of temperature is linear, as a first approximation, and for the RGB-HD SiPM technology the variation coefficient is 25.5 mV/$^o$C.

This dependence of the breakdown voltage on the temperature causes a variation of the gain when operating the SiPM at fixed bias in unstable thermal conditions. The gain is the total charge generated per single event and is obtained by integrating the current signal shown in Fig. 2.7. The gain is determined by circuital elements and by the voltage bias. It can be expressed as:

$$Gain = \frac{Q_{Cell}}{q} = \frac{(V_{Bias} - V_{BD}) \cdot C_D}{q}, \tag{2.1}$$

where q is the electron charge, $Q_{Cell}$ is the is the total charge at the cell electrode, which is equal to the product between the cell capacitance, $C_D$, and the over-voltage, i.e. $V_{BD}$ - $V_{Bias}$. From Eq. 2.1 it is clear that the gain changes if $V_{Bias}$ is not adjusted accordingly to temperature variations. In general, SiPMs must be operated at controlled temperature.
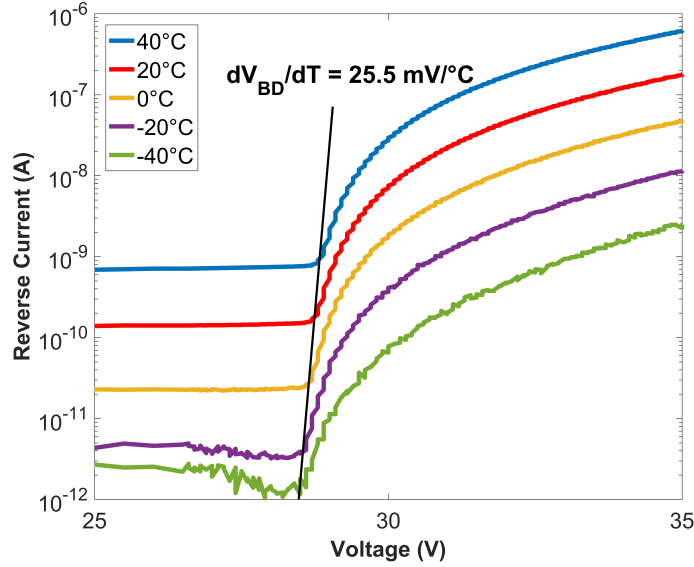
**Figure 2.11:** Reverse I-V curves of a 4x4 mm$^2$ RGB-HD SiPM with 25$\mu$m-cell, at different temperatures. The breakdown voltage has a positive shift by increasing the temperature.

## 2.2.2 Photon detection efficiency

The Photon Detection Efficiency (PDE) is the probability that one photon is detected by a SiPM and can be expressed as:

$$PDE = \frac{N_{Pulses}}{N_{Photons}} = FF \cdot QE \cdot P_{Trig}, \tag{2.2}$$

where N$_{Pulses}$ is the number of detected photons, N$_{Photons}$ is the number of incident photons, FF is the Fill Factor of the SiPM cell, QE is the Quantum Efficiency, and P$_{Trig}$ is the Trigger Probability.

In detail, the fill factor is the geometrical ratio between the sensitive area and the total area of the cell, as shown in Fig. 2.12. The FF is defined by the cell layout and is reduced by structures present around each micro-cell, such as guard ring, trench, and quenching resistance. In general, the FF grows with the cell size.

The Quantum Efficiency is the probability for a photon to generate a carrier that reaches the high-field region. It depends on the reflectivity of the silicon surface, and on the absorption length in silicon. The reflection can be reduced with an Anti-Reflecting (AR) coating. Fig. 2.13 shows the absorption length in silicon as a function of the wavelength and highlights that theoretically shallow junctions for short wavelength, and thick depletion layers for long wavelength help to optimize the QE.

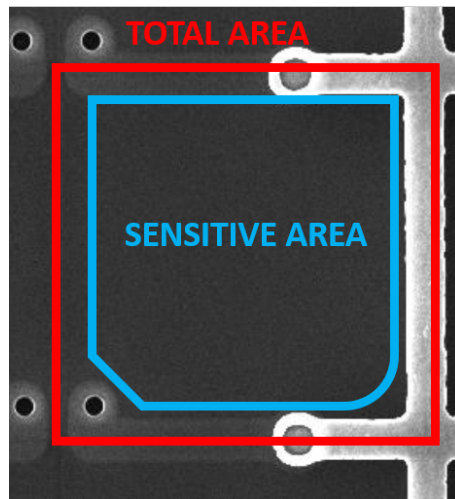**Figure 2.12:** SEM image of a SiPM cell. The red square is the total area, the blue line defines the sensitive area. Their ratio is the fill factor.
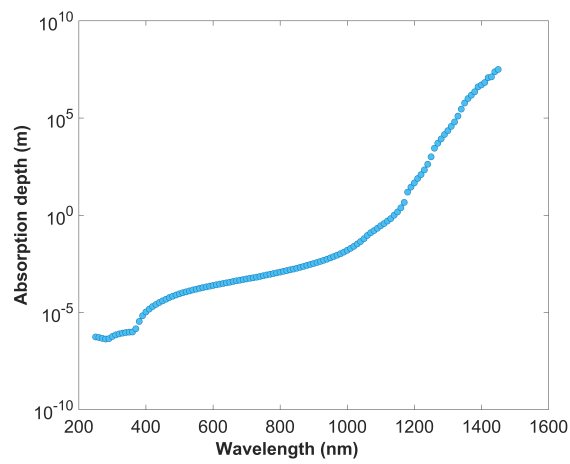


**Figure 2.13:** Absorption length in silicon as a function of the wavelength. Data from [69].

The trigger probability is the probability for a carrier to trigger an avalanche. This probability is linked to ionization coefficients of electrons and holes in silicon, $\alpha_e(x)$ and $\alpha_h(x)$ respectively [70]. $\alpha_e(x)$ and $\alpha_h(x)$ grow with the electric field, and the first is always larger than the second [71, 72]. As a consequence the trigger probabiltiy of electrons, $P_e(x)$, reaches higher values than the trigger probabiltiy of holes, $P_h(x)$, at any given bias of the junction. Furthermore, in a n-on-p device, the electric field forces the electrons to move from depth to the surface (from right to left in Fig. 2.14) and holes to the opposite direction [73], thus $P_e(x)$ and $P_h(x)$ have their maximum values on the right and on the left respectively. The total trigger probability, $P_T(x)$ can be defined as:

$$P_T(x) = P_e(x) + P_h(x) - P_e(x) \cdot P_h(x). \tag{2.3}$$

Fig. 2.14 shows a qualitative trend of $P_e(x)$, $P_h(x)$ and $P_T(x)$.
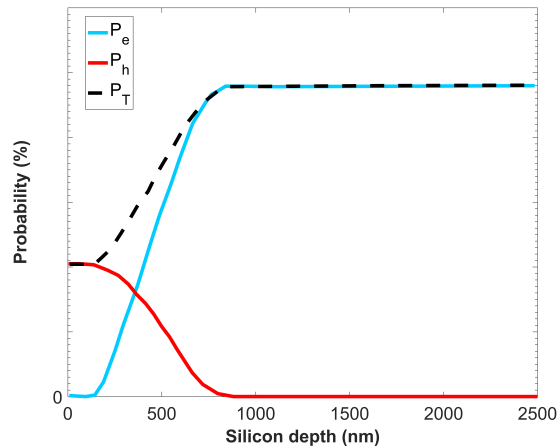


**Figure 2.14:** Qualitative plots of $P_e(x)$, $P_h(x)$ and $P_T(x)$ for a fixed over-voltage in a silicon n-on-p device.

As a consequence of the trigger probability trend the PDE is higher for the carriers generated in the p region of the junction. In addition, the PDE depends also on the specifc doping profiles used to build the p/n junction of the SiPM because the absorption depth in silicon depends on the wavelength, see Fig. 2.13. Combining these two dependences in the design SiPM process, manufactures have developed SiPM with different sensitivity as a function of the wavelength photons. FBK produces Red-Green-Blue (RGB) [74, 75, 76] SiPM for the visible light, Near-Ultra-Violet (NUV) [77, 48] SiPM, and in this last year Near-Infra-Red (NIR) [78]

and Vacuum-Ultra-Violet (VUV) [79] technologies.

We measure the PDE with the setup and method which are descibed in detail in [80, 81]. Similar setup are very common to determine the PDE of the SiPM [82, 83, 84]. Fig. 2.15 shows the main elements of our setup, which are contained inside a box to provide a dark condition. The basic element is an integrating sphere with
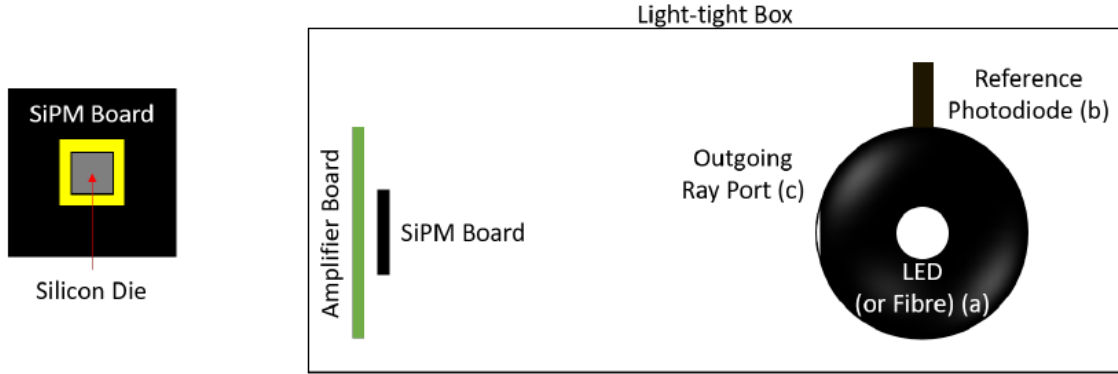


**Figure 2.15:** Scheme of the main components of the experimental setup inside the light-tight box [81].

inner diameter of about 5 cm, and three circular ports with a diameter of 1 cm. The port (a) is used to introduce the LED light into the sphere with an optical fibre. On the port (b) there is a reference photodiode to monitor the light stability and provide the photon rate impinging on the device. This reference photodiode requires a preliminary calibration described in detail in [80]. The port (c) is used to illuminate the device, which is ∼10 cm distant from the sphere to increase the light uniformity on its active area [82]. The LEDs used for the measurements are listed in Table 2.3. For each LED the typical uncertainty of photon rate at the device position was measured. Its value is ∼3% and includes the uncertainties on the device positioning, on the angle of incidence of the impinging photons, and on the light calibration [80]. With this setup we measure the absolute PDE because we are able to distinguish the charges truly induced by incident photons on the SiPM from the charges induced by cross-talk photons or after-pulses, as explained in detail in [80]. The used method is based on the analysis of the charge spectrum of the SiPM in low-level pulsed light illumination. A pulser drives the LED and provides the trigger to the oscilloscope. A characterization of the emission time of the LED is required in order to assure a complete collection of the photon generated

**Table 2.3:**  LEDs used to measure the PDE.

| Central $\lambda$ (nm) | FWHM (nm) | Manufacturer |
|:---:|:---:|:---:|
| **295÷305** | 15 | Roithner LaserTechnik |
| **315÷325** | 20 | Roithner LaserTechnik |
| **335÷355** | 20 | Roithner LaserTechnik |
| **363÷370** | 20 | Roithner LaserTechnik |
| **380** | 18 | Thorlabs |
| **393** | 18 | Roithner LaserTechnik |
| **397** | 16 | Roithner LaserTechnik |
| **407** | 20 | Thorlabs |
| **417** | 25 | Roithner LaserTechnik |
| **428** | 22 | Roithner LaserTechnik |
| **443** | 27 | Roithner LaserTechnik |
| **469** | 32 | Thorlabs |
| **518** | 34 | Thorlabs |
| **533** | 41 | Roithner LaserTechnik |
| **590** | 19 | Thorlabs |
| **639** | 23 | Thorlabs |
| **697** | 29 | Roithner LaserTechnik |
| **780** | 37 | Thorlabs |
| **944** | 24 | Roithner LaserTechnik |

events. The light pulse is very short (tens of nanoseconds) to assure a low level light regime and the oscilloscope window must be set to contain the entire signal duration (hundreds of nanoseconds). The charge of each acquired SiPM waveform is calculated to build a histogram exhibiting many peaks, each one corresponding to a different number of fired cells. Fig. 2.16 shows an example of this charge histogram for a 1x1 mm$^2$ SiPM.
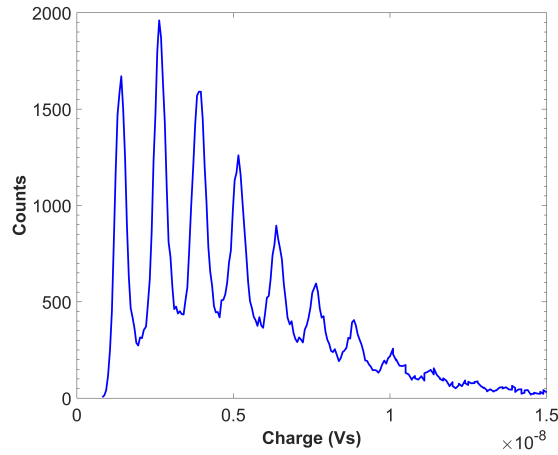


**Figure 2.16:** Typical charge histogram of a 1x1 mm$^2$ SiPM built in low-level pulsed light illumination. The first peak represents events in which no cells is fired.

When the number of fired cells is at least one, the probability P($\geqslant$1) to detect at least one photon follows a quasi-Poisson statistics because of the presence of the correlated noise. Instead, when no cell is fired, the corresponding histogram peak is originated by the integration of the baseline, so no correlated noise affects the number of events in this first peak. Thus, the probability of not detecting any photon, P(0), follows a Poisson statistics. Performing the measurement both in dark and in light condition, we obtained two histograms and two probabilities of no detection, P$_{Dark}$(0) and P$_{Light}$(0) respectively. The measurement in dark condition is necessary to subtract counts generated by the primary noise. From these two probabilities we calculate the average number of detected photons, N$_{Pulses}$, as:

$$N_{Pulses} = \ln \frac{P_{Dark}(0)}{P_{Light}(0)}, \qquad (2.4)$$

and substituting in Eq. 2.2, we obtain:

$$PDE = \frac{\ln \frac{P_{Dark}(0)}{P_{Light}(0)}}{N_{Photons}}. \qquad (2.5)$$

The number of incident photons, $N_{Photons}$, is measured with the reference photo-diode. The measurements are repeated for various bias voltages and LEDs.

## 2.2.3   Dark count rate, cross-talk, and after-pulsing

In SiPMs, there are two different types of noise, the primary noise and the correlated noise, which are related to different physical phenomena. The primary noise, also called Dark Count Rate (DCR) is due to the thermal generation of carriers in the depletion region. Instead, the correlated noise is due to a previous pulse, which can be photon or thermally generated. There are two main contributions to the correlated noise, After-Pulsing (AP) and Cross-Talk(CT). The AP is due to carriers trapped during an avalanche, and released at a later time, during the quenching of the avalanche discharge. The CT is due to photons escaped from one cell during an avalanche discharge that can be absorbed in adjacent cells. Fig. 2.17 shows a picture of a SiPM cross-section with a schematic of the different noise components, while Fig. 2.18 shows their contribution to the output signal.
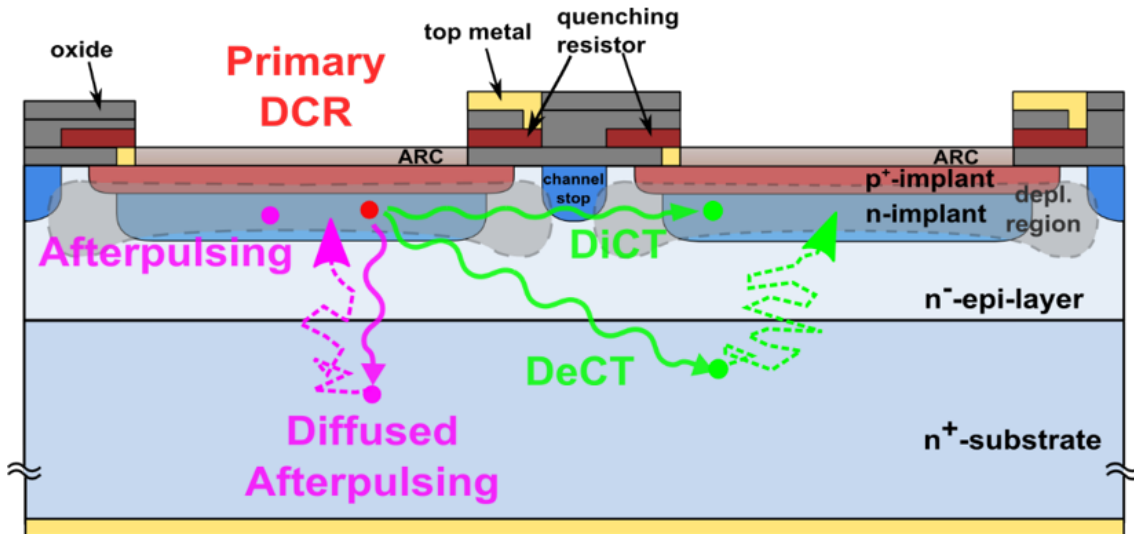


**Figure 2.17:**   Cross-section of SiPM microcells with different noise components: dark count rate, after-pulsing, direct and delayed cross-talk.

Dark Count Rate (DCR) are counts generated in absence of photons. These signals come from avalanches triggered by randomly generated carriers, and so follows the Poisson distribution. DCR has two different sources. The first is the thermal generation due to the Shockley-Read-Hall process [85]. This source dominates at
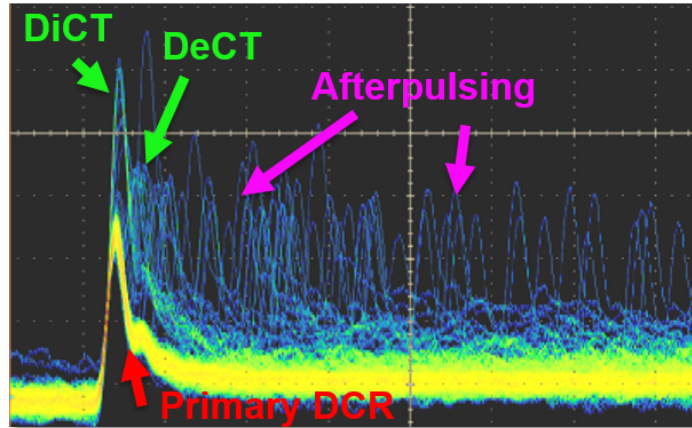
**Figure 2.18:** Example of SiPM waveforms acquired with the oscilloscope in dark conditions: all noise components are clearly visible.

room temperature and is drastically reduced at low temperature. DCR thermally generated can be reduced by improving wafer quality and reducing impurities with gettering techniques. The second DCR source is the band-to-band tunnelling generation, due to the tunnelling of the electrons from the valence to the conduction band [86]. This last source dominates at the lower temperatures. Fig. 2.19 shows a measurements of the DCR as a function of the temperature in a 25 $\mu$m-cell FBK NUV-HD SiPM: to note the change of DCR trend at ∼150 K.

After-Pulsing (AP) is due to carriers which are trapped during a primary avalanche and then released with a time delay, thus triggering another avalanche. The traps are defects and impurities in the semiconductor lattice, which produce energy levels in the forbidden band gap [86]. The AP probability depends on three factors:

- Trap capture probability: depends on the number of traps and on the number of carriers flowing during an avalanche, i.e. on the gain.

- Trap lifetime: depends on the trap level position, on the trap type, and on the temperature.

- Triggering probability: depends on the bias voltage and on the recovery condition of the microcells.

AP can be reduced by minimizing defects which may be introduced during the processing, and by decreasing the gain [86].
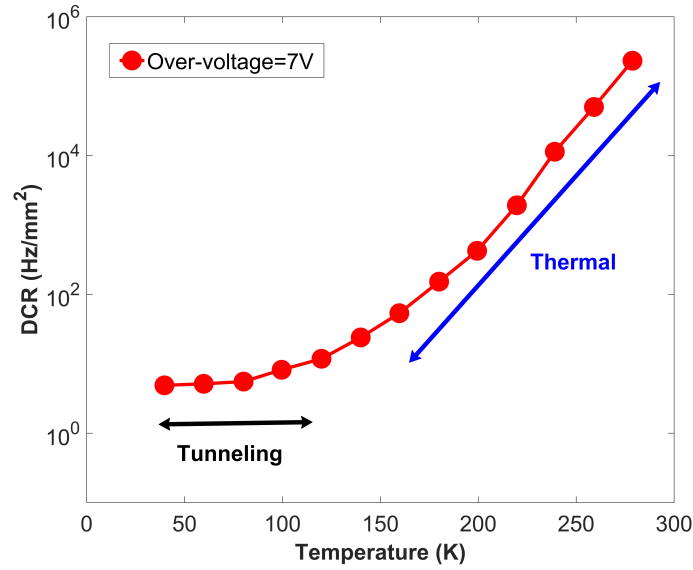
**Figure 2.19:** DCR as a funcition of temperature for a 25 $\mu$m-cell NUV-HD SiPM. It is clearly visible the trend change due to the different source of DCR.

Cross-Talk (CT) is a phenomenon which occurs mainly between adjacent cells. During an avalanche discharge, $\sim 3 \cdot 10^{-5}$ photons are emitted for each carrier crossing the junction with energy higher than 1.14 eV [87]. These photons can trigger an avalanche in adjacent cells. CT depends on the distance between high-field region of the microcells, and thus can be reduced using trenches in silicon, which can be also filled with opaque material, between the SiPM microcells, and reducing the microcell gain. Usually, CT pulses occur at the same time of the primary pulse, the so-called Direct Cross-Talk (DiCT), as shown in Fig. 2.18. Sometimes, a delayed component, called Delayed Cross-Talk (DeCT), occurs because of the carrier diffusion from substrate [88], see Fig. 2.17.

The quantification of the noise components is a fundamental step in the SiPM characterization because the noise influences the SiPM response. We measure DCR, DiCT, DeCT and AP with a method described in detail in [89]. Fig. 2.20 shows the measurement setup, which consists of a thermostatic chamber, to provide a stable temperature and dark condition, a transimpedance amplifier with a gain of 5000 V/A, to allow the analysis of single cell pulses, and a oscilloscope (Keysight Infinium S-Series), to acquire 1 ms-long waveforms with a sampling rate of 10 GS/s. The measurements are repeated to collect enough statistic to evaluate different parameters, for each bias and temperature condition. Fig. 2.21 shows an example of
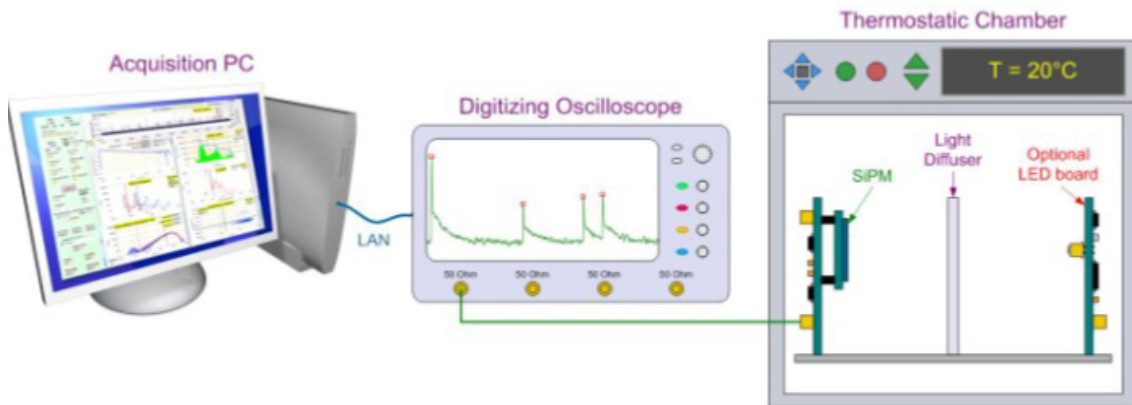
**Figure 2.20:**   The setup for the characterization of the noise of SiPMs.  Picture from [89], copyright 2012, IEEE.

an acquired waveform.  The analysis software filters signals with the DLED technique [90], and detects peak amplitudes and time intervals between peaks.  Inter-
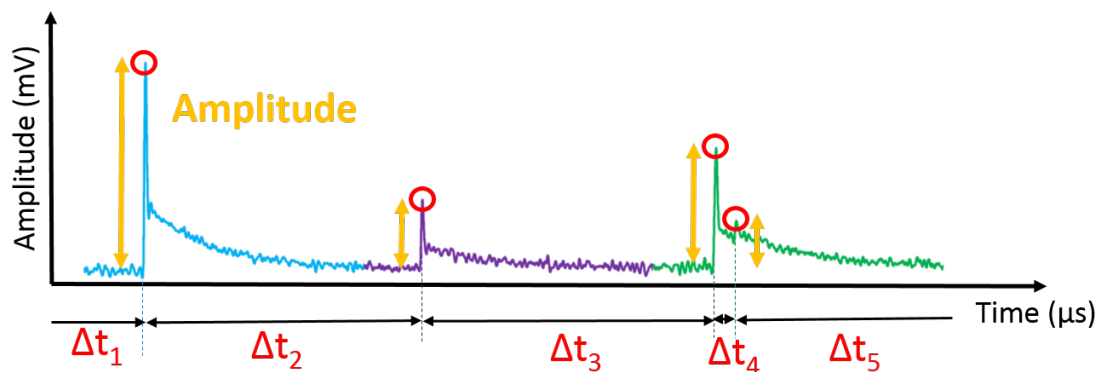


**Figure 2.21:**  Example of acquired waveform. Four peaks are detected by the analysis software, which saves amplitudes and time intervals between them.

arrival times and amplitudes are combined in a scatter plot, which is shown in Fig. 2.22.  In this plot, each point is the amplitude of an event as a function of its time distance from the preceding event.  The pulse amplitudes are normalized to the height of the single-cell signal.  All the different noise components (DCR, DiCT, AP and DeCT) are visible in the plot.  Primary dark counts follow a Poisson distribution and are represented by points with amplitude around 1.  DiCT is represented by points with amplitude exceeding 1 and with the same inter-arrival times of the primary DCR.  AP is represented by points with amplitude between 0.5 and 1 and
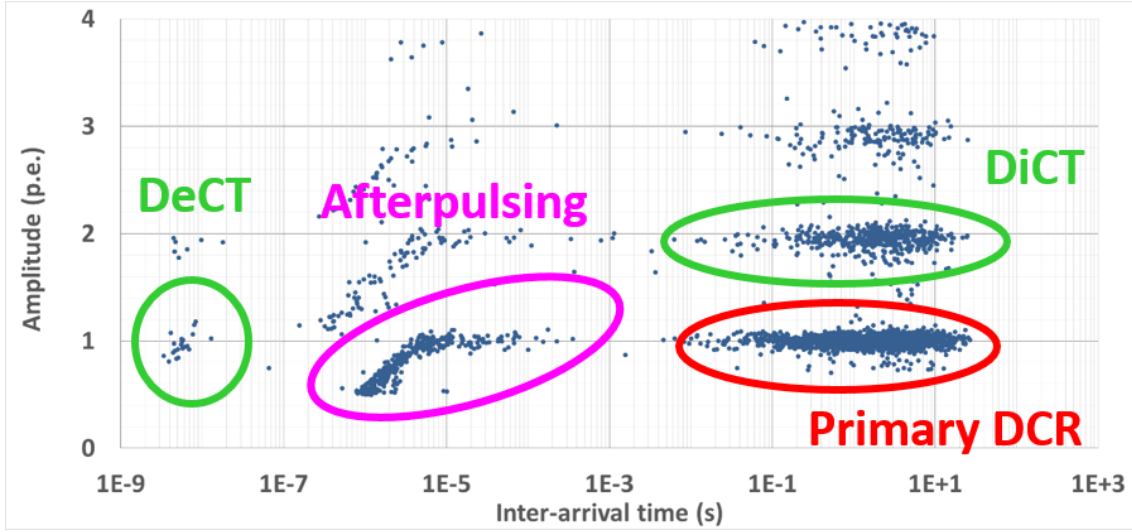
**Figure 2.22:** Example of a scatter plot of pulse amplitudes as a function of their distance from the preceding event at given bias and at liquid nitrogen temperature ($\sim$ -196 $^oC$). At this temperature, all the different noise components (DCR, DiCT, AP, and DeCT) are well distinguished.

inter-arrival times between 50 ns and 200 ns. AP with an amplitude lower than 0.5 is not measured because to identify pulses, a threshold on the amplitude must be imposed to avoid the collection of electrical noise. DeCT is represented by points with amplitude 1 located at very short inter-arrival times, between 5 ns and 20 ns.

To obtain quantitative information on the noise components it is useful to do projections of the scatter plot on the x-axis and on the y-axis. From the projection on the y-axis, an histogram of the amplitudes is generated, as shown in Fig. 2.23. Instead, from the projection on the x-axis, an histogram of the inter-arrival times is obtained, as shown in in Fig. 2.24. From the amplitude histogram, the total DCR and the DiCT probability are calculated as follows:

- Total DCR (Hz): is the sum of Primary DCR, AP and DeCT events and is the highest cumulative rate of the histogram.

- DiCT probability (%): is the probability that every event has to generate a single secondary cross-talk event and is the ratio between peak areas corresponding to the double, $A_2$, and single, $A_1$, events. Thus,

$$P_{DiCT} = \frac{A_2}{A_1}. \tag{2.6}$$

The inter-arrival times histogram allows the calculation of the following parameters:

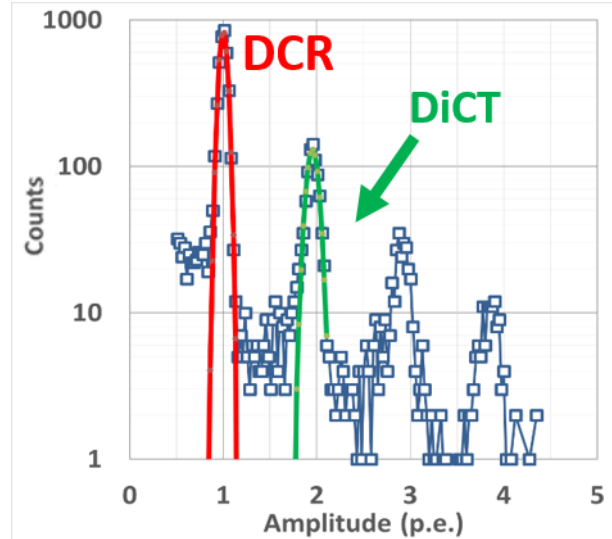**Figure 2.23:** Histogram of amplitudes, i.e. projection of the scatter plot, shown in Fig. 2.22, on the y-axis. The first peak represents the total DCR, the second peak is the DiCT. The time distribution of the events in both peaks follows the Poisson distribution.
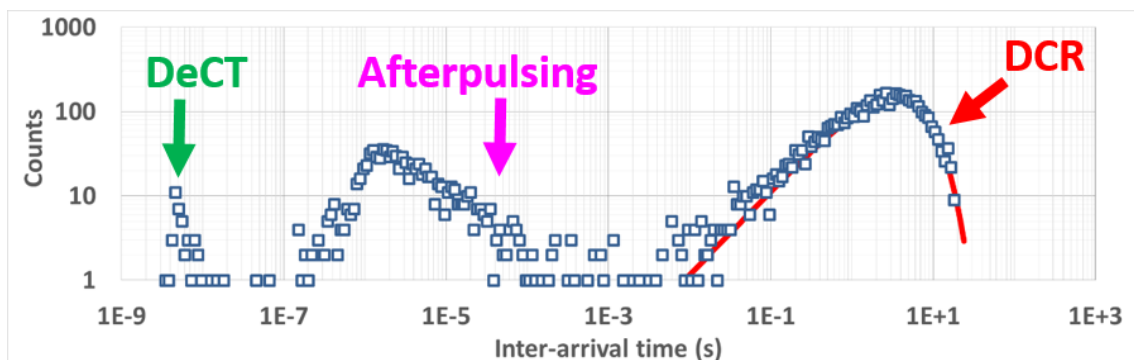


**Figure 2.24:** Histogram of inter-arrival times, i.e. projection of the scatter plot, shown in Fig. 2.22, on the x-axis.

- Primary DCR (Hz): is randomly generated, and as a consequence follows the Poisson distribution. Thus, the function that represents the primary DCR in the histogram is:

$$F_{DCR}(t) = a \cdot P_{DCR}(t) = a \cdot (t \cdot e^{-b \cdot t}), \tag{2.7}$$

where $a$ is a normalization coefficient, $P_{DCR}(t)$ is the probability to have an event at the time distance t, and b is the rate corresponding to the primary DCR. Primary DCR is obtained fitting the right part of DCR peak in the histogram of inter-arrival times, because at shorter time this peak is altered by correlated noise events.

- AP probability (%): ratio between the counts in excess of the DCR Poissonian fit and the total number of events for inter-arrival times above 50 ns, thus:

$$P_{AP} = \frac{N_{AP}}{N_{tot}}. \tag{2.8}$$

- DeCT probability (%): ratio between the counts in excess of the DCR Poissonian fit and the total number of events for inter-arrival times between 1 ns and 30 ns, thus:

$$P_{DeCT} = \frac{N_{DeCT}}{N_{tot}}. \tag{2.9}$$

All these operations are made on DLED filtered signals, but from original data it is possible extrapolate other parameters, such as gain, signal shape, and recharge time of the SiPM. By integrating in time the signal before each peak, it is obtained the baseline area. Instead, integrating for a certain time (according to the duration of the pulse) after each peak, it is obtained the pulse area. Fig. 2.25 shows the histogram of these areas: the baseline area and the pulse area. The SiPM gain is the distance between centroids of the single fired cell peak and the baseline peak.

Fig. 2.26 shows an example of signal shape of a SiPM. The blue line is the most probable signal, that is the average of the signal response for the single-cell events. It is visible a fast component and the exponential recovery of the cell, from which it can be extracted the time constant of the single cell. Instead, the red line is the average of the signal response of all events. This average gives a signal which is longer than the single cell signal because of the random presence of the correlated noise.
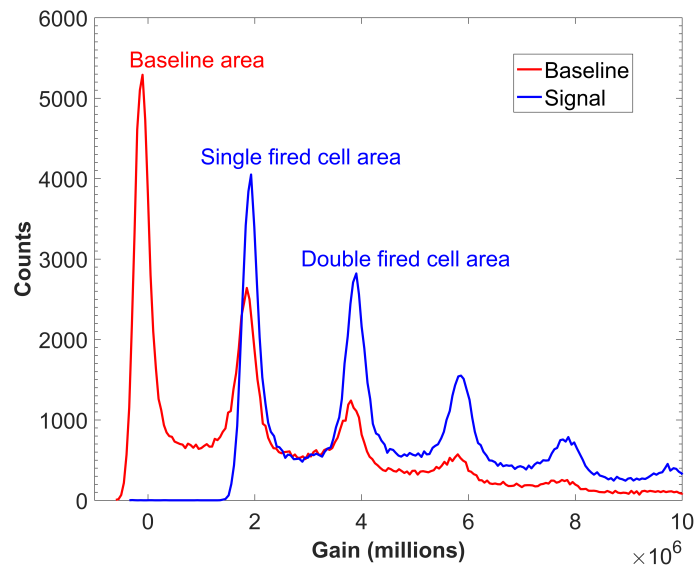
**Figure 2.25:** Histogram of the baseline area (from the time integration before peak signals) and of the pulse area (from the time integration after peak signals).
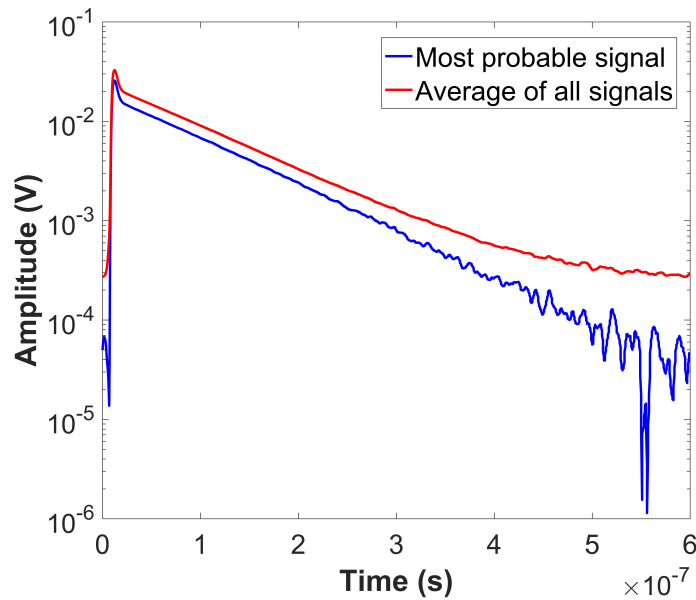


**Figure 2.26:** Most probable signal (blue line) and average of all events (red line). From the single cell signal is possible extrapolate the recovery time of the single cell.

## 2.2.4   Dynamic range

The dynamic range of SiPMs is limited by the finite number of their cells. SiPMs provide a good linearity as long as the number of impinging photons is lower than the number of cells, $N_{photons} << N_{cells}$. When this condition is not met, the SiPM response is non-linear. This behaviour can be described using Poisson distribution. The probability to have n-interactions in a cell i, $P_i(n)$, can be expressed assuming that the photons are evenly distributed across all the microcells, as:

$$P_i(n) = \frac{e^{-\frac{N_{photons} \cdot PDE}{N_{cells}}} (\frac{N_{photons} \cdot PDE}{N_{cells}})^n}{n!}, \qquad (2.10)$$

where $N_{photons}$ is the number of impinging photons, PDE is the SiPM photon detection efficiency, $N_{cells}$ is the number of SiPM cells, and n is the number of interactions. The number of SiPM fired cells, $N_{fired}$, is given by:

$$N_{fired} = N_{cells} \cdot (1 - P_i(0)) = N_{cells} \cdot (1 - e^{-\frac{N_{photons} PDE}{N_{cells}}}), \qquad (2.11)$$

where $P_i(0)$ is the probability to have 0-interactions, calculated using Eq. 2.10. Fig. 2.27 shows the estimation of the Eq. 2.11 as a function of the number of impinging photons, for an hypothetical SiPM with a number of cells from 1000 to 5000. It is clearly visible the non-linear response of the SiPM also when $N_{photons} \cong N_{cells}$.

Another linearity limiting factor is the recovery time of the cell, $\tau_{SiPM}$. When a cell is fired, it is not able to detect another photon for a time, called dead time, which depends on $\tau_{SiPM}$. However, if the distribution in time of photons, i.e. the photon rate, has a $\tau_{Light} > \tau_{SiPM}$, a single cell of a SiPM can be triggered more than once in the $\tau_{Light}$ interval. This re-trigger capability improves the linearity of SiPMs.

Thus, a way to reduce the non-linearity is to increase the density of cells, cells/mm$^2$, in a SiPM reducing their size. Standard SiPMs have a cell size from 100 $\mu$m to 40 $\mu$m and a cell density from $\sim$100 to $\sim$625 cells/mm$^2$. Fondazione Bruno Kessler (FBK) has recently introduced High-Density(HD) [48, 75] and Ultra High-Density (UHD) [76] SiPMs, featuring very small micro-cell pitch from 25 $\mu$m to 5 $\mu$m and a cell density from $\sim$1600 to $\sim$46200 cells/mm$^2$. Moreover, the small cell size provides an ultra-fast recovery time, in the order of a few of nanosecond for the smallest cells. The high cell density and the short recovery time are very important factors to improve the linearity of the SiPM in high-dynamic-range applications,
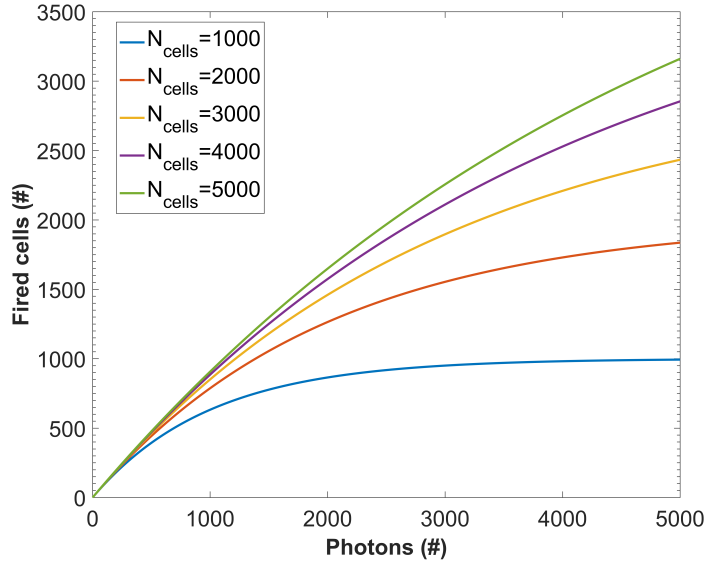
**Figure 2.27:** Estimation of the Eq. 2.11 as a function of the number of impinging photons, for an hypothetical SiPM with number of cells from 1000 to 5000.

such as the scintillation light readout in high-energy gamma-ray spectroscopy and in prompt gamma imaging for proton therapy. The reduction of the cell size has also a drawback, that is a decreasing of the PDE because of the lower fill factor, and as a consequence a worsening of the energy resolution. Thus, it is not sufficient to evaluate the linearity of the SiPM but it is necessary to evaluate how the cell density impacts on global performance of the SiPM. We characterize the non-linear SiPM behaviour with a setup and method described in detail in the Sec. 3.3.

## 2.2.5   Single photon time resolution

Another interesting feature of SiPMs is their excellent Single Photon Time Resolution (SPTR). The response is determined by avalanche discharge and is in the order of few hundreds of ps [91]. The major contribution at timing performance is due to the statistical fluctuations of the current growth due to the photo-conversion depth, a vertical build-up at the beginning of the avalanche, and a lateral propagation of the avalanche. Single Photon Time Resolution is important in many applications, for example it has a direct influence on the best achievable time resolution of time-of-flight (TOF) detectors when are used with scintillators [92]. In TOF for positron emission tomography (PET) the state of the art at the time of this writing is a

coincidence resolving time of ∼85 ps full-width at half-maximum (FWHM), using a
NUV-HD SiPM [48] coupled to a small LSO:(Ce,Ca) codoped scintillator [93].

## 2.3  HD and UHD SiPM technologies

As presented in Sec. 1.4, GammaRAD project aims at developing a gamma-ray
detection module based on SiPMs coupled to LYSO scintillators, and at validating
it in PGI applications. RGB SiPM [74] has been chosen among SiPMs available at
FBK to produce the detector. In principle, NUV SiPM technology is better suited
for LYSO than RGB SiPM technology, but NUV technology provides only cell size
with dimensions higher than 25 $\mu$m. Instead, although the typical PDE as a function
of wavelength of the RGB SiPM technology, shown for example in Fig. 2.28, does
not match exactly the emission wavelength of the LYSO, this technology currently
allows the production of SiPMs with the smallest cell size. Having a high cell
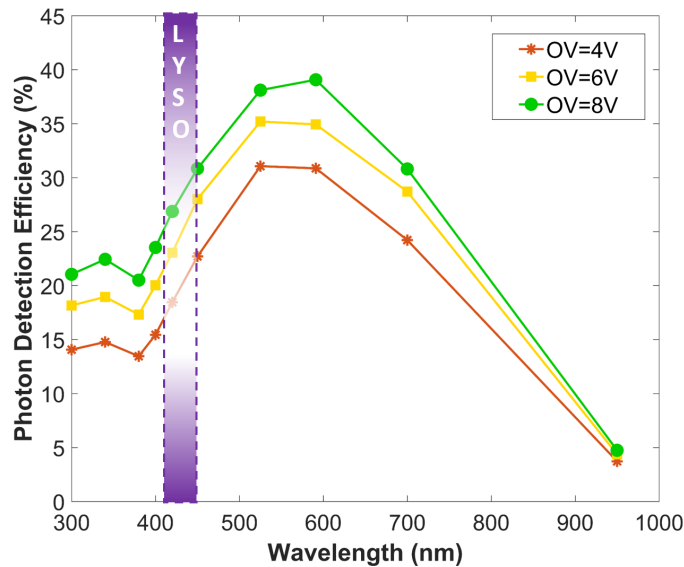


**Figure 2.28:** PDE as a function of the wavelength for RGB-HD SiPM (25 $\mu$m) at different
over-voltage. The purple box indicates the LYSO emission wavelength. The PDE was measured
with the method described in Sec. 2.2.2.

density is extremely important to improve the linearity of the SiPM and to avoid
the compression of the energy spectrum at high energies, which worsens the energy
resolution and makes difficult the calibration of the detector. Furthermore, small
cells have a lower gain, thus lower correlated noise, and faster recharge time which

reduces pile-up. An additional advantage of small cells for PGI is also their increased radiation hardness [51].

Standard RGB SiPMs [74] have a n-on-p structure and cell size of 40 $\mu$m and 50 $\mu$m. Fig. 2.29 (a) shows in detail the cross section of the n-on-p structure. Fig. 2.29 (b) shows the dead border region around each SPAD for the standard technology: microcells are isolated by a p-stop, which introduces a dead border of $\sim$4.5 $\mu$m around the active area. This standard technology was improved with the
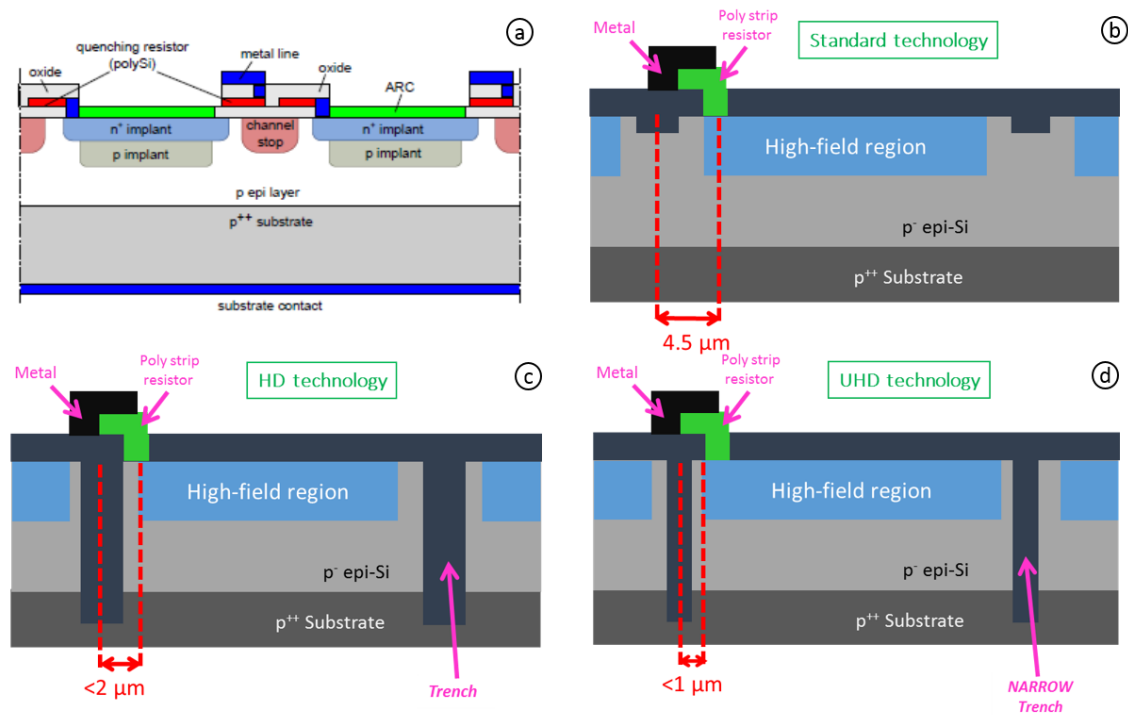


**Figure 2.29: a)** The RGB-SiPM cross section showing the n-on-p structure of the detector; the p implant define the SPAD active area; ARC is an anti-reflective coating layer to enhance light transmission [74]. **b)** Schematic cross section of a standard RGB SiPM which shows a dead border region between cells of 4.5 $\mu$m. **c)** Schematic cross section of a RGB-HD SiPM [94] which shows a narrow border region around cells lower than 2 $\mu$m. **d)** Schematic cross section of a RGB UHD SiPM [94] which shows a narrow border region around cells lower than 1 $\mu$m.

High-Density (HD) version [75] with cell size between 25 $\mu$m and 15 $\mu$m. RGB-HD SiPMs are produced using a lithography technology with smaller critical dimensions and designed with trenches among SPADs, see Fig. 2.29 (c). Trenches are used both for electrical and optical isolation of the cells, thus allowing a reduced optical crosstalk (both primary and delayed). Small cells have a lower gain, which helps to reduce correlated noise, such as AP and CT. The trenches provide a smaller

dead border around cells increasing the FF and thus limiting PDE losses, even with smaller cell size. Fig. 2.30 shows a SEM image of the 15 $\mu$m-cell RGB-HD layout, and a detail of trenches during the production process. The latest development of
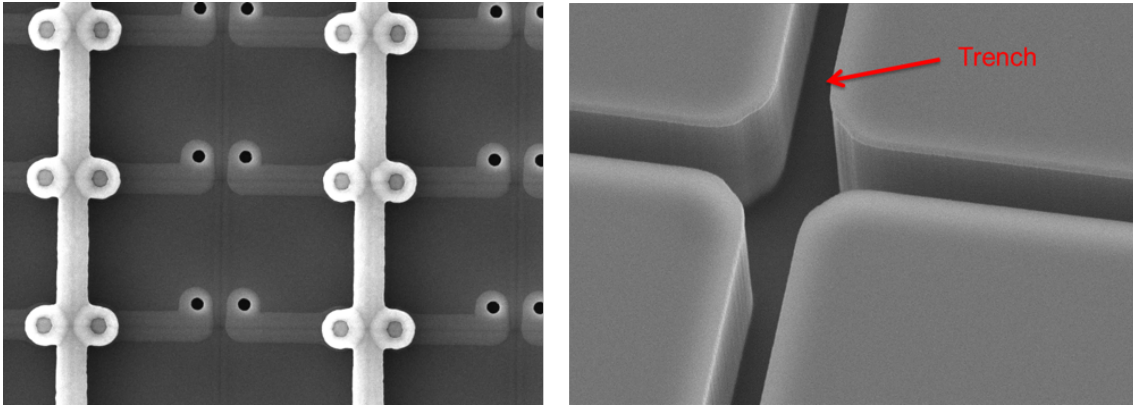


**Figure 2.30:** SEM image of the 15 $\mu$m-cell RGB-HD SiPM (right) whit a detail of trenches between SPADs (left).

the RGB technology is the Ultra-High-Density (UHD) version. UHD SiPMs push the limits of the HD technology even further, by reducing all the feature sizes, such as contacts, resistors, and the border region around cells. UHD SiPMs have hexagonal cells in a honeycomb configuration with a circular active area, as shown in a SEM image in Fig. 2.31. Dead border region around cells is lower than 1 $\mu$m, see Fig. 2.29 (d). Fig. 2.32 shows an interesting comparison among the cell layouts
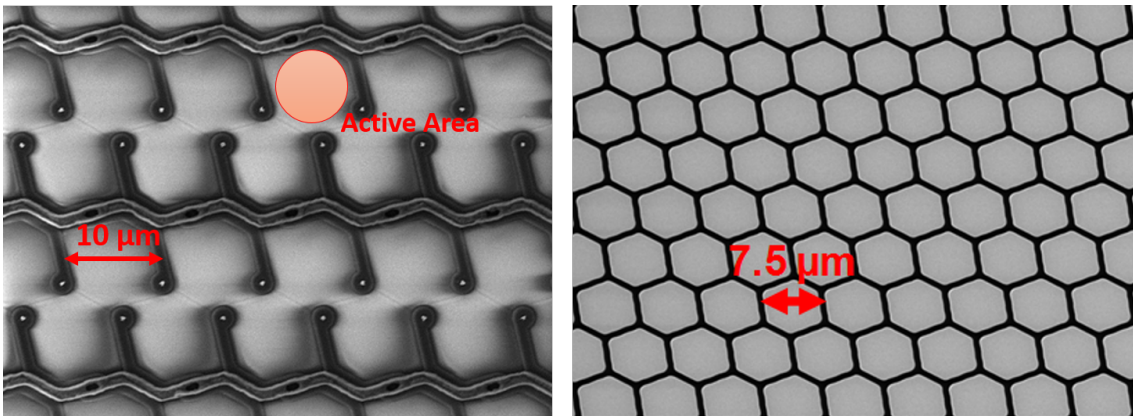


**Figure 2.31:** SEM images of the 10 $\mu$m-cell (right) and 7.5 $\mu$m-cell (left) SiPMs. To note the honeycomb layout and the circular active area.

of three RGB technologies. The reduction of the dead border can improve the FF in smaller cells although FF usually decrease as cell size decreasing. This phenomenon
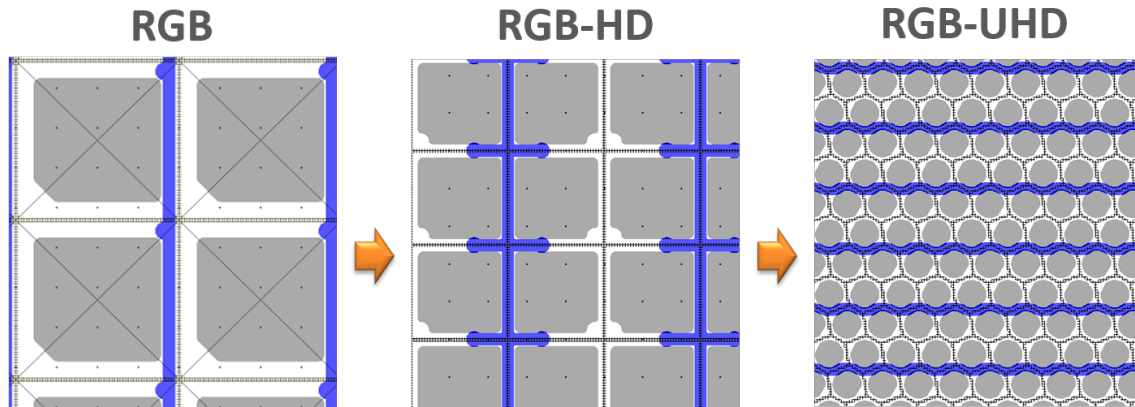
**Figure 2.32:** Comparison among three RGB technologies: 40 $\mu$m-cell for standard RGB, 25 $\mu$m-cell for RGB-HD and 7.5 $\mu$m-cell for RGB-UHD.

is clearly visible in Fig. 2.33, which represents the trend of the FF of each RGB technology. Inside each technology, the FF decreases as the cell size decreasing,
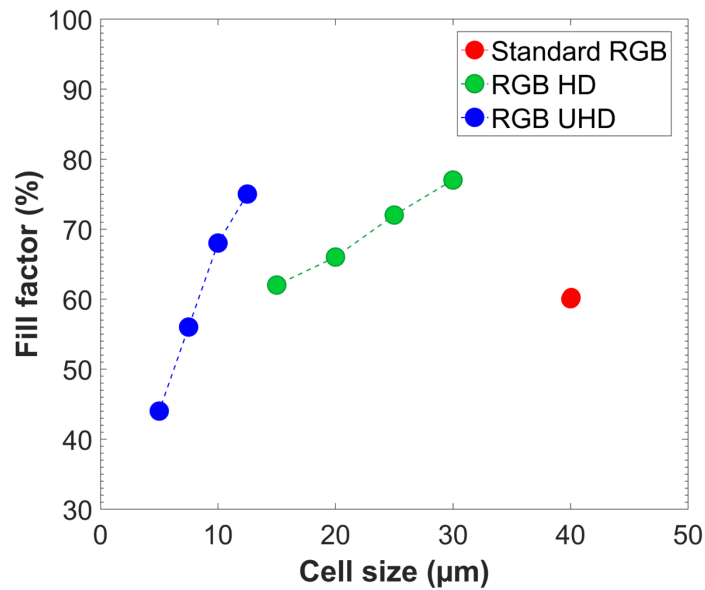


**Figure 2.33:** Fill Factor of the different RGB technologies as a function of the cell sizes.

as expected. Instead, among the technologies, the series are shifted because of the gain in FF, due to the small trenches of the newest HD and UHD SiPMs. As a consequence of the higher FF of the small cells, the PDE loss is lower. In addition, HD and UHD SiPMs have a lower quenching resistance, thus a faster recharge, which further increases the dynamic range of the SiPM. These improvements can be

advantageous for the energy resolution of a SiPM, which is an important parameter in gamma-spectroscopy applications. Summarizing, the cell size has a big impact on performance of the detector because is strongly related with gain, FF, and number of cells. These three parameters are themselves related to the main parameters which are used to define performance of a detector: noise, PDE, linearity, and energy resolution. To study how the modification of the cell size impacts on global performance of the SiPM we have characterized the RGB-HD and RGB-UHD SiPMs. The results of the characterization are presented and commented in Chapter 4.

# Chapter 3

# Gamma ray detection with SiPM

In this chapter, we present a brief overview on scintillation detectors, on the interactions of gamma-rays with materials, and on the LYSO scintillator crystal, which is used in this work. Then, we introduce the study of the energy resolution and non-linearity in the specific case of SiPMs coupled to scintillators. In the last part of the chapter, we describe an experimental setup that is used to measure the energy resolution with low energy gamma radioactive sources, called scintillator setup. In addition, we present a setup that was developed to simulate the detection of high-energy gamma photons, called LED setup. This last setup can be exploited for the study of the energy resolution and non-linearity for applications of high-energy gamma-ray spectroscopy and prompt gamma imaging in proton therapy.

# 3.1 Scintillation detectors

Scintillation detectors are based on scintillator materials, which generate secondary low-energy photons, usually in the visible spectrum, as a response to high-energy incident radiation. The scintillator is coupled to a photo-detector, which converts the scintillator light into an electrical signal. Different scintillator materials provide different features in terms of time response, detection efficiency, sensitivity at several radiation types, and detection area. When an ionizing radiation interacts with a scintillator material, a fluorescent flash, known as scintillation, is produced.

## 3.1.1 Interaction with gamma-rays

In gamma rays detection, scintillation is the result of the excitation of bound electrons by means of fast electrons inside the scintillator. These electrons are generated by three types of mutual interactions: photoelectric effect, Compton effect, and pair production. The probability of occurrence of these interactions depends on the scintillator type, and on the gamma-ray energy.

In the photoelectric effect, an incident gamma-ray is absorbed, and a photoelectron is ejected from one of the electron shells of the absorber atom [95], as shown in Fig. 3.1 (a). The photoelectron appears with an energy $E_{e^-}$ given by:

$$E_{e^-} = h\nu - E_b, \tag{3.1}$$

where $h\nu$ is the energy of the incoming gamma ray, and $E_b$ is the binding energy of the shell from which electron is emitted. The vacancy created by the electron emission can be filled by other electrons. In this rearrangement, the binding energy is realesed either in the form of a characteristic X-ray or Auger electron. Thus, the result of the photoelectric absorption is the ejection of a photoelectron, carrying the most of the gamma-ray energy. This photoelectron can be followed by one or more low energy electrons, generated by the absorption of the original binding energy of the photoelectron. As a consequence, the energy spectrum of the photoelectric effect is ideally a single peak with a total electron energy corresponding to the energy of the incident gamma rays. The amount of scintillation photons produced by photoelectric effect is, as a first approximation, proportional to the gamma-ray energy [95].

In the Compton effect, the incident gamma-ray photon scatters with an electron in the absorbing material. In this scattering phenomenon, the incoming gamma-ray photon is deflected of an angle $\theta$ with respect to its original direction, as represented in Fig. 3.1 (b). Thus, the photon transfers only a portion of its energy to an



(a) Photoelectric effect          (b) Compton effect
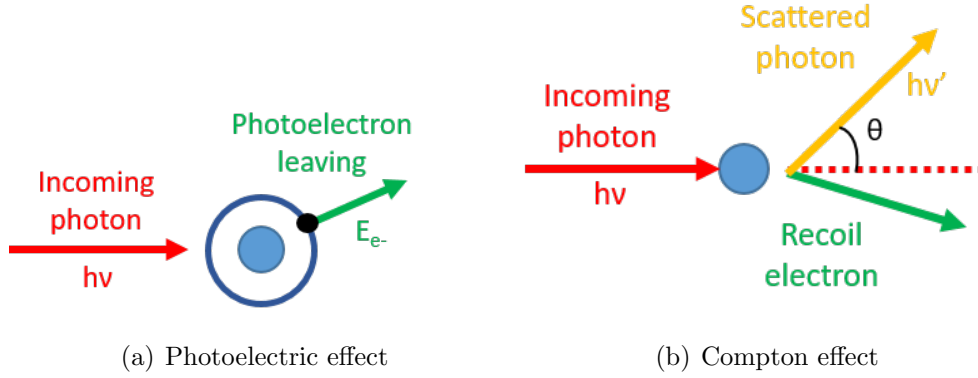
**Figure 3.1:** Schematics of the photoelectric effect (a) and of the Compton effect (b).

electron, called recoil electron. The remaining energy of the the scattered photon $h\nu'$, assuming that the recoil electron is initially at rest, is given by:

$$h\nu' = h\nu \cdot \frac{1}{1 + \alpha \cdot (1 - \cos(\theta))},\qquad(3.2)$$

where $h\nu$ is the energy of the incoming photon, $\theta$ is the deflection angle, and $\alpha$ is:

$$\alpha = \frac{h\nu}{m_0 c^2},\qquad(3.3)$$

where $m_0 c^2$ is the rest mass of the electron, 0.511 MeV. The kinetic energy of the recoil electron is given by:

$$E_{e^-} = h\nu - h\nu'.\qquad(3.4)$$

A continuum of energy can be transferred to the electron, from zero up to the maximum energy, because all scattering angles can occur in a Compton scatter. When $\theta = \pi$, the maximum energy is transferred to the electron. As a consequence, in the energy spectrum this corresponds to the so called Compton edge.

In the pair production effect, a photon passing near the nucleus of an atom, is subjected to strong field effects from the nucleus and may be absorbed. The photon energy is fully converted in an electron-positron pair, $e^-$ and $e^+$, which are created in the energy/mass conversion of the incoming photon. The pair production process

may occur when the incoming photon has an energy $h\nu \geqslant 1.022$ MeV, because the energy needed to create one $e^-/e^+$ pair at rest is $2\times0.511$ MeV. The kinetic energy of the produced particles is:

$$E_{e^+} + E_{e^-} = h\nu - 1.022. \tag{3.5}$$

Usually, this kinetic energy is lost inside the material after a travel of few millimetres.

Fig. 3.2 shows two examples of the response of a detector for low energy events, and high energy events. In these examples, the detector has an intermediate size, which is the usual size of a real detector for gamma-ray spectroscopy, thus it is larger than the mean free path of the secondary gamma radiations (1-2 cm), but it is small enough to permit to a secondary radiation to escape without interacting with the detector active volume. The first spectrum (left) is related to low energy events and it shows photoelectric peak and Compton edge. The second spectrum (right) is related to high energy events, and thus the pair production effect is dominant. The annihilation photons are emitted by the annihilation of $e^+$, which are generated by the primary photon, and can interact with the detector or escape. The double escape peak occurs when both annihilation photons escape without interaction in the detector. The single escape peak occurs when one photon escapes but the other is totally absorbed.

Fig. 3.3 shows the relative importance of these three processes of interaction, i.e. photoelectric effect, Compton effect, and pair production effect, as a function of the incoming photon energy. It is visible that in high Z-materials, the photoelectric effect dominates at low energy, and the pair production at high energy. On the other hand, in low Z-material the Compton scattering dominates at medium energy.

### 3.1.2 LYSO:Ce scintillator

Scintillator materials can be divided into two groups: inorganic and organic. Inorganic scintillators are made of natural crystals or artificial crystals. Artificial crystals can be produced starting from many natural crystals adding doping impurities. Dopant atoms are intentionally added impurities, which are also called activators, because they are responsible for the scintillation process. These activator impurities provide energy levels in the energy band gap of a crystal. These levels allow to the excited electrons to relax by emitting photons. Furthermore, the activator impurities are chosen to make the crystals transparent at the photon emission
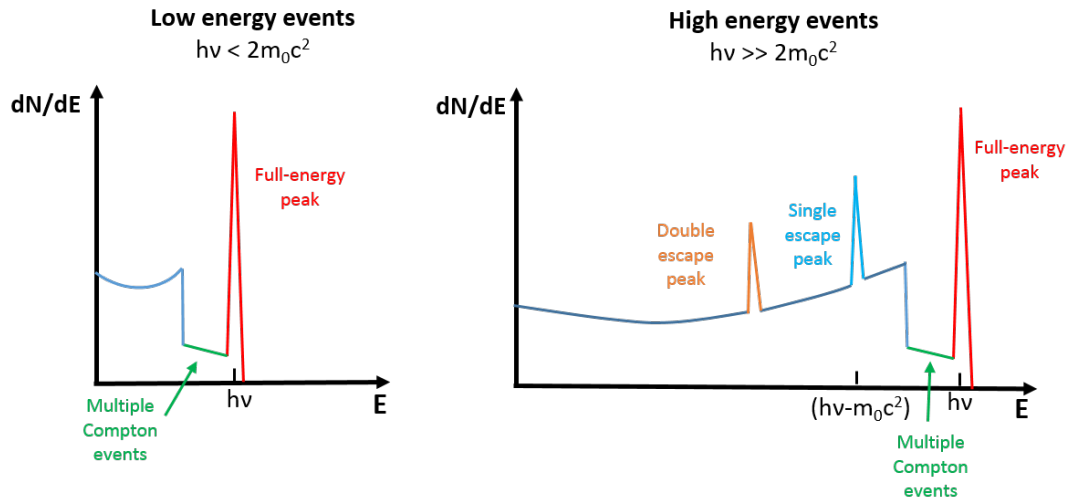
**Figure 3.2:** Example of the response spectrum of a scintillator detector. The spectrum on the left is relative to low energy events, i.e. photoelectric effects and Compton edge. The spectrum on the right describes the situation for high energy events, i.e. pair production and Compton edge. Data from [95].
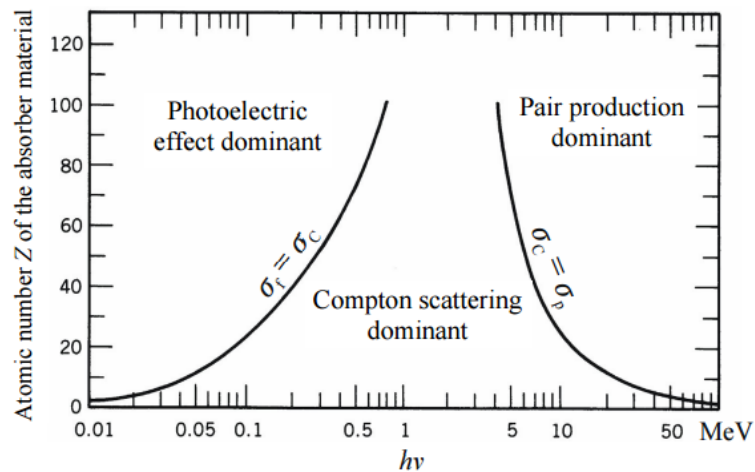


**Figure 3.3:** Relative importance of various processes of gamma radiation interaction with matter as a function of the incoming photon energy, and of the atomic number of the material [96].

frequency, avoiding self-absorption of the emitted light. Most of the inorganic scintillators offer excellent energy conversion efficiency, high absorption efficiency, and a high probability of the photoelectric effect compared to organic scintillators. These last scintillators are made of organic compounds, which are mixed with polystyrene to form a rigid plastic, or with mineral oil to form a liquid. Plastic scintillators are used as slabs or fibers, and are cheaper than inorganic scintillators. Instead, liquid scintillators are useful to fill large volume or to circulate to minimize radiation damage. Organic scintillators have a short decay time, low density, and high sensitivity to fast neutrons because of the high proportion of hydrogen. For these reasons, they are not suitable for the detection of high-energy gamma-ray, as required in prompt gamma imaging. Table 3.1 presents inorganic scintillators which are commonly used in gamma-ray spectroscopy.

**Table 3.1:** Physical properties of common inorganic scintillators [97, 98, 99]. The light yield is the number of photons emitted per keV of deposited energy over a $4\pi$ solid angle.

| Scintillator | Light Yield (ph/keV) | Decay $\tau$ (ns) | Emission $\lambda$ (nm) | Density (g/cm$^3$) |
|---|---|---|---|---|
| $LaBr_3(Ce)$ | 63 | 16 | 380 | 5.08 |
| $NaI_3(Tl)$ | 38 | 250 | 415 | 3.67 |
| $Lu_{1.8}Y_{0.2}SiO_5(Ce)$ | 30 | 45 | 420 | 7.1 |
| $CsI(Tl)$ | 54 | 1000 | 550 | 4.51 |
| BGO | 8-10 | 300 | 480 | 7.13 |
| $Gd_3Al_2Ga_3O_{12}(Ce)$ | 46 | 80-800 | 520 | 6.67 |
| $Lu_2SiO_5(Ce)$ | 27 | 40 | 420 | 7.4 |

The choice of the scintillator material is fundamental in a detector because it has an impact on the detection efficiency, the energy resolution, and the time resolution. Among common crystals available on the market, see Table 3.1, the $Lu_{1.8}Y_{0.2}SiO_5(Ce)$, briefly LYSO(Ce), was chosen to build the detector for Gammarad project. All other materials were discarded for different reasons, such as long decay times, low density, poor energy resolution, and hygroscopicity. Summarizing, the main reasons for LYSO (Ce) choice are:

- Fast response: useful to reduce pile-up in high count rate.

- High density: useful to maximize gamma rays detection, and to minimize neutron detection.

- Emission wavelength: characteristic emission in the range of quite high photo detection efficiency of the RGB SiPM.

- High light yield: useful to improve energy resolution.

- Not hygroscopic.

Furthermore, we decided to use a pixelated crystal which is made of an array of small blocks. This geometry provides several advantages. First, interaction coordinates can be provided by crystal segment identification. Second, small pixels reduce the light spread because they guide the light generated in a single event on a single photo-sensor of the photo-detector. Indeed, is it possible to couple 1:1 the scintillator pixel and the photo-detector to reduce the probability of pulse piling-up at high count rate, and to provide 2D spatial information.

A possible drawback of the LYSO crystal is the presence of a Lutetium radioactive isotope, $^{176}$Lu. This isotope is a natural beta emitter and decays in the 99,66% of the cases to the 597 keV excited state of $^{176}$Hf. This exited state decays with three gamma-rays of 307 keV, 202 keV, and 88 keV. Fig. 3.4 shows the LYSO energy spectrum generated by a LYSO crystal with a diameter of 1", and long 1". The upper energy of this spectrum is $\sim$1.2 MeV. This energy is lower than the energy range of interest for the detection of prompt gamma-rays, which starts at $\sim$2 MeV. Thus, the self-radioactivity of LYSO does not represent a limit in prompt gamma imaging and high-energy gamma-ray spectroscopy applications.

## 3.2 Characterization of SiPM coupled to scintillator

Important requirements for a radiation detector, especially in Prompt Gamma Imaging (PGI) applications, are the ability to discriminate the different energies over the whole dynamic range, and the ease of calibration. These requirements can both be correlated to a good energy resolution, and to a low non-linearity of the detector. The ease of calibration is a practical requirement for the use of the detector in a real environment, that of proton therapy.
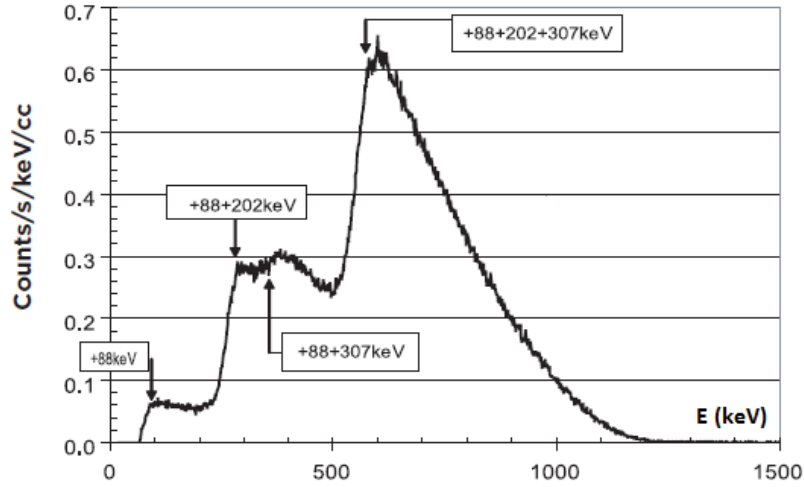
**Figure 3.4:** Spectrum of the beta self-activity of LYSO provided by Saint Gobain for a LYSO crystal with a diameter of 1", and 1" long [100].

## 3.2.1 Energy resolution

The energy resolution of a gamma-ray spectroscopy system, which consists of a photo-detector coupled to a scintillator crystal, can be expressed as [101]:

$$\left(\frac{\Delta E}{E}\right)^2 = (R_i)^2 + (R_t)^2 + (R_{stat})^2 + (R_{el})^2, \tag{3.6}$$

where $R_i$ is the intrinsic resolution of the crystal, $R_t$ is the transfer resolution, $R_{stat}$ is the statistical resolution, and $R_{el}$ is the noise resolution.

The intrinsic resolution of the crystal is associated with the non-proportional response of the scintillator, inhomogeneities in the scintillator structure which generate local variations in the light output, and with imperfect reflection conditions at the surface of the crystal [95]. This component is independent on the photo-detector characteristics.

The transfer resolution is the variance associated with fluctuations of the probability that a photon generates a photo-electron in the SiPM. This component depends on the quality of the optical coupling between a crystal and a photo-detector, on the homogeneity of the quantum efficiency of the photo-detector, and on the efficiency of charge collection. In modern scintillation detectors this component is negligible [102].

The statistical resolution is associated with statistical fluctuations, from pulse to pulse, of the number of photons generated in the scintillator, and detected by

the detector, for the same energy of the gamma photon. These fluctuations are the statistical noise that is due to the charge generated within the detector by a quantum of radiation, which is a discrete number of charge carriers instead that a continuous variable. In an ideal detector the number of detected photons should follow the pure Poisson statistics. On the other hand, in a real detector the Poisson statistics is worsened by the Excess Noise Factor (ENF) of the detector.

The last component, is the noise resolution which is due to the dark current of the photo-detector and to the electronic noise of the front-end. Both these sources add fluctuations to the output signal and degrade the energy resolution.

In detail, when a photo-detector coupled to a scintillator crystal is a silicon photomultiplier, Eq. 3.6 can be written as:

$$\left(\frac{\Delta E}{E}\right)^2 \cong (R_i)^2 + \frac{ENF}{PDE \cdot N_{ph}} + \frac{ENF \cdot DCR \cdot T_{int}}{\left(PDE \cdot N_{ph}\right)^2} + ... =$$

$$(R_i)^2 + (R_{stat})^2 + (R_{el})^2 \,, \tag{3.7}$$

where in $R_{el}$ the electronic noise of the front-end is neglected because of the high gain of SiPMs. The statistical resolution, $R_{stat}$, depends on the PDE, and on excess noise factor (ENF) of the detector. Usually, the ENF describes the statistical noise caused by the SiPM correlated noise (cross-talk and afterpulse) [103]. But, the saturation of the SiPM causes a compression of the energy spectrum, and thus a loss of information and a worsening of the energy resolution. This phenomenon can be represented as an additional ENF due to non-linearity of the SiPM. Thus, it is possible include in the ENF the effects of both the correlated noise and the non-linearity of the SIPM, as described in [104]. From Eq. 3.7, the energy resolution is a trade off between PDE and ENF: for small cell size, the saturation and correlated noise are low (thus ENF is low), but also PDE is low. The situation is the opposite for large cell size.

## 3.2.2   Non-linearity

The analysis of the non-linearity (NL) is based on the following equations:

$$C_{measured} = c_1 \cdot N_{cells} \cdot \left(1 - e^{-\frac{c_2 \cdot PDE \cdot E}{N_{cells}}}\right), \tag{3.8}$$

$$C_{ideal} = c_1 \cdot c_2 \cdot PDE \cdot E. \tag{3.9}$$

$C_{measured}$ is the amount of charge generated in the SiPM by impinging photons. $C_{ideal}$ is the limit of $C_{measured}$ at low energy when the response of the SiPM is linear. $N_{cells}$ is the number of cells of the SiPM, PDE is the photo detection efficiency of the SiPM, and E is the energy of the impinging photons. Instead, $c_1$ and $c_2$ can be expressed as:

$$c_1 = G_{SiPM} \cdot G_{Amplifier} \cdot q \cdot 10^6, \tag{3.10}$$

$$c_2 = LY \cdot \alpha \cdot ENF, \tag{3.11}$$

where $G_{SiPM}$ is the gain of the SiPM, $G_{Amplifier}$ is the gain of the amplifier, q is the charge of the electron, LY is the light yield of the scintillator crystal, $\alpha$ is the light collection coefficient, and ENF is the excess charge factor.

    Fig. 3.5 (a) shows an example of measurements of $C_{measured}$ and $C_{ideal}$. The blue line is the real response, which depends on the number of cells of SiPMs, on the PDE, and on the energy of the radiation. By increasing the number of cells of a SiPM, ideally to infinity, the real response tends to the ideal one, which is the green line in Fig. 3.5. The non-linearity can be expressed as the deviation from the linear response:

$$NL = 1 - \frac{C_{measured}}{C_{ideal}}. \tag{3.12}$$

    Fig. 3.5 (b) shows the typical trend of the non-linearity.

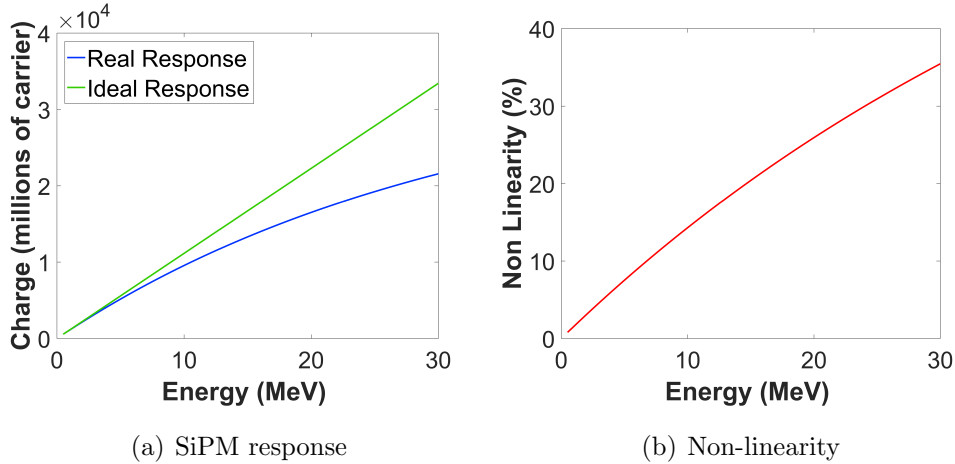(a) SiPM response               (b) Non-linearity

**Figure 3.5:** (a) Example of the responses of a SiPM as a function of the energy simulated with the LED setup, which will be described in Sec. 3.3. The blue line is the real response of a 4x4 mm$^2$ RGB-SiPM with a 20 $\mu$m cell. The green line is the ideal response. (b) Non-linearity as a function of the energy.

## 3.3   Setup for the simulation of high-energy gamma-ray response

In this section are presented the two different setups used to characterize SiPMs for spectroscopy. The first is the scintillator setup, employing typical radioactive sources, and used for low energy gamma spectroscopy. The second is the LED setup, based on a LED source, and used to simulate the response of the photodetector to high-energy gamma-rays [105].

Fig. 3.6 (b) shows the scintillator setup used for SiPM-based gamma-ray spectroscopy. It consists of a radioactive source, in this case $^{22}$Na, which emits gamma-rays converted in visible photons by the LYSO crystal, and then detected by SiPM. The SiPM output signal is amplified and digitized. The amplifier is based on fast operational amplifiers in a transimpendace configuration, with a gain of 100 V/A. The amplified signal is digitized by a 10 GS/s oscilloscope (Keysight Infinium S-Series) and 1 GHz analog bandwidth. Using a custom Labview software, each signal is integrated in time to obtain the area, which represents the charge generated in a single SiPM pulse. The histogram of these values is the spectrum of the radioactive source. Fig. 3.7 (a) shows a charge spectrum of $^{22}$Na source measured with a 4x4 mm$^2$ SiPM with 25 $\mu$m-cell coupled to a 4x4x22 mm$^3$ LYSO crystal. In this
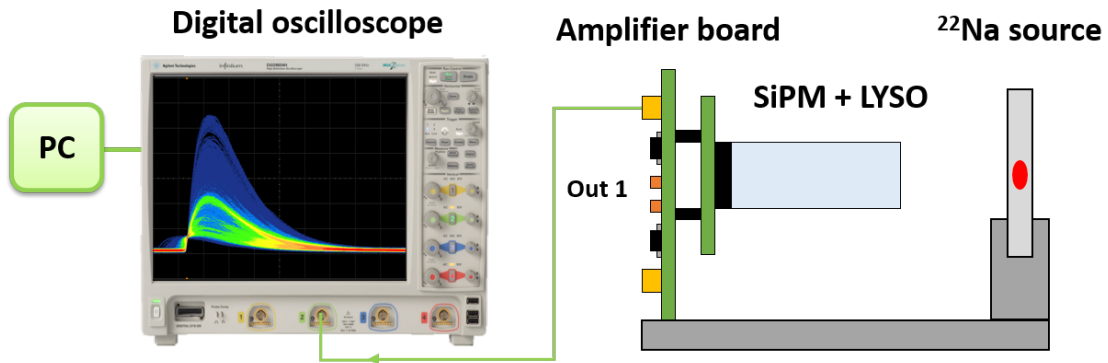
**Figure 3.6:** Measurement setup with radioactive source [105].
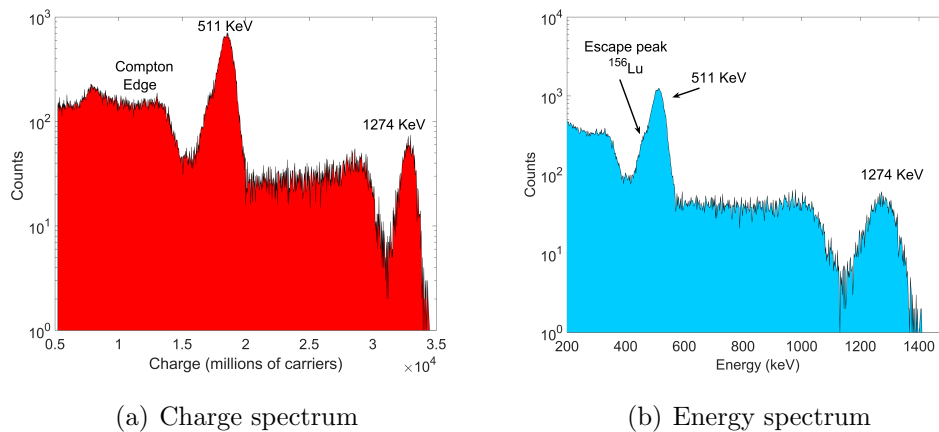


(a) Charge spectrum

(b) Energy spectrum

**Figure 3.7:** Spectrum of $^{22}$Na source measured with a 4x4 mm$^2$ SiPM with 25 $\mu$m-cell coupled to a 4x4x22 mm$^3$ LYSO crystal. Charge spectrum (a) and the energy spectrum (b). The energy spectrum is calibrated and corrected for SiPM non-linearity using Eq. 3.14. In this last spectrum is visible the escape peak caused by $^{176}$Lu which is centred on a energy of (511-54) keV.

charge spectrum are visible the Compton edge, the photo-peak at 511 keV, and the peak at 1274 keV. To convert the charge spectrum into an energy spectrum we use a calibration curve, which is described by the following relation:

$$C(E) = a \cdot (1 - e^{-\frac{E}{b}}), \tag{3.13}$$

where C is the amount of charge generated in the SiPM by impinging photons with an energy of E. The fit parameters of the calibration curve are $a$ and $b$, and are obtained from the two peaks of $^{22}$Na (511 and 1274 keV). Using $a$ and $b$, the charge spectrum is converted and corrected for the non-linearity of the SiPM:

$$E = -b \cdot ln\left(1 - \frac{C}{a}\right). \tag{3.14}$$

Fig. 3.7 (b) shows the energy spectrum obtained using Eq. 3.14. From this energy spectrum, the energy resolutions for each energy peak are calculated with the standard definition:

$$\left(\frac{\Delta E}{E}\right)^2 = \frac{FWHM}{E_0} = \frac{2.35 \cdot \sigma}{E_0}. \tag{3.15}$$

$FWHM = 2.35 \cdot \sigma$ is the Full-Width-Half-Maximun for a Gaussian peak and $E_0$ is the location of the peak centroid for the same Gaussian peak. During the acquisition with the Labview software, the electronic resolution can be calculated form the variance of the baseline acquired before the signal. The non-linearity of a SiPM can produce an important compression of the spectrum, especially at high energy. As example of the effects of saturation, Fig.3.8 shows the prompt gamma-ray spectrum measured in a preliminary measurement run at the proton therapy facility in Trento (Italy), using an RGB-HD 4x4 mm$^2$ SiPM, with 25 $\mu$m cells, coupled to a 4x4x22 mm$^3$ LYSO. If we want to correct the non linearity of such a high-energy spectrum, typical gamma calibration sources are not useful because they have energies of up to 1.5 MeV. In addition, typical SiPMs used for PGI have a very good linearity at this lower energies. Thus, the $a$ and $b$ parameters extrapolated from the fit, i.e. of the 511 and 1275 keV peaks of $^{22}$Na, have a very large measurement errors that prevents to use them at the high energies of the PGI. This fact is well explained by Fig. 3.9. The red line is the fit of the measured SiPM response at high energy, according to Eq. 3.13, using only the two $^{22}$Na peaks (511 and 1274 keV). Instead, the blue line is the fit that is obtained using the SiPM response to LED simulating gamma-ray energies of up to 25 MeV. The difference between the two
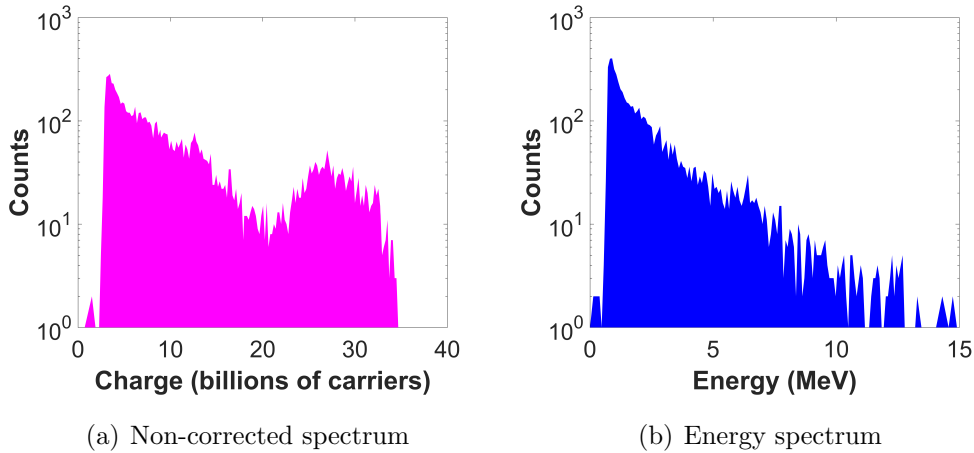
(a) Non-corrected spectrum



(b) Energy spectrum

**Figure 3.8:** Prompt gamma ray spectrum obtained with a proton beam with energy of 225 MeV incident on a water-equivalent phantom before (a) and after calibration with a $^{22}$Na source (b) [105].

lines, shows the importance to have a calibration in high-energy conditions for PGI, or other high-energy gamma-ray applications. Thus, we have developed a novel setup, which is shown in Fig. 3.10. It consists of a pulsed LED, an integrating sphere with two outputs, one for SiPMs and one for a reference diode, which continuously monitors the light intensity emitted by the sphere. The LED (emitting at 420 nm as LYSO scintillators) is driven by a pulse generator (Agilent 33500B Series Waveform Generator), emulating the light emitted by a LYSO scintillator, when it is excited by gamma rays of up to 30 MeV, and assuming that the LYSO emission is proportional to the energy for gamma rays above 1 MeV [106, 107]. Neutral density filters are used to increase the number of measurable configurations, which are limited by the LED operating range (about 2 V). In this way, for each LED operating voltage, we can obtain up to 8 different lighting conditions. Pulse generator parameters (amplitude, duration, rise and fall time constants) are adjusted so that photons emitted by the LED match the intensity and time distribution of the LYSO emission. This setup makes possible the simulation of gamma-ray energies of up to 30 MeV, assuming that the LYSO light yield is constant.

The calibration procedure is the following: the number of photons in each light pulse is calibrated from the measurements at 511 keV, which are obtained with a $^{22}$Na source, and a LYSO crystal coupled to a SiPMs. In such a way, the number of photons emitted from the LED, and measured with the reference diode, is converted
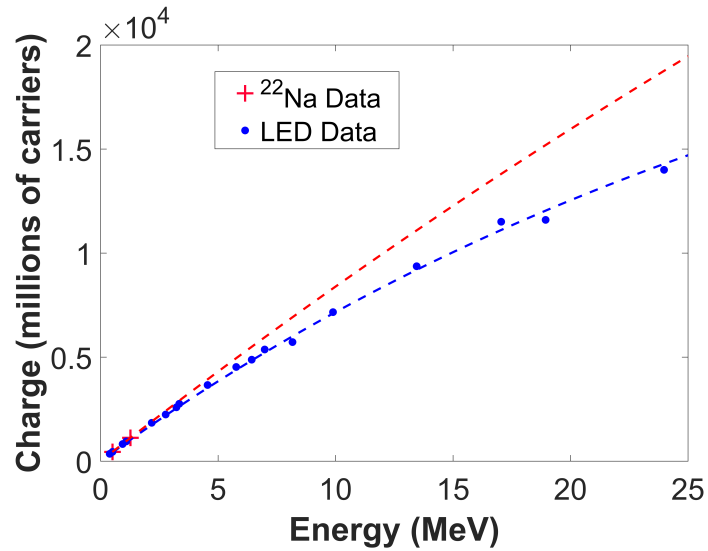
**Figure 3.9:** Fitting results of the Eq. 3.13 for the SiPM response at $^{22}$Na source (red line) and pulsed light source (blue line) [105].
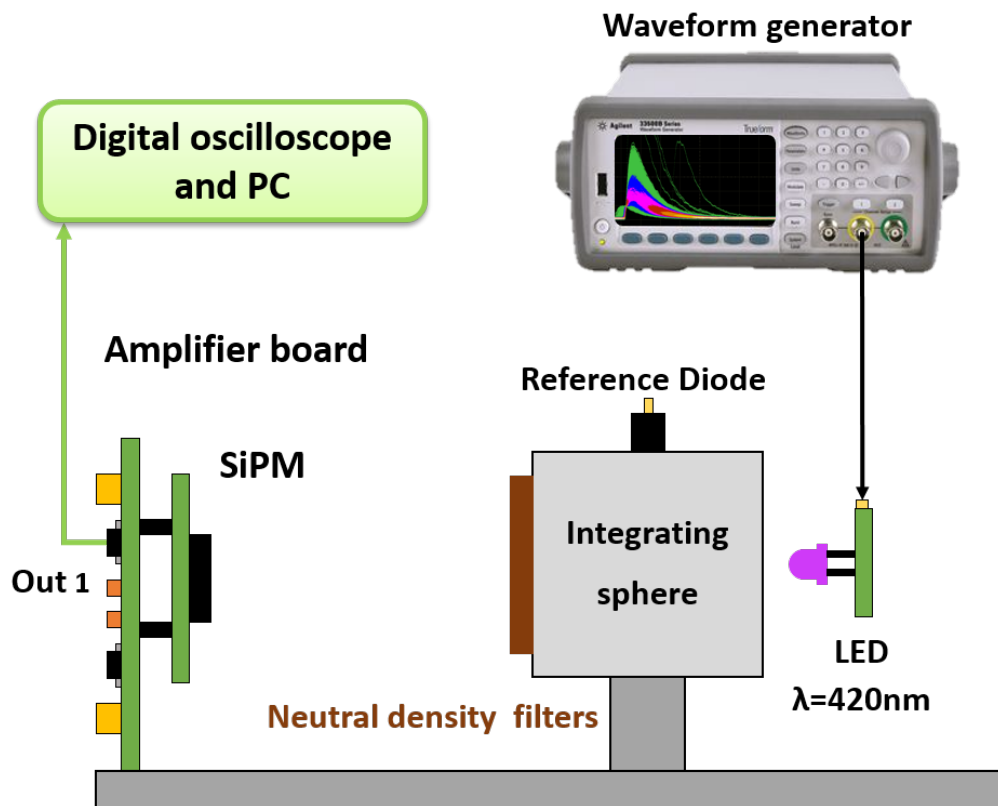


**Figure 3.10:** Measurement setup with LED [105].

an equivalent gamma-rays energy. As in the scintillator setup, the SiPM output signal is amplified and digitized by a oscilloscope. Thus, with a custom Labview software the digitized signal is integrated. The histogram of all signals is the charge spectrum. After the calibration in energy of the LED setup, the charge spectrum is converted in energy and corrected for the SiPM non-linearity. Fig. 3.9 shows an example of the calibration curve obtained with the LED setup (blue line). As a first approximation, such a curve can be used to calibrate the measurements of real experiments of prompt gamma imaging and high-energy spectroscopy.

To use correctly the LED setup preliminary calibrations and characterizations were required. These preliminary operations are described in Sec. 3.3.2. The measurements with both setups were performed by placing the SiPM, the SiPM-crystal, amplifier, the integrating sphere, and the LED inside a dark chamber at the controlled temperature of 20 $^o$C.

## 3.3.1   Scintillator versus LED characterization

Using the two different setups, described in Sec. 3.3, two different measurements of the energy resolution are obtained. The resolution measured with the scintillator setup (in Fig. 3.6) is described by Eq. 3.7:

$$\left(\frac{\Delta E}{E}\right)^2 = (R_i)^2 + (R_{stat})^2 + (R_{el})^2 \,, \tag{3.7}$$

which includes the crystal intrinsic resolution, statistical resolution, and electronic resolution. Instead, the energy resolution with the LED setup (in Fig. 3.10) includes only the statistical, and electronic components. It can be expressed as:

$$\left(\frac{\Delta E}{E}\right)^2_{LED} = (R_{stat})^2 + (R_{el})^2 \,. \tag{3.16}$$

The LED setup, because of the calibration of the reference diode, provides also the number of photons, $N_{ph}$, impinging on the SiPM active area. With this number, the energy resolution due to the pure Poisson statistics of the photons can be calculated as:

$$(R_{pois})^2 = \frac{1}{N_{ph} \cdot PDE}. \tag{3.17}$$

$R_{stat}$, described by the second term of the Eq. 3.7, is $R_{pois}$ divided by ENF. They are linked by the following relation:

$$(R_{stat})^2 = (R_{pois})^2 \cdot ENF. \tag{3.18}$$

This last equation allows to obtain, from the measurements with the LED setup, the ENF due to the SiPM correlated noise and to the saturation of SiPM cells. Moreover, combining the results of the LED and the crystal setup, the intrinsic contribution of the crystal, $R_i$, can be estimated from the difference between Eq. 3.7 and Eq. 3.16. Thus, the intrinsic resolution of the used LYSO scintillator is:

$$(R_i)^2 = \left(\frac{\Delta E}{E}\right)^2 - \left(\frac{\Delta E}{E}\right)^2_{LED}.$$

(3.19)

### 3.3.2   Calibration of LED setup

To obtain from the LED setup information on the number of impinging photons on SiPMs, and to relate this number of photons to the energy, four steps are necessary:

- Calibration of the reference diode for all neutral density filters employed.

- Study of the 2D uniformity of the light.

- Simulation of the LYSO(Ce) emission with the 420 nm LED.

- Calibration of the setup in energy for all SiPMs employed.

These steps are described in detail in the next part of the paragraph.

**Calibration of the reference diode**
The calibration of the reference diode is performed using the procedure described in [80]. The calibration relates the current read by the reference diode, see Fig. 3.10, to the number of photons, per unit time and area, which reaches the SiPM location. For the calibration, a calibrated photodiode is placed in the position in which SiPMs are located for the measurements. The number of photons, $N_{ph}$, impinging on SiPM in a certain position, can be expressed as:

$$N_{ph} = \frac{I_L - I_D}{A \cdot h \cdot \nu \cdot \eta},$$

(3.20)

where $I_L$ and $I_D$ are the currents read by the calibrated photodiode in light and dark condition, A is the active area of the calibrated photodiode, $\eta$ its responsivity, h is the Planck constant, and $\nu$ the frequency of the light. This calibration must be repeated for each LED with different wavelength, and for each neutral density filter, which are used in the subsequent measurements. In this thesis, the LYSO crystal is simulated, and thus the reference diode was calibrated for a LED with wavelength of

420 nm, and for eight different combination of ND filters. As explained previously, filters are necessary to increase the number of measurable configurations, which are limited by the LED operating range. Calibration coefficients obtained for the different configurations are listed in Table 3.2.

**Table 3.2:** Calibration coefficients for the 420 nm LED and for different neutral density filter configurations. The distance between the SiPM position and the integrating sphere is ∼560 mm.

| Filter Optical Density OD | Calibration coefficient ph/(s mm$^2$ A) | Error ph/(s mm$^2$ A) |
|:---:|:---:|:---:|
| **No filter** | $3.503 \times 10^{+16}$ | $1.401 \times 10^{+14}$ |
| **0.5** | $1.185 \times 10^{+16}$ | $4.739 \times 10^{+13}$ |
| **1** | $3.971 \times 10^{+15}$ | $1.787 \times 10^{+13}$ |
| **1.5** | $1.487 \times 10^{+15}$ | $6.690 \times 10^{+12}$ |
| **2** | $2.472 \times 10^{+14}$ | $1.236 \times 10^{+12}$ |
| **2.5** | $1.090 \times 10^{+14}$ | $5.452 \times 10^{+11}$ |
| **3** | $4.047 \times 10^{+13}$ | $2.023 \times 10^{+11}$ |
| **3.5** | $1.440 \times 10^{+13}$ | $7.198 \times 10^{+10}$ |

**Uniformity of the light**

The uniformity of the incoming light on the SiPM location for the PDE setup, described in Sec. 2.2.2, is presented in [80]. In the PDE setup, described in Sec. 2.2.2, the maximum variation of the light on a 2x2 cm$^2$ area around the SiPM location was ∼3%. The PDE setup has an identical integrating sphere of the LED setup. Thus, we have done the reasonable assumption to obtain similar results for a characterization of the LED setup. However, differently from the PDE setup, the misalignment introduced by LED setup is negligible because all part of the LED setup are fixed, and packages of the different SiPM under test are the same.

**Simulation of the LYSO(Ce) emission**

The saturation condition of a SiPM depends on its number of cells. Furthermore, this saturation depends on the recharge time constant of a SiPM, and its value in relation with the decay time constant of the scintillator crystal. For example, if the recharge time of the SiPM is much shorter than the scintillator emission time constant, a single cell of the SiPM can be triggered by the scintillation light more than once and, thus, the non linearity is significantly reduced [104]. Thus, it is

essential to reproduce with the LED setup the intensity and the time distribution of the light emitted by the LYSO crystal. This is accomplished by using a pulse generator and changing its parameters, such as amplitude, duration, rise and fall time constants. In detail, the voltage waveform applied to the LED is tuned so that its light emission has the same time distribution and amplitude as the light emitted by the LYSO scintillator in response to gamma rays of 511 keV. Gamma rays of different energy are simulated changing the bias applied to the LED, i.e. amplitude. Fig. 3.11 shows the time profile of the LED light emission, which was measured with the Time Correlated Single Photon Counting (TCSPC) technique. The light emitted by the LED is very similar to LYSO signal, with a decay time constant of $\tau \sim 40$ ns.
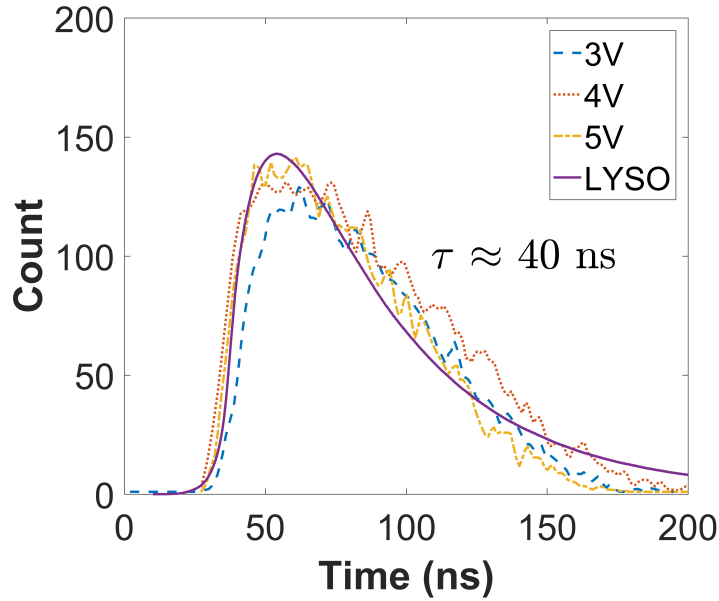


**Figure 3.11:** Time distribution of the light emitted by the 420 nm LED at different LED bias compared to the normalized LYSO emission (continuous line).

### Calibration in energy

Because of the previous calibration of the reference diode, the number of photons impinging on the SiPM, $N_{ph}$, is known. To relate the $N_{ph}$ to the energy we use the measurements at 511 keV, performed with a $^{22}$Na source and a LYSO crystal coupled to a SiPM. In detail, we have reproduced with the LED, the charge generated in the 511 keV photopeak of the spectrum measured with the SiPM coupled to the

LYSO crystal, thus:

$$C_0(^{22}Na) = C_0(LED), \tag{3.21}$$

where $C_0$ are the centroids of the two Gaussian peaks of the charge spectrum, which are generated with the two different setups. Fig. 3.12 shows an example of this calibration in energy. In this situation, the number of photons impinging on the
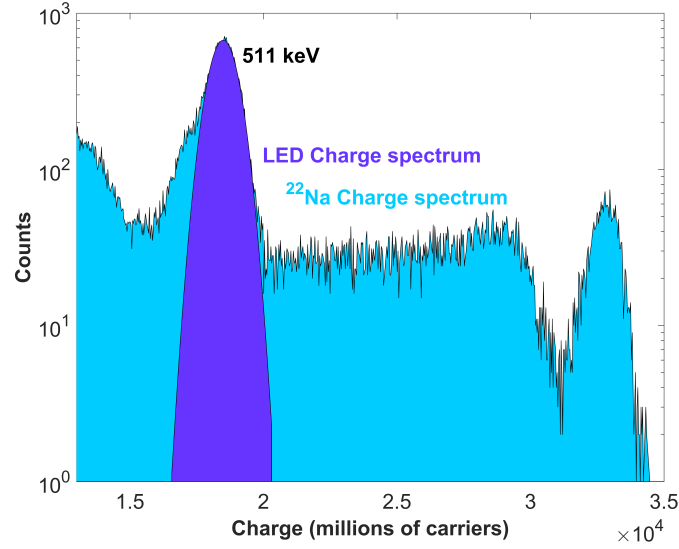


**Figure 3.12:** Example of energy calibration of the LED setup. A 511 keV peak of charge spectrum of $^{22}$Na is used to calibrate LED charge spectrum.

SiPM is $N_{ph}(511)$. Assuming that the LYSO emission is proportional to the energy for gamma rays above 1 MeV [106, 107], it can be written:

$$N_{ph}(511) : 511keV = N_{ph}(E) : E. \tag{3.22}$$

Thus, gamma-rays of different energies E can be generated changing the $N_{ph}$ impinging on the SiPM:

$$E(keV) = \frac{N_{ph}(E) \cdot 511}{N_{ph}(511)}. \tag{3.23}$$

This is accomplished by measuring the current of the reference diode and by changing the amplitude of the voltage waveform driving the LED until the diode current corresponds to the desired number of photons multiplied by the pulse repetition rate. Fig. 3.13 shows an example of the different energies as a function of the $N_{ph}$ impinging on the SiPM. Different energies are obtained using four different neutral density filters. Errors on the the number of photons impinging on the SiPM are 1%,

instead on the simulated energy are between 2.5% and 3% because of the presence of uncertainties when, with the LED, it is reproduced the charge generated in the 511 keV photopeak of the spectrum, see Eq. 3.21. Errors are omitted for clarity from the graph. The number of photons $N_{ph}(511)$, which is found in this calibration, is
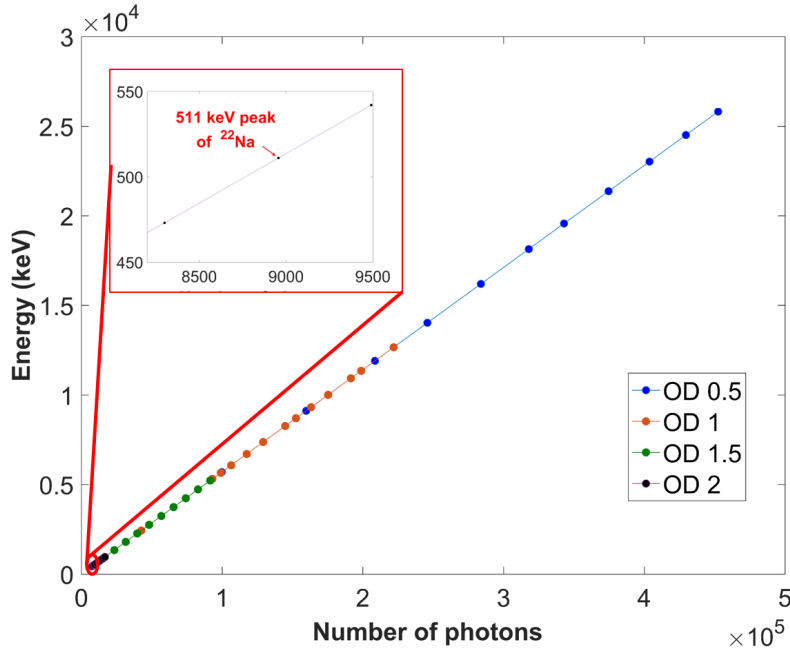


**Figure 3.13:** Example of simulated gamma ray energies as a function of the $N_{ph}$. The data are obtained using four different neutral density filters with OD between 0.5 and 2.

not equal to the light yield of the LYSO crystal at the same energy. This is because the calibration is based on the SiPM response at the LYSO output light, and only a fraction of the photons produced in the LYSO (and other scintillators) arriving at the SiPM surface. This effect is mainly caused by internal reflections of the photons inside the LYSO, and by the coupling interface between the LYSO and the SiPM. An estimation of this effect is provided by light collection coefficient, $\alpha$, which is defined as the ratio between the light output of the scintillation element, $N_{ph}$, and the absolute light yield Y [108]:

$$\alpha = \frac{N_{ph}}{Y}. \tag{3.24}$$

The light collection in scintillator depends on a large number of parameters, such as form and dimension of the crystal, crystal surface treatments, reflective materials, and optical coupling to photosensors [108]. This problem have been studied for

many years [109, 110, 111, 112]. A complete dissertation on this topic falls outside of the aims of this thesis. However, because of the calibration of the LED setup, it can be estimated a relative light collection coefficient of the LYSO crystal for this case.

# Chapter 4

# Characterization of HD and UHD SiPMs

In this chapter we present and discuss about the results of the characterization of High-Density (HD) and Ultra-High-Density RGB (UHD) SiPMs. The presented results are obtained testing some devices and are representative of the technology properties. The first part of the characterization regards the optical and electrical SiPM proprieties, such as photon detection efficiency, gain, dark count rate, and correlated noise. This characterization is presented in Sec. 4.1 and Sec. 4.2. These measurements were performed using methods described in Chapter 2. The tested RGB-HD and RGB-UHD SiPMs are presented in Table 4.1.

Table 4.1: Characteristics of tested SiPMs

| Technology | Cell pitch ($\mu$m) | Cell density (cells/mm$^2$) | Fill Factor (%) | SiPM Active Area (mm$^2$) |
|:---:|:---:|:---:|:---:|:---:|
| RGB-UHD | **7.5** | ∼20500 | 57 | 3x3 |
| RGB-UHD | **10** | ∼11550 | 68 | 3x3 |
| RGB-UHD | **12.5** | ∼7400 | 75 | 3x3 |
| RGB-HD | **15** | ∼4500 | 62 | 4x4 |
| RGB-HD | **20** | ∼2500 | 67 | 4x4 |
| RGB-HD | **25** | ∼1600 | 72 | 4x4 |
| RGB-HD | **30** | ∼1100 | 78 | 4x4 |

The second part of the characterization focuses on spectroscopy performance of SiPMs coupled to a scintillator crystals. These measurements were performed as explained in Chapter 3. Tested SiPMs and LYSO scintillator crystals (Hilger Crystals Ltd [113]) are reported in Table 4.2. We did not test SiPMs with cell of

**Table 4.2:** Characteristics of tested SiPMs and scintillator crystals.

| Technology | Cell pitch ($\mu$m) | Active Area (mm$^2$) | Cell number (cells) | LYSO size (mm$^3$) |
|---|---|---|---|---|
| RGB-UHD | **10** | 3x3 | 103950 | 3x3x15 |
| RGB-UHD | **12.5** | 3x3 | 66600 | 3x3x15 |
| RGB-HD | **15** | 4x4 | 71111 | 4x4x22 |
| RGB-HD | **20** | 4x4 | 39600 | 4x4x22 |
| RGB-HD | **25** | 4x4 | 25600 | 4x4x22 |

30 $\mu$m because of their low cell-density, and SiPMs with cell of 7.5 $\mu$m because of a not-proper quenching of these cells due to a small value of the quenching resistors, caused by the wrong setting of a fabrication parameter [105].

## 4.1    Photon detection efficiency

In this section we present the Photon Detection Efficiency (PDE) results. PDE was evaluated following the method described in Sec. 2.2.2. Measurements were performed at room temperature.

Fig. 4.1 shows the PDE as a function of wavelength for a 25 $\mu$m-size RGB-HD SiPM. The PDE is peaked around 550 nm, as expected for a n-on-p technology [74], and increases with the over-voltage because of the increase of the trigger probability. On over-voltage range between 6 and 8 V, the maximum of the PDE is between 34% and 38% respectively. At 420 nm, the region of interest in applications which use LYSO crystals, is between 23% and 27%.
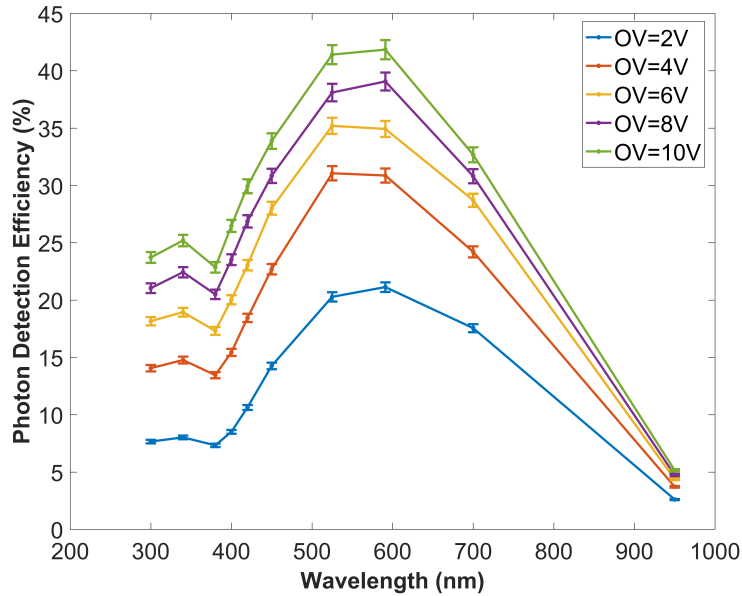


**Figure 4.1:**    PDE as a function of the wavelength for RGB-HD SiPM (25 $\mu$m) at different over-voltages. Relative errors are between 1.5% and 3%.

Fig. 4.2 shows the PDE as a function of over-voltage at a wavelength of 420 nm for the different RGB-HD and RGB-UHD SiPMs presented in Table 4.1. At the same over-voltage, the PDE increases with cell size because of the higher Fill Factor (FF) of the larger cells. It is also clearly visible that the PDE raises as a function of the over-voltage. Relative errors on the PDE measure are between 1.5% and 3%. It is important to note that the measured PDE is not proportional to the nominal FF defined by the layout, as reported in Table 4.1, but to an effective FF. The effective
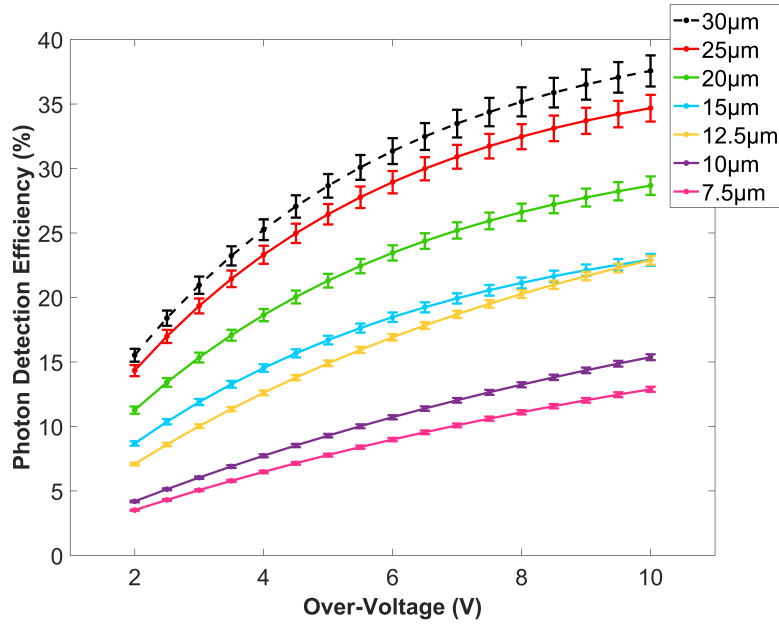
**Figure 4.2:** PDE as a function of over-voltage for different cell sizes of RGB-HD and RGB-UHD SiPMs, at a wavelength of 420 nm. Relative errors are between 1.5% and 3%.

FF is smaller than the nominal FF because on the 'border effect': the electric field region is smaller than the nominal one, and the charge carriers generated at the edge do not drift towards the high-field region [76]. We are working on a newest development of the UHD technology to reduce the 'border effect' and improve the PDE without affecting the correlated noise [76].

## 4.2    Gain and noise

In this section we show the characterization of the gain and of the noise, which are performed as described in Sec. 2.2.3. Measurements were performed in a thermostatic chamber at a fixed temperature of 20 $^{o}$C. Errors on various measured quantities are calculated using the error propagation method, but they are omitted for clarity in the plots.

Fig. 4.3 shows the gain as a function of over-voltage for different cell sizes. The gain is the product of the cell capacitance times the over-voltage. So, it is higher for the bigger cells, which have higher capacitance because of their geometry, and it increases with the over-voltage. The gain has typically two slopes given by the depletion or non-depletion of the epitaxial layer. In Fig. 4.3 these trends are visible

only in the larger cells. The first part of the gain curve has a non-linear behaviour, which is due to a decreasing capacitance caused by a incomplete depletion of the epitaxial layer. Then, at ~5-6 V of over-voltage, the gain starts to increase linearly since the epitaxial layer is fully-depleted. The gain is in the order of $10^6$ for cell sizes larger than 15 $\mu$m (HD SiPMs), and in the order of $10^5$ for smallest cells (UHD SiPMs).
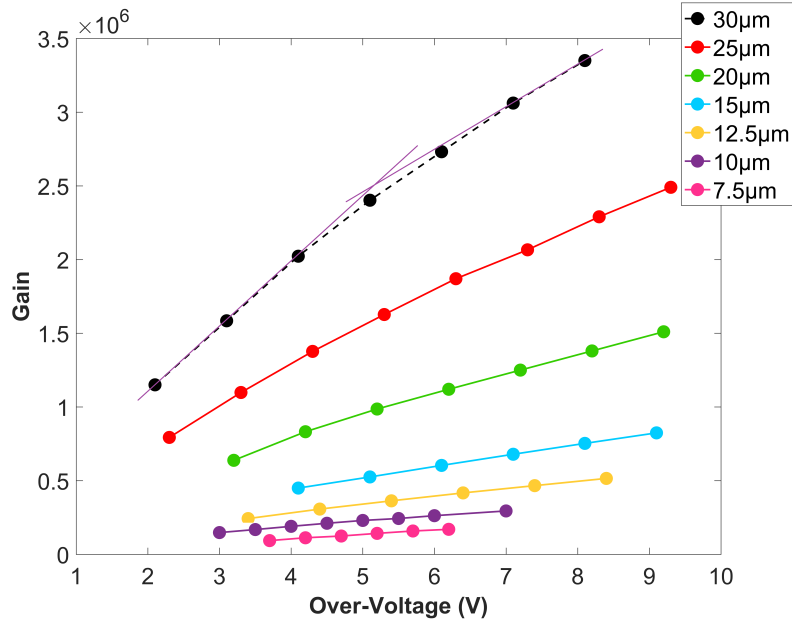


**Figure 4.3:** Gain as a function of the over-voltage for different cell sizes of the HD and UHD SiPM technologies. Gain increases with the over-voltage and the cell size. Relative errors are between 2% and 5%.

Regarding to the noise, both primary and correlated noise were measured. Fig. 4.4 shows the primary DCR as a function of the over-voltage for different cell sizes. Primary DCR is caused by thermal generation and it is strongly related to wafer quality: in both presented technologies (HD and UHD) the starting wafers come from the same manufacturer and are manufactured in FBK with similar processes, thus we can expect comparable primary DCR per unit of active area. The DCR increases with the over-voltage because of the increasing triggering probability. In addition, the thermal generation is partially field enhanced, thus DCR constantly increases with the over-voltage and with the effective FF. These two effects are particularly important in small cells. The DCRs of HD and UHD technologies are between ~100 and ~600 KHz/mm². Fig. 4.5 shows the primary DCR as a function of the over-
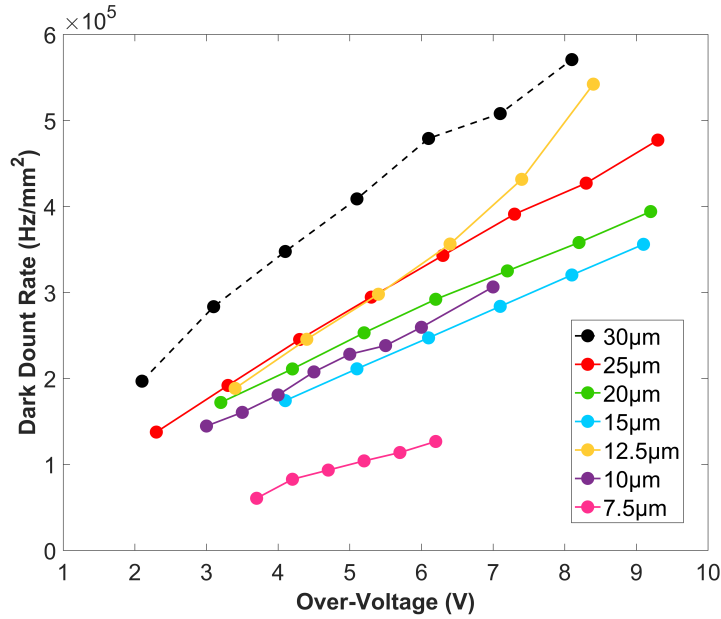
**Figure 4.4:** Primary DCR as a function of the over-voltage for different cell sizes of HD and UHD technologies. Relative errors are between 2% and 5%.

voltage for different cell sizes of the HD technology (a), and the UHD technology (b). For each technology we can see a clear trend of the DCR as a function of the cell size.

Regarding to the correlated noise, the probabilities of cross-talk and after-pulsing were measured with the procedure reported in Sec. 2.2.3. Fig. 4.6 shows direct optical CT as a function of the over-voltage for different cell sizes. Direct CT increases with over-voltage because of the higher PDE and gain. Cell sizes from 7.5 $\mu$m to 15 $\mu$m show a direct CT lower than 13% along their entire operative range. A low correlated noise reduces the saturation of SiPMs in high-energy gamma spectroscopy, improving global performance of detectors.

After-Pulsing (AP) and Delayed Optical CT (DeCT) are both estimated by the counts in excess of the DCR Poissonian fit in the inter-time histogram, as explained in Sec. 2.2.3. They are sometimes difficult to separate, thus Fig. 4.7 shows the sum of these two probabilities as a function of the over-voltage. Similarly to the direct CT, AP and delayed CT probabilities increase with the over-voltage and with the cell size. These trends are clearly visible for the HD technology (cell size from 15 to 30 $\mu$m). In the UHD technology (cell size from 10 to 12.5 $\mu$m) instead, there is a divergence of the AP probability because the quenching resistor is too

(a) DCR RGB-HD                                  (b) DCR RGB-UHD
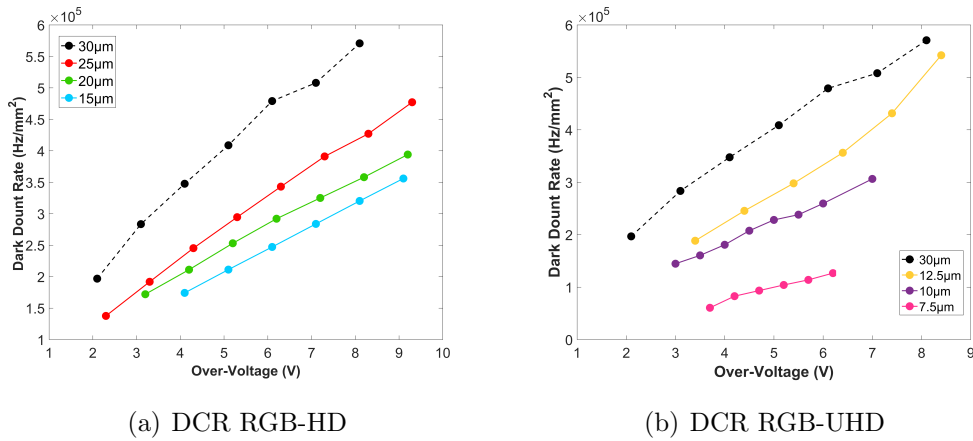
**Figure 4.5:** Primary DCR as a function of the over-voltage for different cell sizes of the HD technology (a), and the UHD technology (b) with the cell of 30 $\mu$m of the HD SiPMs as reference. Relative errors are between 2% and 5%.
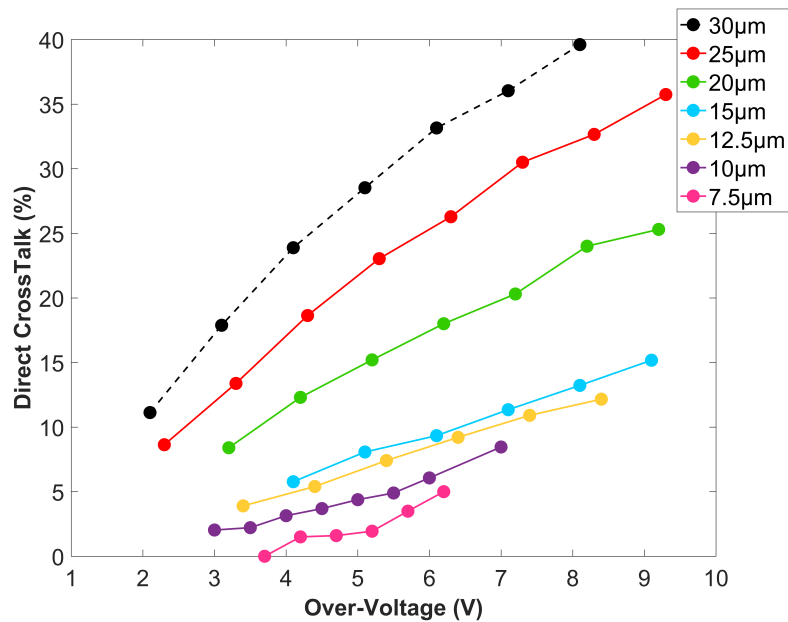


**Figure 4.6:** Direct optical CT probability as a function of the over-voltage for different cell sizes. Relative errors are between 2% and 3%.

low. This makes the avalanche in the microcell not properly quenched above a certain over-voltage, i.e. bad quenching, and it is not possible to measure the AP probability correctly. In UHD SiPMs the quenching resistor values were chosen relatively low (with respect to the HD SiPMs) in order to reduce the recharge time of the cells and to have an ever higher dynamic range. For the 7.5 $\mu$m-cell it was not possible estimate properly the probabilities of AP and delayed CT because too small quenching resistors, which cause a bad quenching of cells. As for the direct CT probability, cell sizes smaller than 15 $\mu$m provide very good results, with a sum of the AP and delayed CT probabilities lower than 5% (excluding over-voltage greater than 6 V for the cell of 10 $\mu$m and 12.5 $\mu$m). Due to the very small values of AP and DeCT events, relative errors on the obtained values are between 6% and 9%.

Overall, these measured noise values are similar to the current state-of-the-art [48]. The primary DCR is also better than previous FBK SiPMs technologies [114].
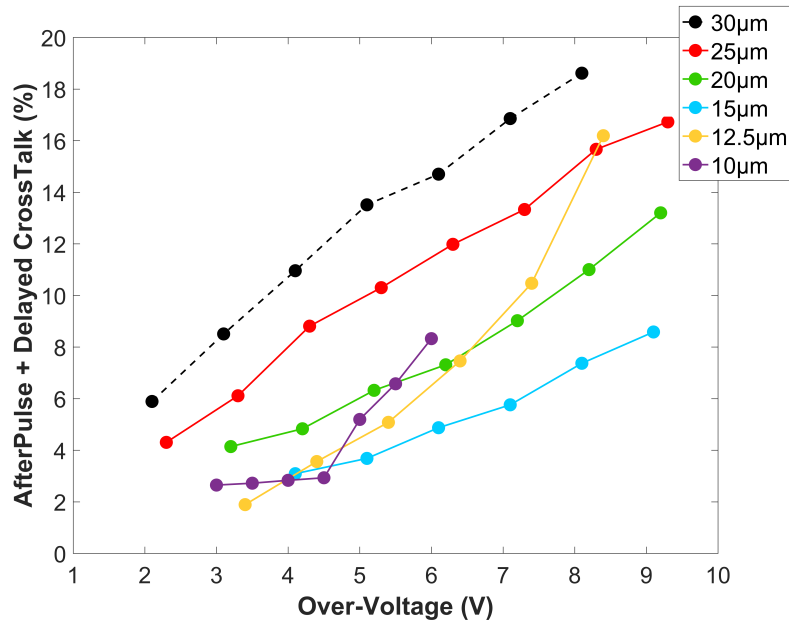


**Figure 4.7:** Sum of after-pulse and delayed optical CT probabilities as a function of the over-voltage for different cell sizes. Relative errors are between 6% and 9%.

## 4.3   Energy resolution at low energies

In this section we present the results of the measurement of the energy resolution of HD and UHD SiPMs coupled to scintillator crystals, performed with a $^{22}Na$ and the scintillator setup, as explained in Sec. 3.2.1. Measurements were performed in a thermostatic chamber at a fixed temperature of 20 $^o$C.

Fig. 4.8 shows energy resolutions as a function of the over-voltage for different cell sizes at 511 keV. The energy resolution improves with cell size and the over-
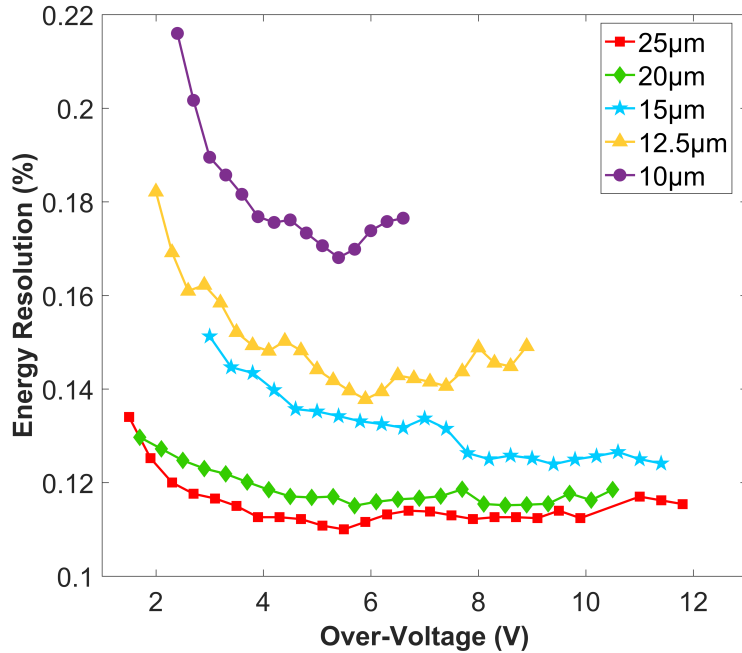


**Figure 4.8:**  Energy resolution as a function of the over-voltage for different cell sizes at 511 keV. Relative errors are between 3% and 6%

voltage due to the higher PDE. For UHD SiPMs, i.e. 10 $\mu$m and 12.5 $\mu$m, the energy resolution deteriorates at over-voltage higher than ∼5 V because of the SiPM bad quenching. For the HD technology at medium and high over-voltages the energy resolution is constant because the improvement of the PDE is balanced by the increase of the ENF due to the correlated noise.

## 4.4   Energy resolution at high energies

In this section we present energy resolution results performed with LED setup, described in Sec. 3.3. These values do not include the LYSO intrinsic term. Measurements were performed in a thermostatic chamber at a fixed temperature of 20 ºC. Relative errors on the energy resolution are between 3% and 6%. They are omitted for clarity in the graphs.

Fig. 4.9 shows the energy resolution, measured with the LED setup simulating the LYSO emission in response of 5 MeV photons, as a function of the over-voltage for different cell sizes. As in previous section, between low and medium



**Figure 4.9:** Energy resolution as a function of the over-voltage for different cell sizes at 5 MeV [105].

over-voltages, the energy resolution improves with increasing cell size because the PDE gets larger while the effect of the ENF is negligible. Depending on the over-voltage, we can define three different regions as a function of the over-voltage: at low over-voltage, energy resolution improves because of the increase of the PDE. At medium over-voltage, energy resolution is constant because the improvement of the PDE is balanced by the increase of the ENF due to the correlated noise and the non-linearity. At high over-voltage, the energy resolution deteriorates because the growth of the ENF is no longer compensated by the PDE, as a consequence of the saturation of the triggering probability.

Fig. 4.10 shows the energy resolution, measured with the LED setup, as a function of the energy for different cell sizes, at fixed over-voltage of 6 V. At low energies,



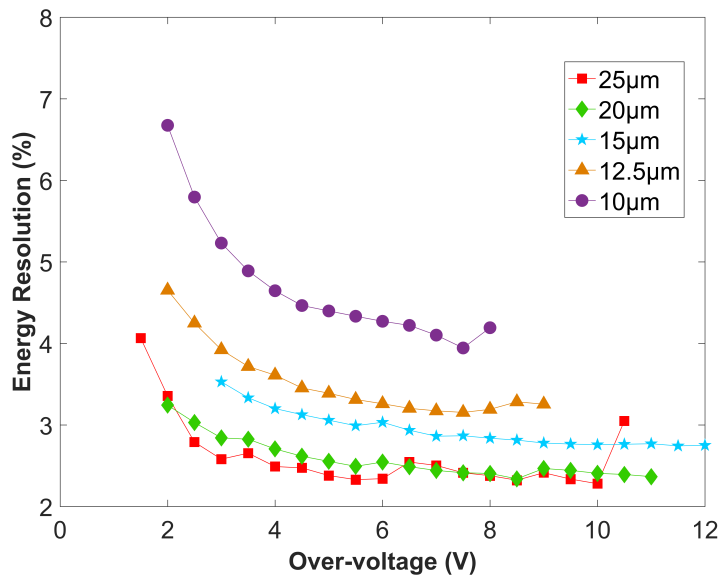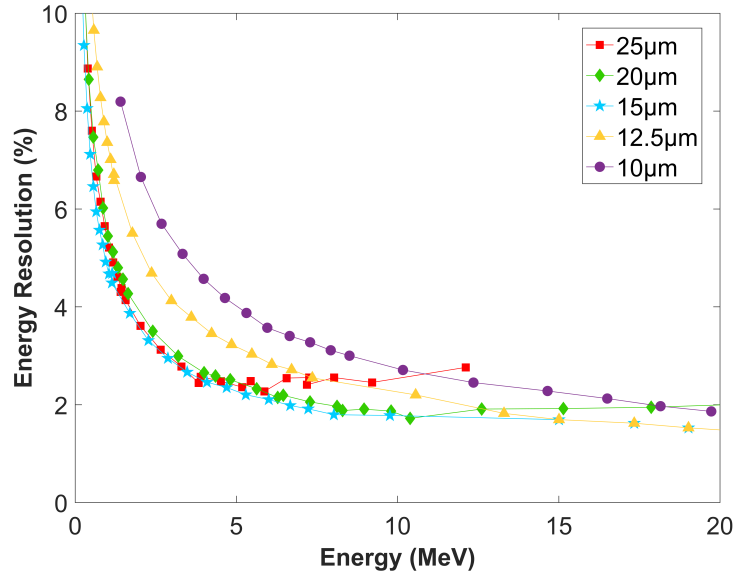**Figure 4.10:** Energy resolution as a function of the energy for the different cell sizes at 6 V over-voltage [105].

the energy resolution improves with increasing energy because of the improvement of the statistical term and the reduction of the electronic one. It can be also noted that the improvement is faster for the larger cell sizes, which feature the highest PDE. However, at very high energies, the 20 $\mu$m and 25 $\mu$m cells show a deterioration of the energy resolution because of the non-linearity. On the contrary, there is no deterioration at high energies for the smallest cells, for which the energy resolution keeps improving up to 20 MeV.

The dependence of the energy resolution on the over-voltage is shown in Fig. 4.11 as a function of the energy for 25 $\mu$m-cell. The bottom x-axis shows the energy, while the top x-axis shows the number of photons impinging on the SiPM surface at each energy. As already observed in Fig. 4.9, energy resolution improves with over-voltage up to approximately 4 V. Above that value it is almost constant. The improvement of the energy resolution with energy is similar to the one already shown in Fig. 4.10. If we consider the highest over-voltages of 8 and 10 V, however, the high number of photons, together with the high PDE and correlated noise of the 25 $\mu$m-cell, cause strong saturation of the detector, which causes a deterioration of the energy
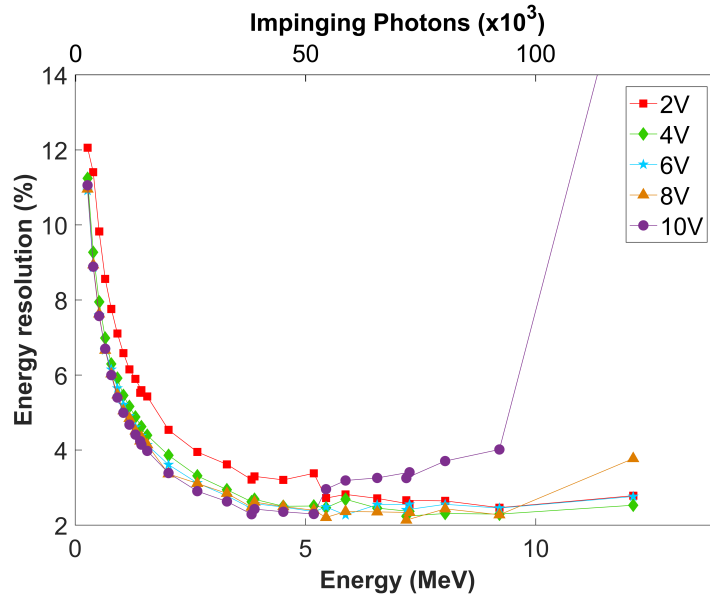
**Figure 4.11:**   Energy resolution as a function of the energy (bottom x-axis) and impinging photons (top x-axis) for 25 $\mu$m cell at different over-voltage [105].

resolution. This deterioration cannot be explained by the increase of the ENF due to correlated noise alone, constant in each different data series with the over-voltage, but should be attributed to the ENF caused by the saturation.

Fig. 4.12 shows the energy resolution at 5 MeV, from the LED setup, as a function of the PDE for different cell sizes. It can be noted that all the points are aligned on the same curve, which is not dependent on the cell size. This is expected because, without correlated noise or saturation, the energy resolution is dominated by the statistical contribution only. The curves start separating when the ENF, caused by correlated noise and saturation, becomes larger than one. For example, the smallest cells (UHD technology) start deviating from the pure Poissonian curve at low over-voltage of 5 V and 5.5 V (the seventh point of the series, respectively). This behaviour cannot be attributed to the non-linearity or to the correlated noise. Both are very low at 6 V of over-voltage, as seen in Fig. 4.17, and in Sec. 4.2. The phenomenon can be attributed to the bad quenching. On the other hand, the energy resolution of the 25 $\mu$m cell is deteriorated at the higher PDE points because of a simultaneous increase of the correlated noise and saturation.
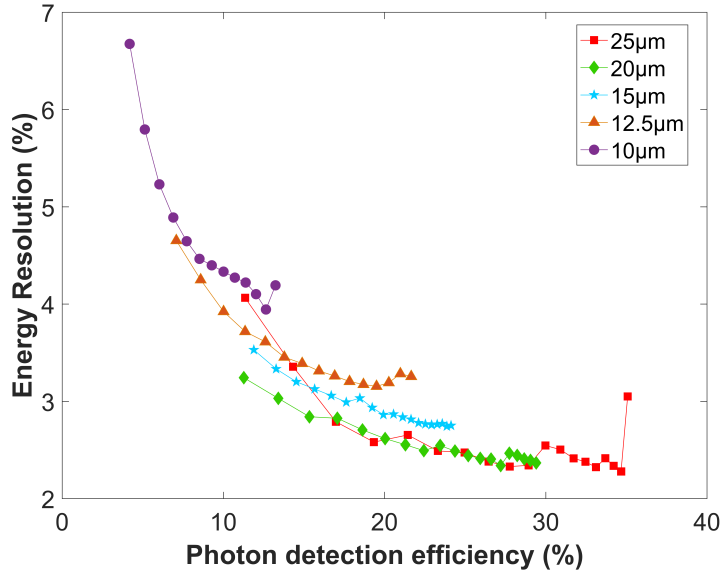
**Figure 4.12:** Energy resolution as a function of the PDE for different cell sizes at 5 MeV [105].

## 4.5 Intrinsic energy resolution of the scintillator

As mentioned in Sec. 3.3.1, the combination of the LED and crystal setups allows the estimation of the intrinsic contribution $R_i$ of LYSO scintillators used in these measurements, based on Eq. 3.19.

For this calculation, we considered the two peaks corresponding to the 511 keV and 1254 keV photons emitted by a $^{22}$Na source. Fig. 4.13 and Fig. 4.14 show the different components of the energy resolution as a function of the over-voltage for the 25 $\mu$m 4x4 mm$^2$ SiPM coupled to 4x4x22 mm$^3$ LYSO crystal. It can be noted that the electronic noise component is relevant, but not dominant in the left region of the plot and decreases quickly with increasing over-voltage. The sum of the statistical and electronic components provides the resolution due to the SiPM, defined in Eq. 3.16, which improves with the over-voltage because of the reduced electronic noise and the increased PDE, which improves the poisson statistics. By subtracting the SiPM energy resolution ($R_{stat} + R_{el}$, red line) from the SiPM+LYSO energy resolution (defined in Eq. 3.7 as $R_{stat} + R_{el} + R_i(LYSO)$, black line) we obtain an estimate of the LYSO intrinsic energy resolution at 511 keV $R_i(511)$, see Fig. 4.13. Excluding the lower over-voltages, where there is a larger experimental uncertainty, the calculated value of $R_i(511)$ does not depend on the SiPM bias, as expected. We can also notice that the energy resolution is limited by the crystal starting from 6 V:

**Figure 4.13:**   Different components of the energy resolution at 511 keV, as a function of the over-voltage, for 25 $\mu$m cell SiPM coupled to LYSO crystal [105].



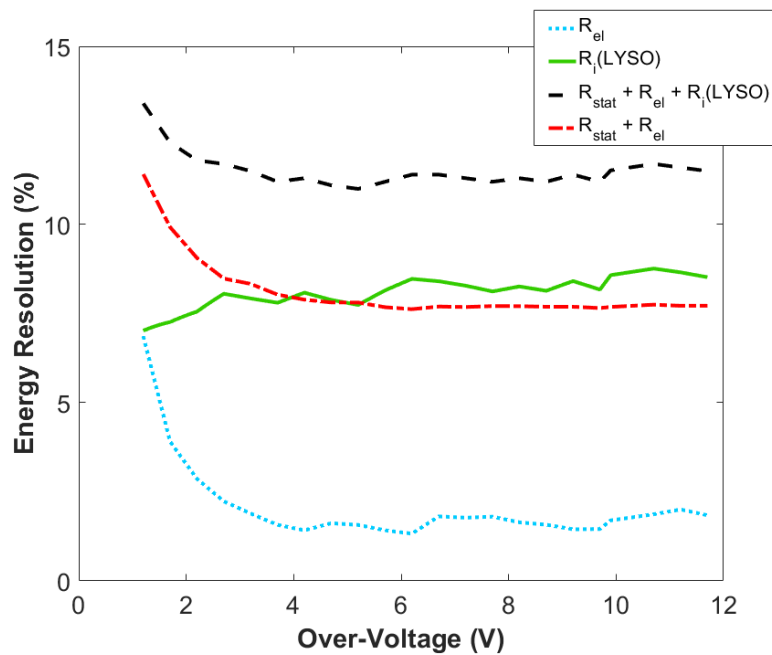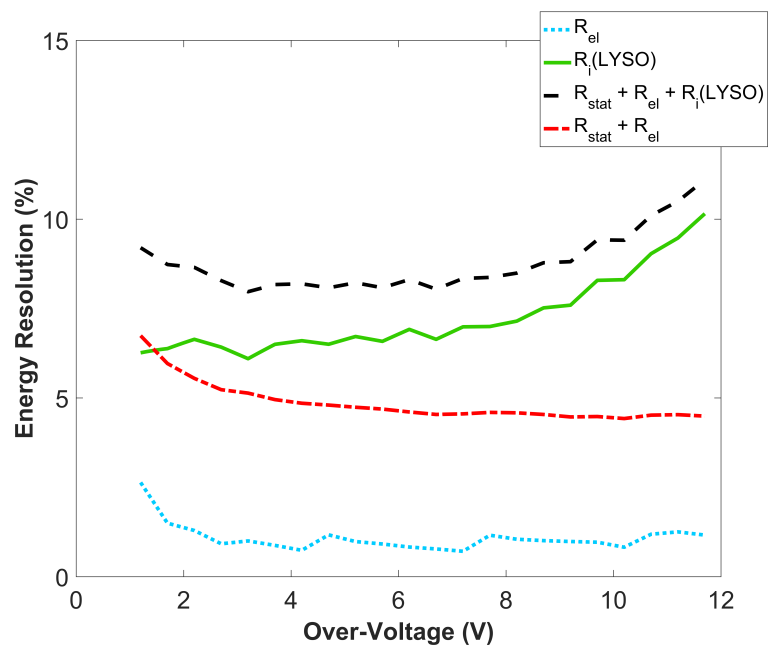**Figure 4.14:**   Different components of the energy resolution at 1274 keV, as a function of the over-voltage, for 25 $\mu$m cell SiPM coupled to LYSO crystal [105].

above this value, $R_i(511)$ covers the improvement of detector performance. Fig. 4.14, shows the same measurement carried out at the higher energy of 1274 keV. In this case, the energy resolution measured with the crystal gets worse at high over-voltage, instead of saturating as at 511 keV. The increase is not present in the energy resolution measured without the scintillator. As a consequence, the calculated $R_i(1274)$ is not constant with the over-voltage. The reason for this behaviour can be attributed to the increase of the correlated noise, which amplifies the signal generated by the 1274 keV photons and causes significant SiPM saturation. The corresponding ENF, see Sec. 3.3.1, degrades the energy resolution. The signal amplification caused by the correlated noise can be observed easily from the reverse IV curve of the device, measured in dark and with or without the LYSO scintillator, as shown in Fig. 4.15. It can be observed that the current measured with the crystal placed on top of the
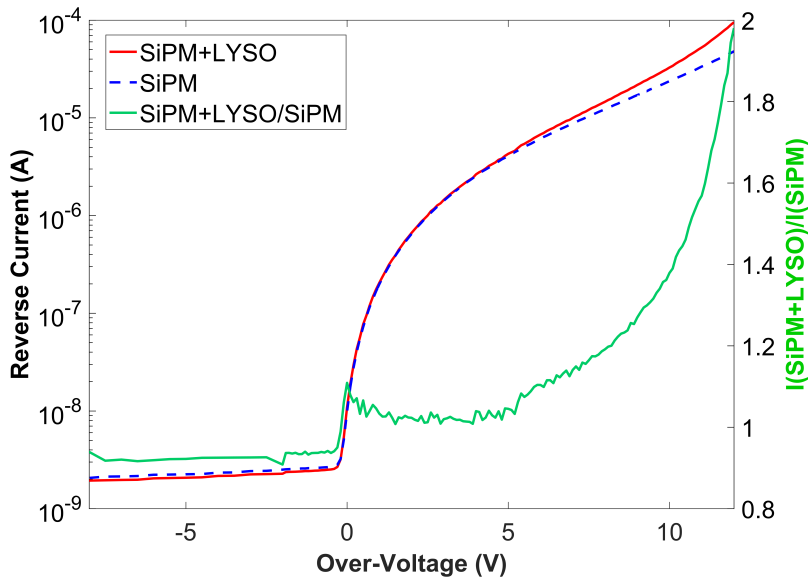


**Figure 4.15:** IV curve of the 25 $\mu$m SiPM coupled to LYSO crystal (red line) and without crystal (blue line). The green line shows the ratio between the two IV curves [105].

SiPM is significantly larger at high over-voltage, because of the correlated noise. Indeed, as explained in [115], the scintillator can reflect back towards the SiPM part of the photons emitted by the hot electrons during an avalanche, increasing the probability of optical cross-talk. The ratio between the two curves, plotted on the right axis, can be considered as the Excess Charge Factor (ECF) due to the scintillator. This effect is less important at 511 keV, because the number of generated photons is

approximately half of the ones generated at 1274 keV. The effect is negligible with the 15-20 $\mu$m cells either, because of the lower correlated noise combined with the higher cell density. This shows the effectiveness of reducing the cell size in removing the non-linear effect of the SiPMs.

From the measurement of the different cells of RGB-HD and RGB-UHD technologies, we estimated the intrinsic resolution of the 4x4x22 mm$^3$ and 3x3x15 mm$^3$ LYSO crystals used in the setup. The reported resolution is the average of the values obtained at different over-voltages, with the exception of the 25 $\mu$m cell at 1274 keV where we use only the over-voltages of up to 5 V. Table 4.3, and Table 4.4 show the values and the related errors obtained for 511 keV and 1274 keV for the two crystal sizes. The values of the intrinsic resolution obtained for each LYSO dimension with the different cell sizes are compatible within $2\sigma$. These values are also comparable to other values reported in the literature [116, 117].

**Table 4.3:** Intrinsic resolution of 4x4x22 mm$^3$ LYSO crystals at 511 keV and 1274 keV.

| Cell pitch ($\mu$m) | Technology | $R_i$ at 511 keV (%) | $R_i$ at 1274 keV (%) |
|---|---|---|---|
| 15 | RGB-HD | $8.8 \pm 0.4$ | $6.5 \pm 0.15$ |
| 20 | RGB-HD | $8.6 \pm 0.2$ | $6.2 \pm 0.15$ |
| 25 | RGB-HD | $8.3 \pm 0.2$ | $6.3 \pm 0.2$ |

**Table 4.4:** Intrinsic resolution of 3x3x15 mm$^3$ LYSO crystals at 511 keV and 1274 keV.

| Cell pitch ($\mu$m) | Technology | $R_i$ at 511 keV (%) | $R_i$ at 1274 keV (%) |
|---|---|---|---|
| 10 | RGB-UHD | $9.6 \pm 0.6$ | $8.0 \pm 0.6$ |
| 12.5 | RGB-UHD | $9.6 \pm 0.1$ | $7.6 \pm 0.4$ |

As explained in Sec. 3.3.2 of the previous chapter, from the calibration of the LED setup at 511 keV it is also possible estimate a light collection coefficient for the used LYSO crystal, see Eq. 3.24. Fig. 4.16 shows the number of photons sent to a 20 $\mu$m-cell SiPM with the LED setup to simulate the LYSO signal at 511 keV, as a function of the over-voltage.
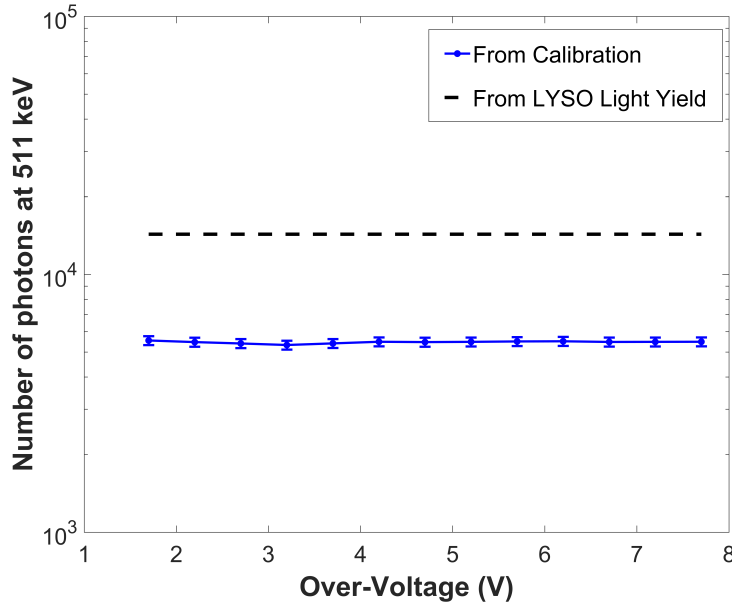
**Figure 4.16:** Number of photons as a function of over-voltage which are necessary to calibrate the LED setup at 511 keV for the 20 $\mu$m-cell. The dashed line represents the theoretical number of photons generated in a LYSO crystal, i.e. supposing an absolute light yield of 32 ph/keV [113]. Relative errors on the number of photons are between 2.5% and 3%, they include calibration errors.

Table 4.5, and Table 4.6 report the light collection efficiencies that were calculated for two different crystal sizes: 4x4x22 mm$^3$ and 3x3x15 mm$^3$, respectively. Each value is the average of the values obtained at the different over-voltages. Light collection coefficients obtained for each LYSO dimension with the different cell sizes are compatible within $2\sigma$. The obtained data have been also compared to the data published in [118]. In this paper the light collection coefficient was simulated for two different LYSO dimensions, considering different coupling (with silicon or epoxy resins), and different wrapping conditions (with adhesive thickness or reflective film). For similar conditions, i.e. 4x4x22 mm$^3$ LYSO, silicon resin, optical grease, and reflective film, our values are comparable to values presented in this paper within a difference of $\sim$10%. The difference of the light collection coefficient, $\alpha$, for the two sizes of the LYSO crystals could be addressed to the different *aspect ratio*. The *aspect ratio* is the ratio between readout area and the length of the crystal [119], and it affects the light absorption inside the crystal. For the two sizes of the crystals, the *aspect ratio* are: 0.60 for the 3x3x15 mm$^3$ LYSO and 0.73 for the 4x4x22 mm$^3$ LYSO. A higher *aspect ratio* improves the light collection, and thus $\alpha$.

**Table 4.5:** Light collection coefficient ($\alpha$) for 4x4x22 mm$^3$ LYSO crystals used in our measures.

| Cell pitch ($\mu$m) | Technology | $\alpha$ (%) |
|---|---|---|
| 15 | RGB-HD | $33.5 \pm 0.9$ |
| 20 | RGB-HD | $33.4 \pm 1.0$ |
| 25 | RGB-HD | $33.3 \pm 1.6$ |

**Table 4.6:** Light collection coefficient ($\alpha$) for 3x3x15 mm$^3$ LYSO crystals used in our measures.

| Cell pitch ($\mu$m) | Technology | $\alpha$ (%) |
|---|---|---|
| 10 | RGB-UHD | $24.6 \pm 2.4$ |
| 12.5 | RGB-UHD | $23.9 \pm 0.6$ |

## 4.6    Non-linearity

In this section we show the non-linearity characterization of the SiPMs performed with the LED setup, as explained in Sec. 3.2.2. Measurements were carried out in a thermostatic chamber at a fixed temperature of 20 $^o$C. Relative errors on the non-linearity are between 4% and 9%. They are omitted for clarity in the graphs.

Fig. 4.17 shows the non-linearity as a function of the energy for the different cell sizes at 6 V of over-voltage, which is the OV that on average corresponds to the best energy resolutions. As expected the non-linearity increases with cell size, because of the lower cell density and the resulting SiPM saturation. The smallest cells, fabricated in UHD technology, are almost perfectly linear up to 30 MeV. Also the 15 $\mu$m HD technology shows an almost linear behaviour in the considered energy range.

Fig. 4.18 shows the non-linearity as a function of the energy for 20 $\mu$m cell size, at different over-voltages. The top x-axis shows the number of photons impinging on the SiPM surface at each energy. As expected, the non-linearity increases with the over-voltage, as a consequence of the increase of both PDE and correlated noise. Other cell sizes show a similar trend.

Fig. 4.19 shows the non-linearity at 5 MeV as a function of the PDE for different cell sizes and over-voltages. In the plot, it is possible to compare the PDE that
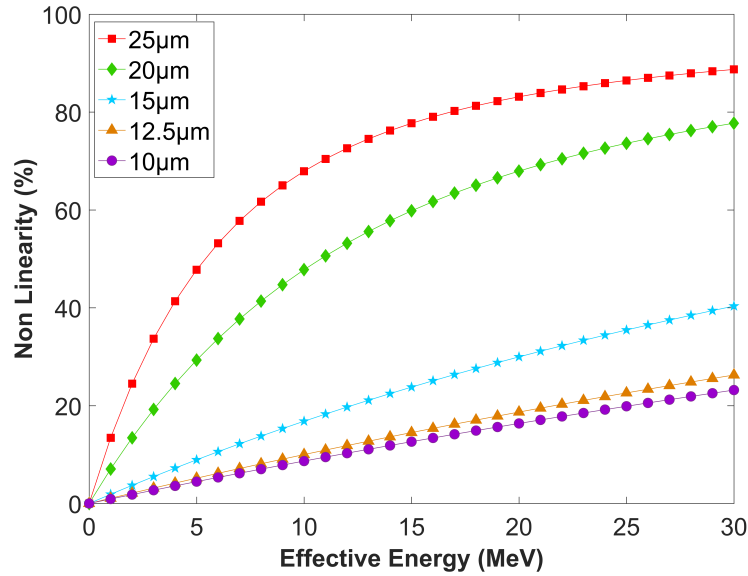
**Figure 4.17:** Non-linearity as a function of the energy for the different cell sizes at 6 V over-voltage [105].
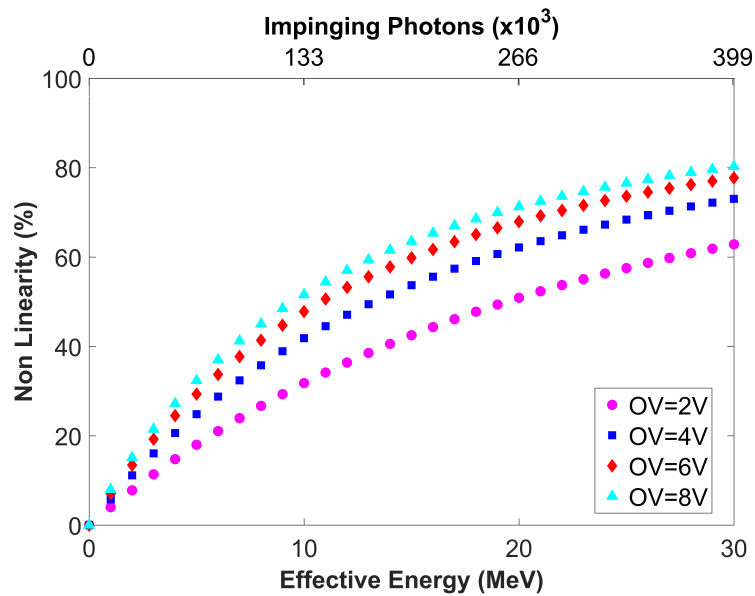


**Figure 4.18:** Non-linearity as a function of the energy (bottom x-axis) and impinging photons (top x-axis) for 20 $\mu$m cell at different over-voltages [105].
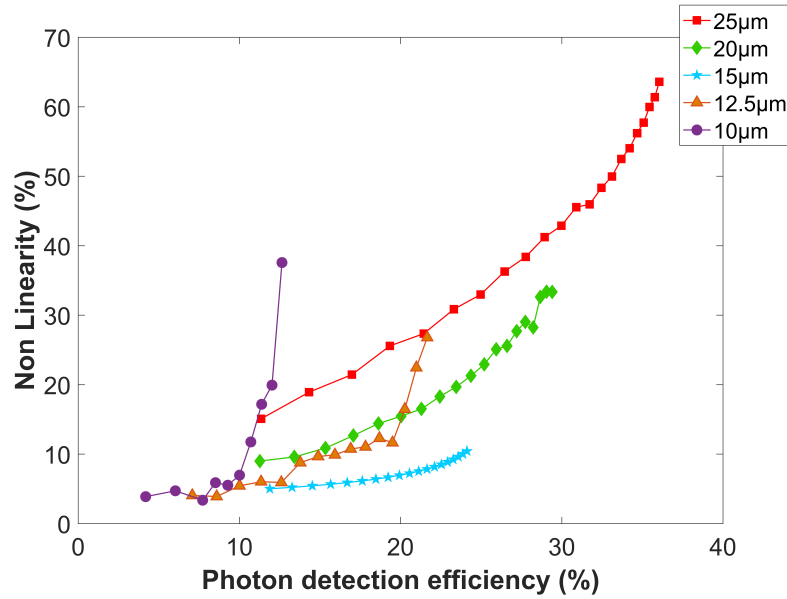
**Figure 4.19:** Non-linearity as a function of the PDE for the different cell sizes, at the energy of 5 MeV. Changes of PDE are obtained by applying different over-voltages to the SiPMs [105].

the different SiPMs can provide at a given value of non-linearity. This comparison is motivated by the assumption that NL can be set as a specification in certain applications. For example, setting NL=5 %, 15 $\mu$m cell reaches the highest PDE. The divergence in the SiPMs with 10 $\mu$m and 12.5 $\mu$m cell is caused by the bad quenching at high over-voltage.

As explained in Sec. 3.3, the charge spectrum is obtained by integrating over time the voltage signals generated in a SiPM. This allows us to calculate the number of fired cells in a SiPM. Fig. 4.20 shows the number of triggered cells per second as a function of the number of impinging photons in a 25 $\mu$m-cell SiPM for different over-voltages. At a fixed number of impinging photons the number of triggered cells increase with over-voltage due to the higher PDE. It can be noted that the number of triggered cells exceeds the number of SiPM cells (dashed line). This effect is due to the cell recovery: a short recovery time, compared to the entire duration of the light pulse, allows a cell to re-trigger during the light pulse, even when the cell is not fully recharged.

Fig. 4.21 shows the occupancy of cells, i.e. the ratio between the triggered cells and the number of cells of a SiPM, as a function of impinging photons for different cell sizes, and a 4 V over-voltage. As expected, fixing a number of impinging pho-
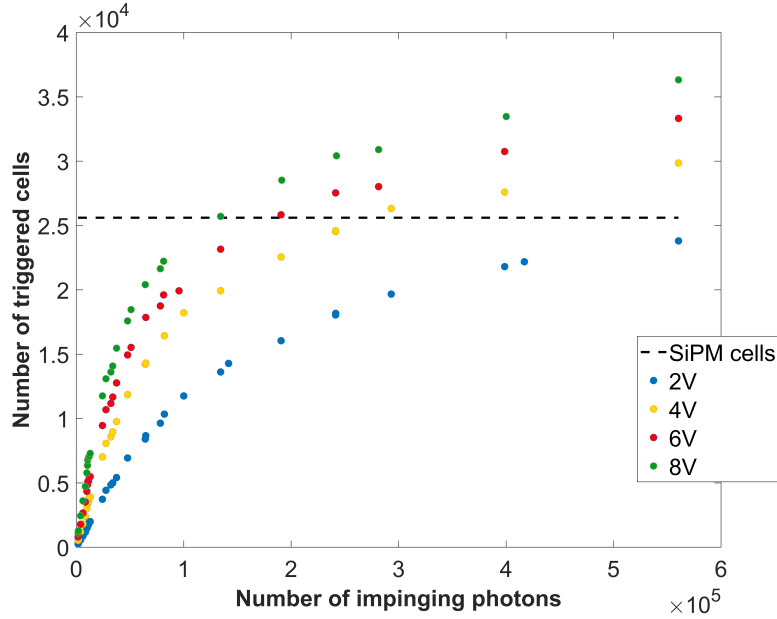
**Figure 4.20:** Number of triggered cells/s as a function of the number of impinging photons in a 25 $\mu$m-cell SiPM for different over-voltages. The black dotted line indicates the number of cells in the SiPM. Relative errors on triggered cells are between 3 and 6% and on the impinging photons is ~1%.

tons, the occupancy of cells increase with cell size because of the lower cell density, higher PDE, and longer recovery time. This figure highlights the importance of having a high-cell density to reduce the saturation of SiPMs when a high-dynamic range is required.

Fig. 4.22, and Fig. 4.23 show cell recovery times as a function of the over-voltage for different cell sizes of the HD and UHD technologies. These times are calculated as explained in Sec. 2.2.3. The recovery time increases with cell size because of the higher cell capacitance. It also decreases with the over-voltage because of the decrease of the capacitance, which is caused by the progressive depletion of the epitaxial layer with the over-voltage, causing a progressive reduction of the cell capacitance. HD SiPMs have recovery times in the order of tens of nanosecond, which are comparable with the LYSO decay time. Recovery times of UHD SiPMs are instead in the order of a few nanoseconds, much smaller than the LYSO decay time. Thus, the short cell recovery times are very important to improve performance of a SiPM in this kind of applications. In particular, they provide a reduction of the SiPM saturation, as a consequence of the re-trigger phenomenon, described in
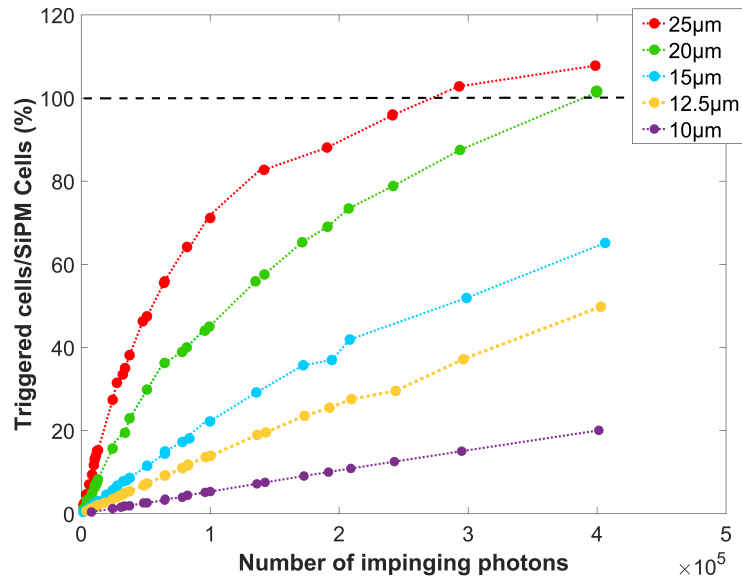
**Figure 4.21:** Occupancy of cells, i.e. the ratio between the triggered cell and the number of cells, of a SiPM as a function of impinging photons for different cell sizes, and a 4 V over-voltage.
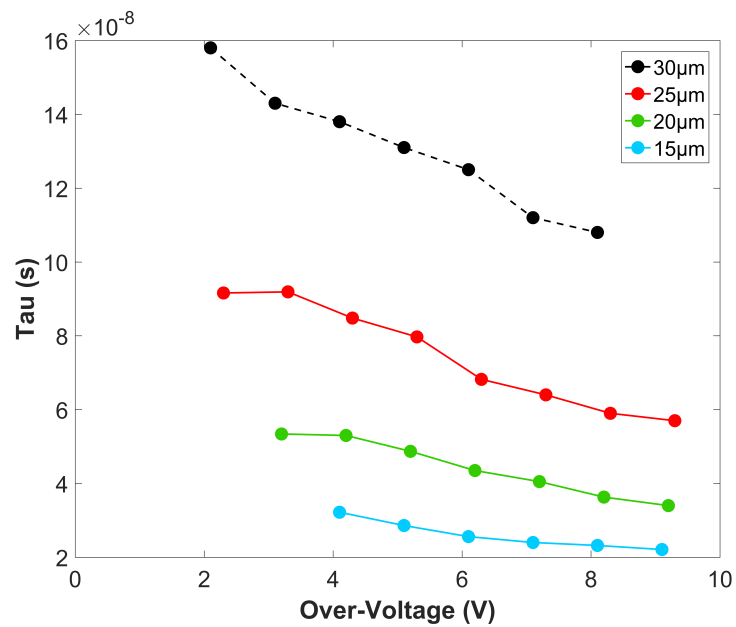


**Figure 4.22:** Cell recovery times as a function of the over-voltage for different cell sizes of the HD technology.
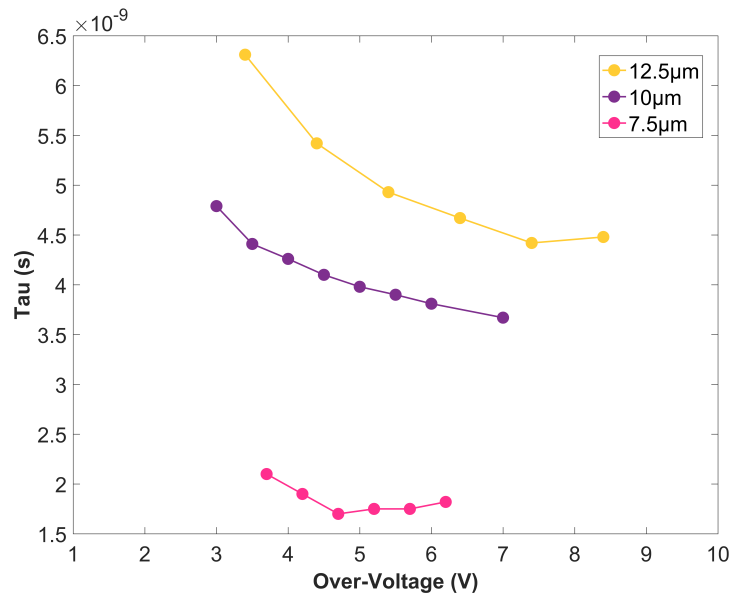
**Figure 4.23:** Cell recovery times as a function of the over-voltage for different cell sizes of the UHD technology.

Sec. 2.2.4, and a reduction of the pile-up effect because of very fast signals, i.e. 15 ns with 12.5 $\mu$m-cells.

## 4.7 Energy resolution versus non-linearity

This section presents the correlation between energy resolution and non-linearity at the same over-voltage. Fig. 4.24 shows the non-linearity as a function of the energy resolution for the different SiPMs at 5 MeV, in the middle of the useful energy range of the PGI. Fixing the NL threshold, it is possible to obtain different energy resolutions with different cell sizes, i.e. at 5% of NL the best energy resolution is provided by 15 $\mu$m-cell. Instead, Fig. 4.25 shows the results at higher energy: 10 MeV. The deterioration of the energy resolution because of the NL, and thus of the corresponding ENF, is clearly visible for the 25 $\mu$m-cell. In PGI both good energy resolution and low non-linearity are required. Thus the best trade-off has been identified as a cell size between 12.5 $\mu$m and 15 $\mu$m. The acquisition part (ASIC and DAQ) of the gamma-camera of Gammarad project will be optimized for an energy range between 2 MeV and 8 MeV, thus slightly lower than 10 MeV. Thus, the chosen microcell is the 15 $\mu$m. Instead, for higher energy the use of smaller cell
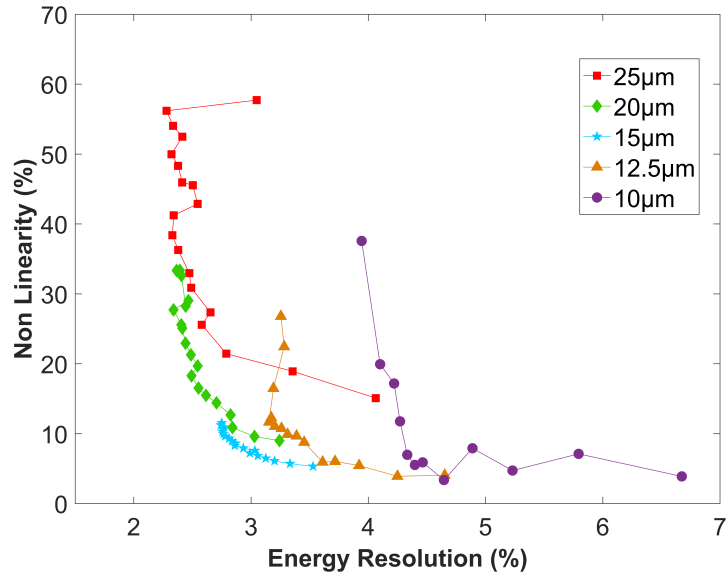
**Figure 4.24:**   Non-linearity as a function of the energy resolution at 5 MeV for different cell sizes [105].
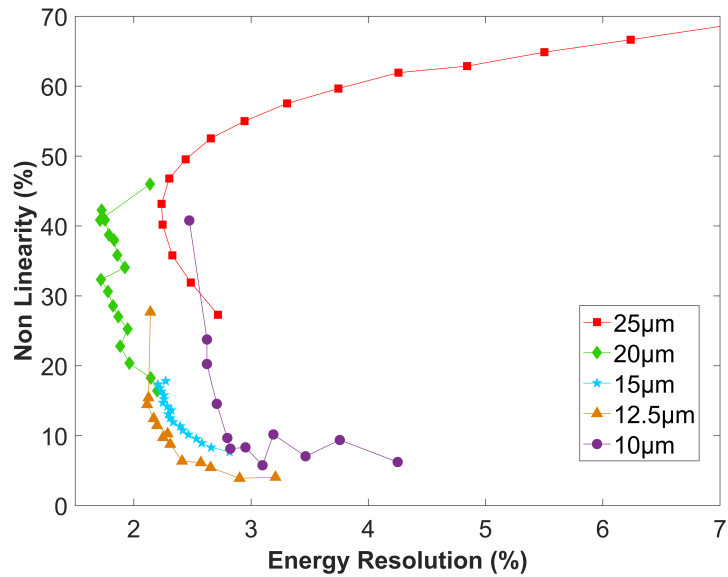


**Figure 4.25:**   Non-linearity as a function of the energy resolution at 10 MeV for different cell sizes [105].

sizes seems to be more profitable. New developments of the UHD technology are in progress. First results are promising in terms of PDE, but new developments are required to reduce the DCR [76].

Summarizing, because of the results presented in this chapter, the RGB-HD SiPMs with the 15 $\mu$m-cell size will be used to produce the first module of the gamma camera, which is composed of a tile of 64 SiPMs, independently read-out in a single-ended configuration. The characterization of this module is presented in the next chapter.

# Chapter 5

# Photo-detector module

In this chapter is presented the R&D activity carried out to produce the photo-detector module of the gamma camera that will be used for PGI applications. The production of this module requires research on packaging techniques to solve two main challenges: the maximization of the photo-sensitive area and the application of a protective resin, transparent in the near UV, to maximize light collection from the LYSO. In the last part of the chapter, we show the characterization of the photo-detector array in terms of energy resolution, position sensitivity and non-linearity. Measurements on the photo-detector module were carried out together with the Politecnico di Milano, who is a partner of Gammarad and provided the ASIC and a temporary DAQ for the readout.

# 5.1   Construction of the photo-sensor module

On the basis of the characterization results shown in Chapter 4, HD SiPMs with an active area of 4x4 mm$^2$, and cell size of 15 $\mu$m were chosen to produce the photo-detector module of the gamma camera (GDM), which is optimized in the range between 2 MeV and 8 MeV. The schematic of the GDM has been presented in Sec. 1.4. A single module of the GDM consists of an array of 64 SiPMs arranged in a square layout (8x8), which is called a tile. The devices within the tile have electrical characteristics as uniform as possible. Because of the reproducibility of FBK's SiPM technology, the selected SiPMs have breakdown voltage variations within 100 mV and a good uniformity of dark currents, as shown in Fig. 5.1.
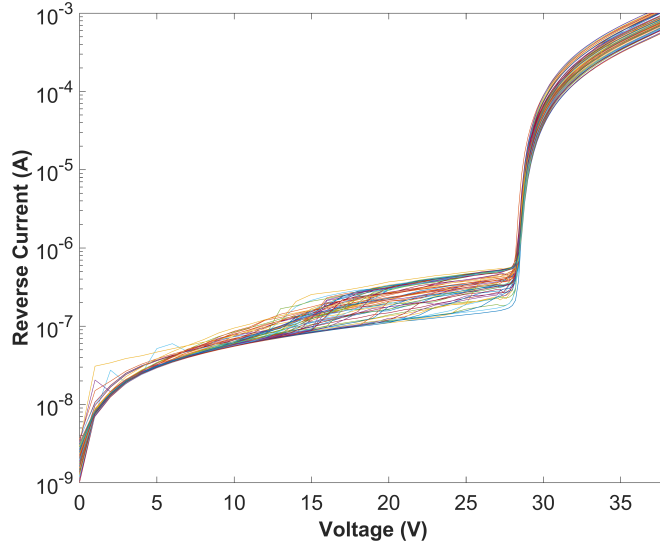


**Figure 5.1:**   Reverse IV curves of the 64 SiPMs of the tile.

As explained in the introduction of this chapter, the production of the tile requires research on packaging techniques to solve two main challenges: the maximization of the photo-sensitive area and the application of a protective resin.

The maximization of the photo-sensitive area is obtained by minimizing the dead regions between SiPMs (gaps). This was achieved by designing a dedicated PCB for the tile and a slim edge technology in the SiPM layout. Slim edge means that the distance from the active area of the last cell of the SiPM and the die cut-line is around 50 $\mu$m. Fig. 5.2 shows the designed SiPMs for Gammarad project (a) and the 8x8 tile produced with these SiPMs (b) with the relevant dimensions. The

(a) SiPM layout for Gammarad          (b) PCB for the 64-channels Gammarad tile
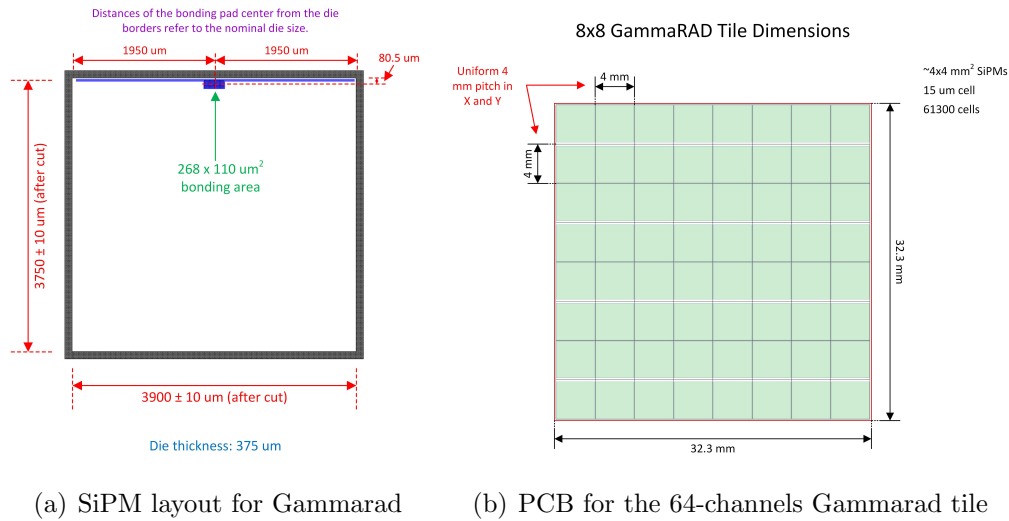
**Figure 5.2:** Pictures of SiPM layout for Gammarad project (a), and of the PCB for the tile of 64 channels (b).

placement of each SiPM was difficult because of the thin gaps between neighbouring devices, only 80 $\mu$m on three sides and 400 $\mu$m on the side used for the bonding connection. Furthermore, each contact between adjacent SiPMs must be avoided because they are read-out independently. In Fig. 5.3 two microscope pictures show the SiPM placement (a) and a detail of the bonding connections (b). To comply with these specifications, a semi-automatic pick and place machine was used in FBK. It is important to note that this machine was never used before with such tight specifications. In addition, the distance between the SiPM along the bonding side required the use of a deep access bonding tool, and the modification of the bonding procedure and parameters.

The application of a protective resin is the second challenge. This resin layer has to protect the bonding wire, the SiPMs surface, and to improve the optical coupling between the tile and the crystal scintillator array. After having studied and tested many resins, a silicone resin with a transparency higher than 99% (above 300 nm) and a high resistance to heat and ageing, was chosen. This new type of resin required the development of a procedure to obtain a perfectly uniform and planar surface, and to avoid the formation of air bubbles inside the resin during polymerization. To avoid the formation of air bubbles, it was developed a degassing technique, carried out under vacuum and at moderate temperature. Finding the correct temperature was one of the challenges because a compromise must be found
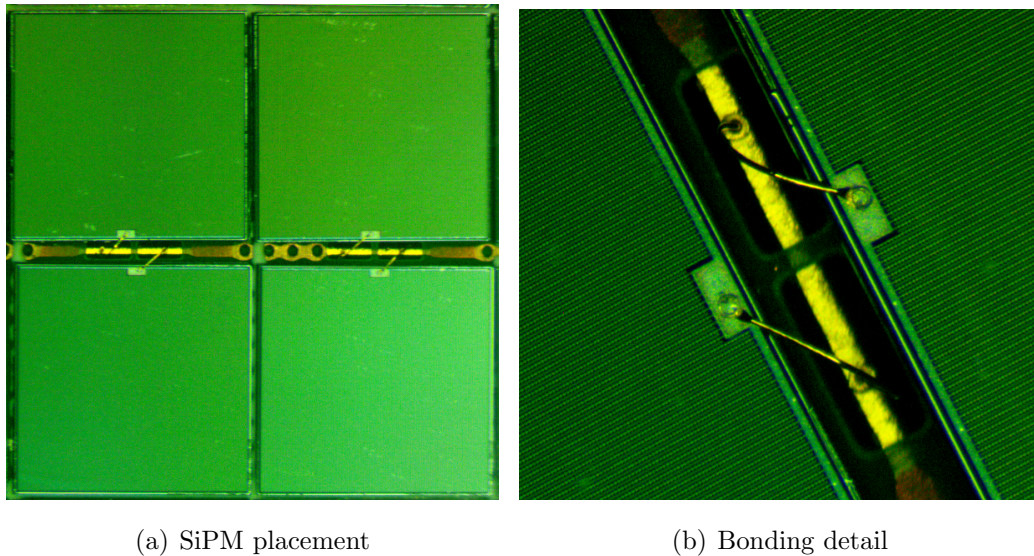
(a) SiPM placement
(b) Bonding detail

**Figure 5.3:** Microscope pictures of SiPM placement on the tile (a) and the detail of the bonding connections (b).

between the polymerization speed, which increases with the temperature, and the resin viscosity, which instead decreases with the temperature and helps removing the air bubbles.

After this R&D on packaging, we obtained a fully functional tile with 64 SiPMs with a fill factor, i.e. ratio between the photo-sensitive area of all the SiPMs and the total area of the tile, of ∼86%. This fill factor is comparable with values obtained when a Through Silicon Vias (TSVs) technique is employed to connect SiPMs but without the high production cost, and the additional fabrication process complexity of the TSV. It should be highlighted that all these operations are very critical in terms of yield. It is in fact necessary to produce a tile with all working SiPMs, since defective items can not be replaced at a later stage. Fig. 5.4 shows images of a prototype tile with 16 channels and of the fully functional tile with 64 channels, both covered with the protective resin with a thickness of approximately 700 $\mu$m. The tile with 64 SiPMs will be coupled to a 64-pixels LYSO crystal to form the photo-detector for the Gammarad project.

The readout of this photo-detector is obtained by means of multi-channel ASICs and a general-purpose DAQ. The ASIC was developed and provided by Politecnico di Milano, a partner of Gammarad project, who provides also a temporary DAQ. The Trento Institute for Fundamental Physics and Applications (TIFPA), instead,
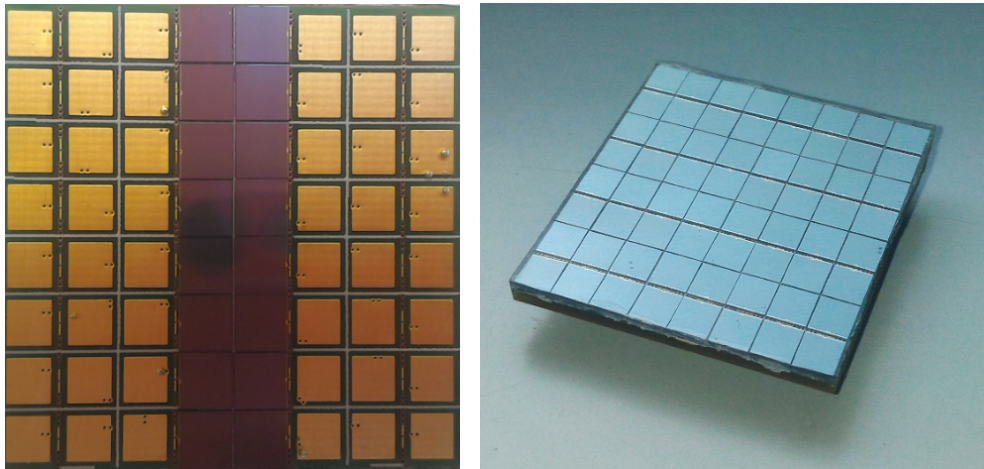
(a) 16-channels prototype tile            (b) Fully functional tile of 64 channels

**Figure 5.4:**    Pictures of a prototype tile with 16 channels (a) and of the fully functional tile with 64 channels (b). Both the tiles are covered with the protective resin with a thickness of approximately 700 $\mu$m.

is developing the final DAQ. The characterization of the photo-detector array in terms of energy resolution, position sensitivity, and non-linearity, was carried out jointly with Politecnico di Milano and is presented in sec. 5.3.

## 5.2   Photo-sensor readout

In this section, we give a brief overview on the tile readout system designed at Politecnico di Milano. This readout is described in detail in [120, 121]. The output signals of the 64 SiPMs are read by two 36-channel front-end ASICs, designed in CMOS 0.35 $\mu$m technology: ANGUS [120]. Fig. 5.5 shows the schematic structure of one channel of ANGUS. The SiPM current is read by a current conveyor stage, which scales it to a proper amplitude for the following RC filter. The peak of the signal is fed to a sample and hold for A/D conversion. Two ASICs are needed to read all the 64 SiPMs. They are placed on their respective boards and are connected to a motherboard. The motherboard is responsible for SiPMs placement and provides the connection between the photo-detector and the two ASICs, and between the two ASICs and an external Data Acquisition System (DAQ). ANGUS was developed for SPECT applications, which have energy of up to 250 keV and a monolithic scintillator crystal. Instead, the expected Gammarad energy spectrum has energy of
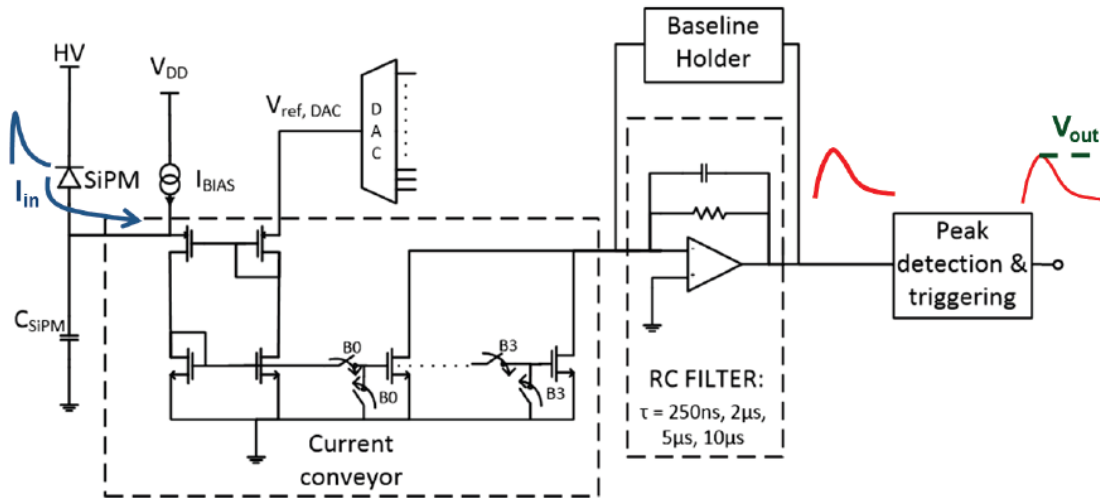
**Figure 5.5:** Schematic structure of one channel of ANGUS. Picture from [120], copyright 2014, IEEE.

up to 8 MeV and the scintillator crystal is pixelated. As a consequence, the SiPM output current is too large for the ASIC. Thus, a current reduction filter, shown in Fig. 5.6, was designed and placed on the motherboard to match the limited peak input current that the chip can handle (maximum of 4 mA) [121]. To stabilize the
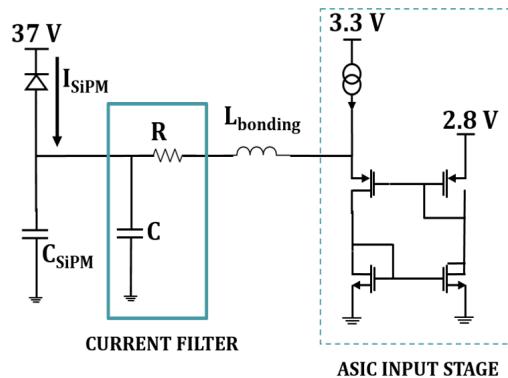


**Figure 5.6:** Schematic representation of the current reduction filter [121].

SiPM gain in real-time during the measurements, we used a temperature stabilization strategy based on a micro-controller control loop. The temperature information is given by a Pt100 sensor placed on the bottom of the SiPMs board. An external power board provides all the required bias voltages from an external 12 V power supply. Fig. 5.7 shows the complete detection module. The tile with 64 SiPMs is coupled to 64-pixels LYSO crystal, both are shown in Fig. 5.8, by using BC-630
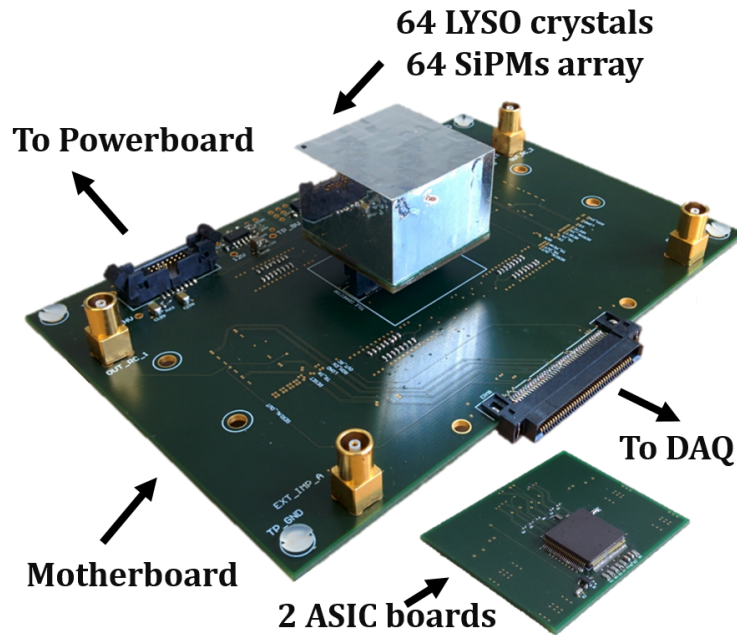
**Figure 5.7:** 64 pixels photo-detector [121].

silicone optical grease from Saint Gobain. As explained in Chapter 3, we decided to use a pixelated crystal, with the dimensions of 32x32x22 mm$^3$, which is made of an array of small blocks of 4x4x22 mm$^3$. Thus, it is possible to couple 1:1 a scintillator pixel and a single SiPM, to reduce the probability of pulse piling-up at high count rate, and to provide 2D spatial information.

During the measurements this module is placed inside a light-tight box to ensure dark conditions. Data are transferred to a PC and elaborated with a Matlab software.

## 5.3 Characterization of the photo-detector

In this section, the characterization of the photo-detector module is presented. A PGI detection module has to reconstruct a 1-dimensional projection, or profile, of the beam path on the scintillator by detecting prompt gamma-rays. These gamma-rays are emitted along the beam path, and are correlated with the Bragg peak position. A slit collimator is generally used to project the beam profile onto the gamma detector. Measurements to test global performance of the photo-detector, in order to verify its capability for PGI applications, are:

(a) Tile with 64 SiPMs                    (b) Pixelated LYSO crystal
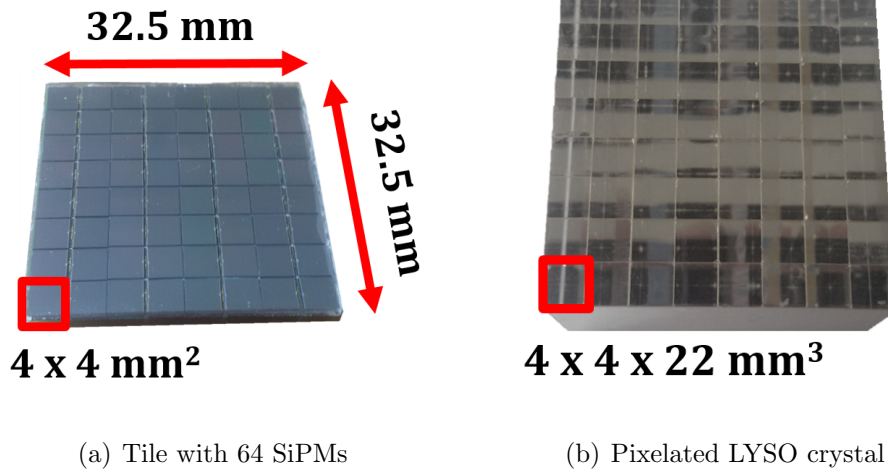
**Figure 5.8:**  Pictures of the tile with 64 SiPMs (a) and of the LYSO crystal with 64 pixels (b). The pitches are 4 mm to allow 1:1 coupling.

- **Energy Resolution**: this measurement regards spectroscopic performance of the photo-detector (with pixelated LYSO crystal) with energy of up to 1.3 MeV. The obtained energy resolution is compared to a previously developed gamma camera for PGI applications [37]. These measurements were carried out together with Politecnico di Milano at its Radiation Detectors and Applications laboratory in Milan.

- **Position Sensitivity**: this measurement regards the position sensitivity of the photo-detector (with pixelated LYSO crystal) and aims at verifying if the photo-detector module has a sufficient imaging capability to reconstruct the prompt gammas profiles. These measurements were carried out by Politecnico di Milano at the laboratory of INFN (Istituto nazionale di Fisica Nucleare) in Milan.

- **Non-linearity**: this measurement regards spectroscopic and linearity performance of the photo-detector (without pixelated LYSO crystal) with high-energy gamma-rays. High-energy gamma-ray sources are not easily found outside authorized structures and thus the module was tested at higher energies (up to 13 MeV) with the LED setup presented in Sec. 3.3. These measurements were carried out jointly with Politecnico di Milano at the Gamma Laboratory of Fondazione Bruno Kessler in Trento.

### 5.3.1  Energy resolution test

The energy resolution was tested with $^{137}$Cs (662 keV) and $^{60}$Co (1173 keV, 1333 keV) gamma-ray sources. The energy resolution was estimated with the standard method described in Sec. 3.3. Fig. 5.9 shows the setup used for these spectroscopy measurements, as described in Sec. 5.2. The energy resolution was measured for all 64 SiPMs
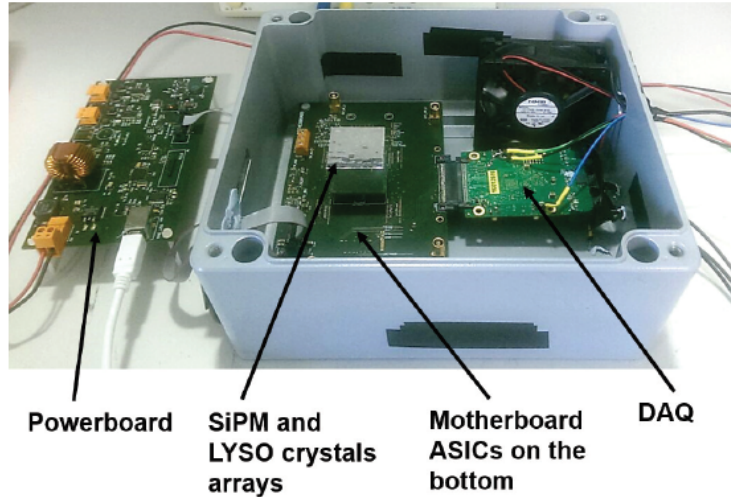


**Figure 5.9:**  Picture of the experimental setup used for spectroscopy measurements. Provided by G. Cozzi.

of the tile. Fig. 5.9 shows an example of measured energy resolutions of the SiPMs of the tile for the energy peak of the $^{137}$Cs. The average energy resolution of the tile is obtained by averaging energy resolutions of the 64 SiPMs. Table 5.1 lists the results for each energy considered. Spectroscopy results are in agreement with

**Table 5.1:**  Averages of 64 SiPM energy resolutions for each energy at 8 V of over-voltage. These values are compared to the energy resolution of a previously developed gamma camera for PGI applications [37].

| Energy | Energy resolution | Energy resolution [37] |
|:---:|:---:|:---:|
| (keV) | (%) | (%) |
| 662 | 12.7±0.8 | 13.8±0.6 |
| 1173 | 9.0±0.4 | 9.2±0.2 |
| 1333 | 8.8±0.3 | 8.4±0.1 |

the energy resolution measured on single samples of SiPM, coming from the same
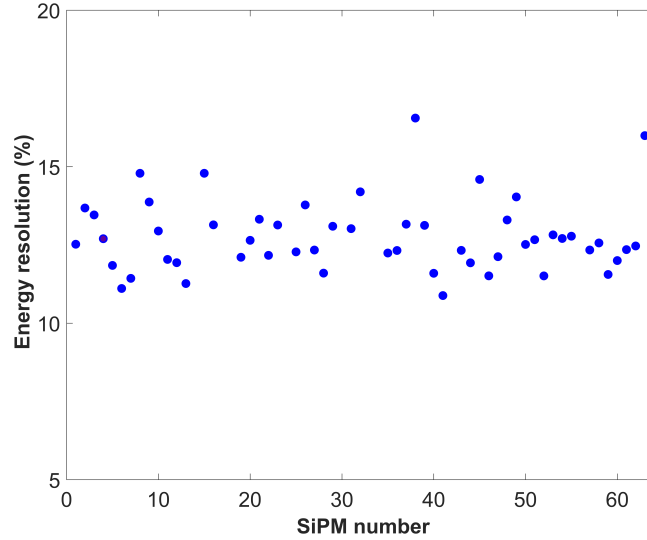
**Figure 5.10:**  Energy resolutions of the 64 SiPMs on the tile at 662 keV and 8 V of over-voltage.

production run and readout with standard, discrete electronics. Furthermore, these results are comparable to the energy resolution of a previously developed gamma camera for PGI applications [37].

## 5.3.2   Position sensitivity characterization test

As mentioned in the introduction of this section, the position sensitivity of a photo-detector allows to obtain a 1-D profile of the impinging gamma-rays on the pixelated crystal. Ideally, in a pixelated crystal the position of interaction is identified by the fired pixel because the energy of a single gamma-ray is absorbed by a single pixel. However, it is possible that a single gamma-ray event releases part of its energy also in the neighbouring pixels. To evaluate the position sensitivity of our gamma detector, we test if the position response is in agreement with the pixel size, which in our case is 4x4 mm$^2$. The position sensitivity of the module was evaluated along one direction because the photo-detector has a symmetric structure.

Fig. 5.11 shows the experimental setup for position sensitivity measurements. This setup features a mechanical structure that moves a collimator on an x-y plane with one millimeter accuracy. The collimator is a Tungsten-based alloy, 10 cm long, and has a hole of 1 mm. The collimated source is the $^{137}$Cs. The photo-detector module was placed at a distance of 5 cm in front of the collimator hole. The position
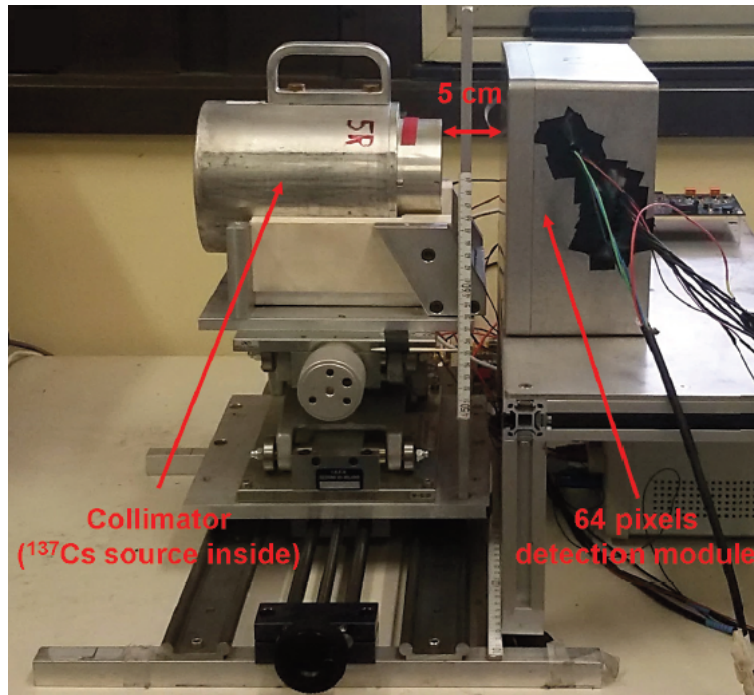
**Figure 5.11:** Picture of the experimental setup for position sensitivity measurements. Provided by G. Cozzi.

sensitivity was evaluated from the Point Spread Function (PSF) of the pixels by scanning the photo-detector module in different positions along the y-axis.

Fig. 5.12 (a) shows a scheme of the y-axis scan from 0 to 32 mm. Each spot has a diameter of 1 mm and two consecutive spots are separated by 1 mm. Fig. 5.12 (b) shows the PSF of the 8 pixels as a function of the source position, numbered according to the notation of the scheme in (a). Each point represents normalized counts of energy spectra inside an energy window (two energy thresholds were used to accept the counts for each pixel) for each spot position. The PSFs have a Gaussian shape, and not an ideal rectangular shape, because in real conditions there is a certain probability that some events release a fraction of energy also in the neighbouring pixels. As expected, the maximum of the PSF is reached when the source is aligned with the center of each pixel. Table 5.2 reports the FWHM of the Gaussian fit for each PSF. The photo-detection module shows a spatial resolution comparable to the SiPM dimension of 4 mm. Thus, this module can be used to reconstruct images of a 1-D profile of prompt gamma-rays.
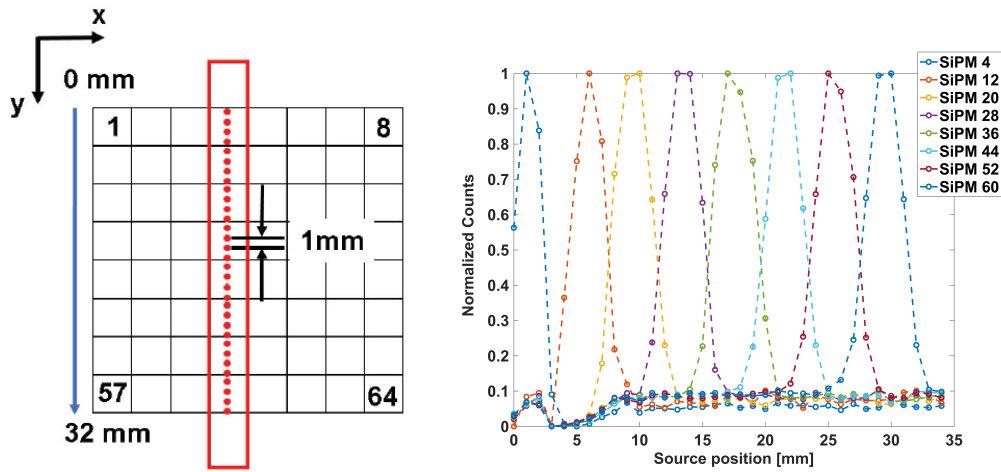
(a) Scheme of the irradiation spots                    (b) PSF of the 8 pixels.

**Figure 5.12:**   Scheme of the irradiated spots (a).  Point Spread Function of the 8 pixels as a function of the source position (b). Data provided by G.Cozzi.

**Table 5.2:**   FWHM of the Gaussian fit for measured PSFs of the 8 pixels.  Data provided by G.Cozzi.

| Pixel number | FWHM |
| --- | --- |
| | (mm) |
| 4 | 2.29±0.78 |
| 12 | 3.17±1.44 |
| 20 | 3.53±1.09 |
| 28 | 3.60±1.11 |
| 36 | 4.08±1.24 |
| 44 | 3.63±1.10 |
| 52 | 3.96±1.17 |
| 60 | 3.84±1.22 |

### 5.3.3 Non-linearity test

To evaluate the Non-Linearity (NL) and the energy resolution of the photo-detector module in high-energy gamma-ray spectroscopy, the method and the setup described in Sec. 3.3 were used. Fig. 5.13 shows the placement of the photo-detector module in front of the setup for the simulation of high-energy gamma-ray response. Both the LED setup and the photo-detector module are in a thermostatic chamber to have the dark condition and to keep the temperature stable. This LED setup was aligned
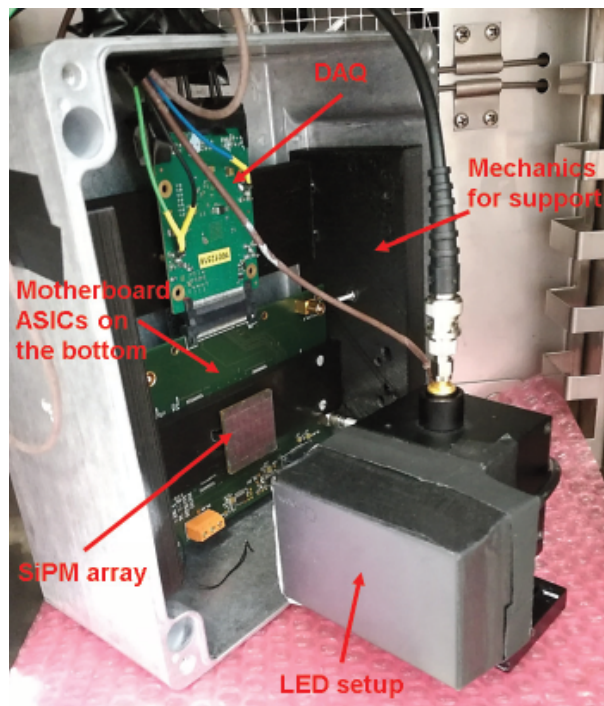


**Figure 5.13:** Picture of the photo-detector module in front of the setup for the simulation of high-energy gamma-ray response.

to illuminate one central SiPM of the tile. This tile is placed at the distance of $\sim 5.6$ cm, which was used to calibrate the reference diode, as described in Sec. 3.3.2, to guarantee an uniform illumination on the SiPM area. A preliminary calibration was performed to find the correct emission of the LED that simulates the signal produced in the SiPM + AISC system when a 511 keV photon interacts with the LYSO scintillator. This calibration in energy allows also to find the optimal ASIC settings, i.e. a gain of 3 and a shaping time of 800 ns, for the detection of the higher energy photons between 2 and 8 MeV. After the calibration different numbers of photons, and thus different energies, were generated with the LED setup.

Fig. 5.14 shows measured peak positions in ADC channels as a function of the energy. The green-dashed line is the ideal response of the photo-detector extrapolated from a linear fitting of the first data points (up to 2 MeV) where the 15 $\mu$m RGB-HD SiPMs non-linearity is negligible, see Fig. 4.17. As expected from the consideration on a single SiPM, see Sec. 3.2.2, the non-linearity of the photo-detector module increases with the energy because of the increasing number of photons which saturates the SiPM cells. A new calibration of the complete photo-detector module
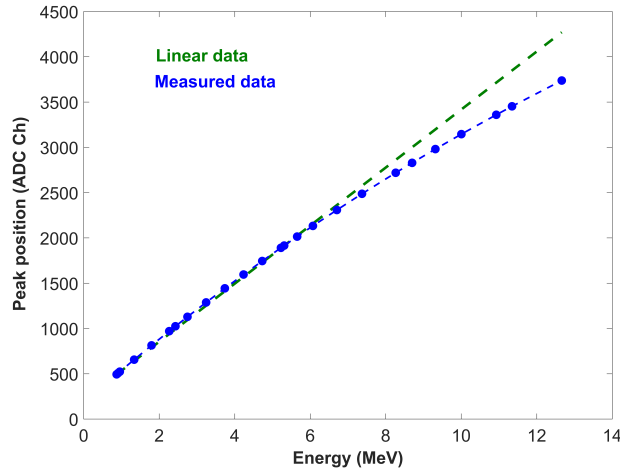


**Figure 5.14:** Measured peak positions (in ADC channels) as a function of the simulated gamma-ray energy. The green-dashed line represents a linear response of the photo-detector module.

was performed, taking into account the non-linear behaviour of both SiPMs and ASIC, using the following equation:

$$ADC_{Ch}(E) = a \cdot \left( 1 - e^{-\frac{E}{b}} \right) + c, \tag{5.1}$$

where $a$ and $b$ are the fit coefficients due to the non-linearity, and $c$ is due to an ASIC offset. Maximum fitting errors are lower than 1%, confirming the agreement between experimental data and Eq. 5.1. Eq. 5.1 was used to calibrate the acquired spectra for energies between 800 keV and 13 MeV. Fig. 5.15 shows the corresponding energy spectra. The FWHM of each energy peak is used to calculate the energy resolution of the photo-detector module without the term due to the intrinsic resolution of the scintillator crystal, as explained in Sec. 3.3.1. Fig. 5.16 shows these energy resolutions as a function of the energy compared to a theoretical resolution. This theoretical resolution is the sum between the statistical resolution, see Sec. 3.2.1,
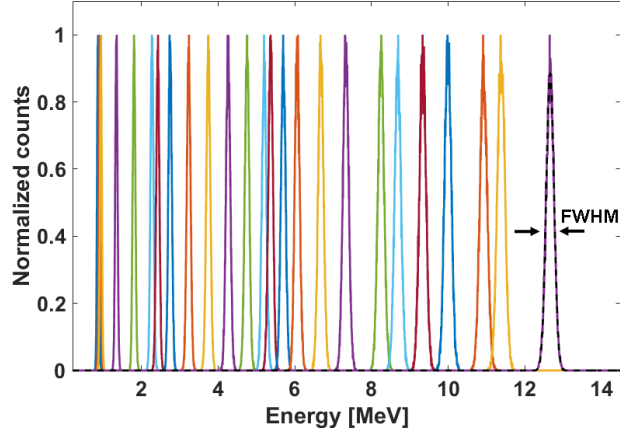
**Figure 5.15:**  Normalized energy spectra of the central SiPM of the tile as a function of energies simulated with the LED setup at 5 V of over-voltage.

and a electronic noise term.  This last term has two contributions:  the parallel contribution due to the DCR, and the estimated Equivalent Noise Charge (ENC) due to ASIC series and 1/f noise [122].  Experimental data follow the expected trend
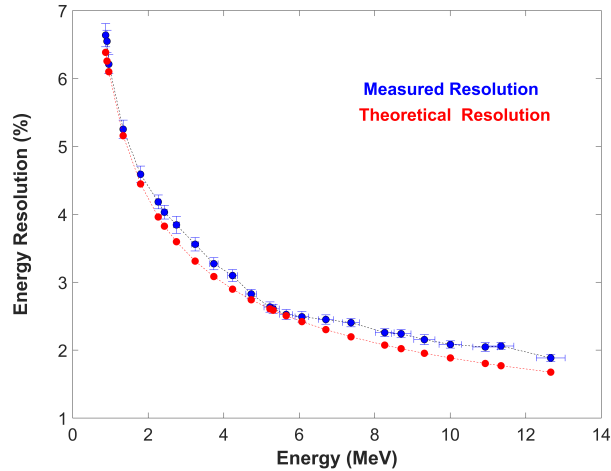


**Figure 5.16:**  Measured energy resolution as a function of the energy compared to a theoretical resolution.  Data of the theoretical resolution are provided by G.Cozzi.

and are in agreement with the theoretical values.  A difference between measured and theoretical resolution appears above 6 MeV, and has a maximum value of 0.3%. This difference should be attributed to the NL of the photo-detector system in high-energy condition, shown in Fig. 5.14.  From the data shown in Fig. 5.14 the NL of the GDM was estimated using the method presented in Sec. 3.2.2.  Fig. 5.17 shows

a comparison between this NL and the NL of a single SiPM tested with discrete electronics developed at FBK. The NL due to the SiPM saturation is significantly lower than the NL of the GDM, thus there is a source of NL in the readout chain. There are many factors involved in a readout chain and this phenomenon will be studied accurately in the future. However, the NL values is lower than 7% in the energy range for which the photo-detector is optimized (2-8 MeV). Furthermore, the photo-detection module has a satisfactory behaviour up to 13 MeV of energy with NL values lower than 15%.
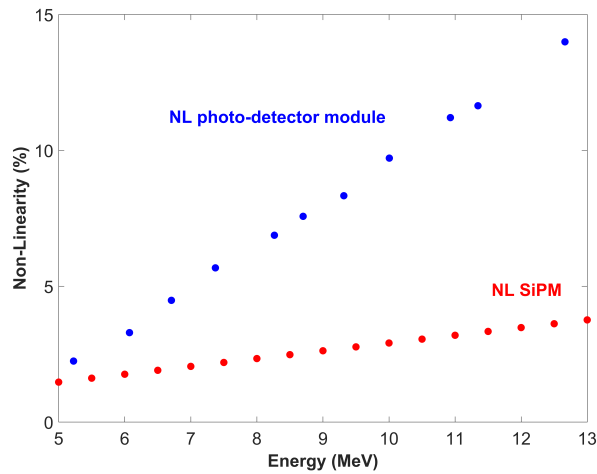


**Figure 5.17:** Non-linearity as a function of energy for the complete photo-detector module and for a single SiPM.

## 5.4   Results and future work

The previous sections present the results of the characterization of the photo-detector optimized for prompt gamma imaging, based on a photo-sensor of 64 SiPMs coupled to a pixelated LYSO crystal. Results show that the module has spectroscopic performance comparable to the state-of-the-art devices in PGI applications [37]; this allows an accurate energy calibration of the system, and a correct setting of two energy thresholds. The characterization of the module shows also a position sensitivity that matches the SiPM dimensions, in agreement with the system design and specifications. The study of the non-linear behaviour shows a proper acquisition of high-energy gamma-ray events from 800 keV to 13 MeV. Summarizing, these mea-

surements have proved that the module is suitable for PGI applications. At the time of writing this module has not yet been tested in a proton therapy facility. Later steps of the Gammarad project will plan a test of this photo-detector module in an experimental treatment room at the Proton therapy facility in Trento, in collaboration with the Gammarad project partners. Currently, the DAQ development is carried out by the Gammarad's partner of the Trento Institute for Fundamental Physics and Applications (TIFPA).

# Conclusion

The R&D activity carried out during this thesis has provided the final photo-detection module for the Gammarad project, with state-of-the-art performance for high-energy gamma-ray spectroscopy. The characterization of the module shows also a position sensitivity that matches the SiPM dimension, and a proper acquisition of high-energy gamma-ray events from 800 keV to 13 MeV. This module will be tested in an experimental treatment room at the Proton therapy facility in Trento by the partners of Gammarad project. The core of the photo-detection module is the photo-sensor based on silicon photomultipliers. The realization of this sensor requires several steps, which can be summarized into two parts.

The first part has focused on the selection of the most suitable SiPM technology for the photo-sensor. This selection was based on the requirement for prompt gamma imaging application, and for high-energy gamma-rays spectroscopy. These applications require a photo-sensor that has a high-dynamic range, and the capability to detect high-energy gamma-rays. In addition, detectors must be compact, robust, and insensitive to the magnetic field. They have to provide high performance in terms of spatial, temporal, and energy resolution. For their characteristics, SiPMs can satisfy all these requirements but typically they have been used with relatively low energy gamma rays and low photon flux, so manufacturers have optimized them for these conditions. Because of the limited number of micro-cells in a standard SiPM, 625 cells/mm$^2$ with 40 $\mu$m cells, the detector response is non-linear in high-energy conditions. Increasing the cell density is extremely important to improve the linearity of the SiPM, and to avoid the compression of the energy spectrum at high energies, which worsens the energy resolution and makes difficult the calibration of the detector. On the other hand, small cells provide a lower Photon Detection Efficiency (PDE) because of the lower Fill Factor (FF) and as a consequence a lower energy resolution. Summarizing, the energy resolution at high energies is a

trade-off between the excess noise factor (ENF) caused by the non-linearity of the SiPM and the PDE of the detector. Moreover, the small cell size provides an ultra-fast recovery time, in the order of a few of nanoseconds for the smallest cells. A short recovery time together with a fast scintillator such a LYSO, reduces pile-up in high-rate applications, such as PGI.

Based on the above considerations, SiPMs evaluated for the photo-sensor were High-Density (HD) and Ultra-High-Density (UHD) SiPM technologies, recently produced at Fondazione Bruno Kessler (FBK). Instead of standard SiPMs, HD and UHD SiPMs have a very small micro-cell pitch, from 30 $\mu$m down to 5 $\mu$m with a cell density from 1600 cells/mm$^2$ to 46190 cells/mm$^2$, respectively. Both these technologies were characterized in terms of photon detection efficiency, gain, dark count rate, and correlated noise.

The most important markers of SiPMs performance in gamma-ray spectroscopy are the energy resolution and the linearity. A typical characterization of the energy resolution of SiPMs, coupled to scintillator crystals, is performed with radioactive source up to 1.5 MeV. However, PGI features gamma ray-energies up to 15 MeV which are not easily provided by the usual laboratory calibration sources. Extrapolating the behaviour of the detector from the "low" energy data is not correct and leads to unreliable data for calibration and performance estimation. Therefore, it was developed a setup that simulates the LYSO light emission in response to gamma photons up to 30 MeV. A LED (emitting at 420 nm) is driven by a pulse generator, emulating the light emitted by a LYSO scintillator when excited by gamma rays. The photon number in each light pulse is calibrated from the measurements at 511 keV, obtained with a $^{22}$Na source and a LYSO crystal coupled to the SiPM. Using this LED setup, the energy resolution and non-linearity of SiPMs in high-energy gamma-ray conditions were characterized. Furthermore, combining the results of the LED setup with the results of the scintillator setup, can be distinguished different components of the energy resolution (intrinsic, statistical, detector and electronic noise). Currently, this LED setup for the simulation of high-energy gamma-ray response is used to characterize and calibrate the response of SiPMs produced at Fondazione Bruno Kessler (FBK).

Summarizing the results, the lowest non-linearity is provided by the technology with highest cell density, the UHD technology. Instead, the best energy resolution is provided by largest SiPM cells of the HD technology. This is due to the dependence

of the energy resolution on the photon detection efficiency, which increases with the size of the SiPM cell. Optimal performance of the detector in high-dynamic-range applications, which depends on several SiPM parameters, such as excess noise factor, photon detection efficiency, and cell sizes of the SiPM, is a trade-off between non-linearity and energy resolution. At 5 MeV, the best trade-off for prompt gamma imaging application is obtained with the 15 $\mu$m-cell of the HD-SiPMs. At 10 MeV the 12.5 $\mu$m-cell of the UHD-SiPMs provides the best trade-off, because of the higher number of photons emitted by the scintillator. Thus, UHD-SiPMs are very promising for gamma-ray spectroscopy at energies above 10 MeV. Furthermore, a recent development of UHD-SiPM improves the PDE in comparison with the UHD-SiPM version tested in this work. This improvement of the PDE is a good premise for further improvement of UHD performance in high-energy gamma-ray spectroscopy, that will be evaluated in the future.

The second part of the thesis has focused on the production of the photo-detector module of the prompt gamma camera with the chosen SiPM technology. This production requires research on packaging techniques to solve two main challenges: the maximization of the photo-sensitive area and the application of a protective resin, transparent in the near UV to maximize light collection from the LYSO. After some R&D on packaging, it was obtained a fully functional tile with 64 SiPMs with a fill factor, i.e. the ratio between the photo-sensitive area and the total area, of ~86%. This fill factor is comparable to the values obtained when a Through Silicon Vias (TSVs) technique is used to connect SiPMs but without the high production cost and the additional fabrication process complexity of the TSV. It should be highlighted that packaging operations are very critical because it is necessary to produce a tile with all working SiPMs, since defective items can not be replaced in the tile. Currently, in the packaging laboratory of the Integrated Radiation and Image Sensors group at Fondazione Bruno Kessler (Trento, Italy), some of the packaging techniques developed for this thesis are used to produce photo-sensor tiles for several experiments in gamma-ray spectroscopy, high-energy physics, and astrophysics.

Global performance of the photo-detector, based on 64 RGB-HD SiPMs and 64 LYSO crystals with a 1:1 coupling, was tested in order to verify its capability for PGI applications. The energy resolution and the position sensitivity of the photo-detector were measured using radioactive sources with energy of up to 1.3 MeV. Instead, the energy resolution and the non-linearity of the photo-detector (without pixelated

LYSO crystal) at high-energy gamma-ray conditions, were tested with the LED setup which was developed to simulate the LYSO light emission in response to gamma photons up to 30 MeV. The measurement results show that the module has an energy resolution of ∼13% at 622 keV and 9% at 1173 keV. These values are comparable to the state-of-the-art performance in PGI applications; this allows an accurate energy calibration of the system, and a correct setting of two energy thresholds. The characterization of the module shows also a position sensitivity that matches the SiPM dimensions, in agreement with the system design and specifications. The study of the non-linear behaviour shows a proper acquisition of high-energy gamma-ray events from 800 keV to 13 MeV. Summarizing, these measurements have proved that in principle the module is suitable for PGI applications. However, at the time of writing this module has not yet been tested in clinical conditions. This step is necessary to validate the laboratory characterization at high-energy conditions and for a better understanding of the detector behaviour. These measurements are being currently planned in collaboration with the Proton therapy facility in Trento, and will be carried out in the following months.

# Bibliography

[1] H. Paganetti, ed., *Proton Therapy Physics*. CRC Press Taylor & Francis Group, 2012.

[2] R. Wilson, "Radiological use of fast protons," *Radiology*, vol. 47, p. 487, 1946.

[3] A. Knopf and A. Lomax, "In vivo proton range verification: a review," *Phys. Med. Biol.*, vol. 58, pp. R131–R160, 2013.

[4] U. Schneider and E. Pedroni, "The calibration of ct hounsfield units for radiotherapy treatment planning," *Phys. Med. Biol.*, vol. 41, p. 111, 1996.

[5] M. Moyers *et al.*, "Methodologies and tools for proton beam design for lung tumors," *Int. J. Radiat. Oncol. Biol. Phys.*, vol. 49, p. 1429, 2001.

[6] H. Paganetti, "Range uncertainties in proton therapy and the role of monte carlo simulations," *Phys. Med. Biol.*, vol. 57, pp. R99–R117, 2012.

[7] H. Lu, "A potential method for in vivo range verification in proton therapy treatment," *Phys. Med. Biol.*, vol. 53, p. 1413, 2008.

[8] B. Gottschalk *et al.*, "Water equivalent path length measurement in proton radio- therapy using time resolved diode dosimetry," *Phys. Med. Biol.*, vol. 38, p. 2282, 2011.

[9] M. Mumot *et al.*, "Proton range verification using a range probe: definition of concept and initial analysis," *Phys. Med. Biol.*, vol. 55, p. 4771, 2010.

[10] K. Yajima *et al.*, "Development of a multi-layer ionization chamber for heavy-ion radiotherapy," *Phys. Med. Biol.*, vol. 54, pp. N107–N114, 2009.

[11] U. Schneider and E. Pedroni, "Proton radiography as a tool for quality control," *Med. Phys.*, vol. 22, pp. 353–363, 1995.

[12] S. Penfold *et al.*, "A more accurate reconstruction system matrix for quantitative proton computed tomography," *Med. Phys.*, vol. 36, pp. 4511–4518, 2009.

[13] M. Studenski and Y. Xiao, "Proton therapy dosimetry using positron emission tomography," *World J. Radiol.*, vol. 2, pp. 135–142, 2010.

[14] C. Min *et al.*, "Prompt gamma measurements for locating the dose fall-off region in the proton therapy," *Appl. Phys. Lett.*, vol. 89, p. 183517, 2006.

[15] S. Stevens *et al.*, "Early and late bone-marrow changes after irradiation: Mr evaluation," *Am. J. Roentgenol.*, vol. 154, pp. 745–750, 1990.

[16] M. Gensheimer *et al.*, "In vivo proton beam range verification using spine mri changes," *Int. J. Radiat. Oncol. Biol. Phys.*, vol. 78, pp. 268–275, 2010.

[17] K. Parodi *et al.*, "Patient study of in vivo verification of beam delivery and range, using positron emission tomography and computed tomography imaging after proton therapy," *Int. J. Radiat. Oncol. Biol. Phys.*, vol. 68, pp. 920–934, 2007.

[18] K. Parodi *et al.*, "Experimental study on the feasibility of in-beam pet for accurate monitoring of proton therapy," *IEEE Trans. Nucl. Sci.*, vol. 52, p. 778, 2005.

[19] F. Sommerer *et al.*, "In-beam pet monitoring of monoenergetic (16)O and (12)C beams: experiments and fluka simulations for homogeneous targets," *Phys. Med. Biol.*, vol. 54, pp. 3979–3996, 2009.

[20] A. Knopf *et al.*, "Quantitative assessment of the physical potential of proton beam range verification with pet/ct," *Phys. Med. Biol.*, vol. 53, pp. 4137–4151, 2008.

[21] A. Knopf *et al.*, "Accuracy of proton beam range verification using post-treatment positron emission tomography/computed tomography as function

of treatment site," *Int. J. Radiat. Oncol. Biol. Phys.*, vol. 79, pp. 297–304, 2011.

[22] F. Stichelbaut and Y. Jongen, "Verification of the proton beam position in the patient by the detection of prompt gamma-rays emission," *39ᵗʰ Meeting of the Particle Therapy Co-Operative Group*, 2003.

[23] B. Koslovsky *et al.*, "Nuclear deexcitation gamma-ray lines from accelerated particle interactions," *Astrophys. J.Suppl. Ser.*, vol. 141, pp. 523–541, 2002.

[24] D. Prieels *et al.*, "Towards a practical solution for real-time measurement of the proton beam range in patients," *50ᵗʰ Meeting of the Particle Therapy Co-Operative Group*, 2011.

[25] C. Min *et al.*, "Prompt gamma measurements for locating the dose fall-off region in the proton therapy," *Appl. Phys. Lett.*, vol. 89, 2006.

[26] J. Verburg *et al.*, "Energy- and time-resolved detection of prompt gamma-rays for proton range verification," *Phys. Med. Biol.*, vol. 58, pp. L37–L49, 2013.

[27] F. Roellinghoff *et al.*, "Real- time proton beam range monitoring by means of prompt-gamma detection with a collimated camera," *Phys. Med. Biol.*, vol. 59, pp. 1327–1338, 2014.

[28] J. Smeets *et al.*, "Prompt gamma imaging with a slit camera for real-time range control in proton therapy," *Phys. Med. Biol.*, vol. 57, pp. 3371–3405, 2012.

[29] J. Smeets, *Prompt gamma imaging with a slit camera for real time range control in particle therapy.* PhD thesis, Universite Libre de Bruxelles, 2012.

[30] V. Bom *et al.*, "Real-time prompt gamma monitoring in spot-scanning proton therapy using imaging through a knife-edge-shaped slit," *Phys. Med. Biol.*, vol. 57, pp. 297–308, 2012.

[31] C. Min *et al.*, "Development of array-type prompt gamma measurement system for in vivo range verification in proton therapy," *Med. Phys.*, vol. 39, pp. 2100–2107, 2012.

[32] G. Phillips *et al.*, "Gamma-ray imaging with compton cameras," *Nucl. Instr. Meth. Phys. Res.*, vol. 99, pp. 674–677, 1995.

[33] M. Richard *et al.*, "Design guidelines for a double scattering compton camera for prompt gamma imaging during ion beam therapy: a monte carlo simulation study," *Trans. Nucl. Sci.*, vol. 58, pp. 87–94, 2011.

[34] F. Hueso-Gonzalez *et al.*, "Test of compton camera components for prompt gamma imaging at the elbe bremsstrahlung beam," *JINST*, vol. 9, p. P05002, 2014.

[35] T. Kormoll *et al.*, "Compton imaging in a high energetic photon field," in *2013 IEEE Nuclear Science Symposium and Medical Imaging Conference*, 2013.

[36] E. Muñoz *et al.*, "Performance evaluation of MACACO: a multilayer Compton camera," *Phys. Med. Biol.*, vol. 62, pp. 7321–7341, 2017.

[37] P. Perali *et al.*, "Prompt gamma imaging of proton pencil beams at clinical dose rate," *Phys. Med. Biol.*, vol. 59, pp. 5849–5871, 2014.

[38] P. Lopes *et al.*, "Time-resolved imaging of prompt-gamma rays for proton range verification using a knife-edge slit camera based on digital photon counters," *Phys. Med. Biol.*, vol. 60, pp. 6063–6085, 2015.

[39] J. Polf *et al.*, "Measurement of characteristic prompt gamma rays emitted from oxygen and carbon in tissue-equivalent samples during proton beam irradiation," *Phys. Med. Biol.*, vol. 58, pp. 5821–5831, 2013.

[40] A. Biegun *et al.*, "Time-of-flight neutron rejection to improve prompt gamma imaging for proton range verification: a simulation study," *Phys. Med. Biol.*, vol. 57, pp. 6429–6444, 2012.

[41] F. Roellinghoff *et al.*, "Real-time proton beam range monitoring by means of prompt-gamma detection with a collimated camera," *Phys. Med. Biol.*, vol. 59, pp. 1327–1338, 2014.

[42] "Gammarad Project," www.gammarad.fbk.eu.

[43] "Fondazione Bruno Kessler (FBK)," www.fbk.eu.

[44] "Politecnico di Milano - Dipartimento di Elettronica, Informazione e Bioingegneria - (DEIB)," www.deib.polimi.it.

[45] "Trento Institute for Fundamental Physics and Applications (TIFPA)," www.tifpa.infn.it/.

[46] "Protonterapia," www.protonterapia.provincia.tn.it.

[47] D. Renker, "Geiger-mode avalanche photodiodes, history, properties and problems," *Nucl. Instrum. Meth. A*, vol. 567, pp. 48–56, 2006.

[48] C. Piemonte, V. Regazzoni, *et al.*, "Performance of NUV-HD silicon photomultiplier technology," *IEEE Trans. Electron Devices*, vol. 63, pp. 1111–1116, 2016.

[49] A. Ferri *et al.*, "Performance of a 64-channel, 3.2x3.2 cm$^2$ SiPM tile for TOF-PET application," *Nucl. Instrum. Meth. A*, vol. 824, pp. 196–197, 2016.

[50] S. Gundacker *et al.*, "State of the art timing in TOF-PET detectors with LuAG, GAGG and L(Y)SO scintillators of various sizes coupled to FBK-SiPMs," *JINST*, vol. 11, p. P08008, 2016.

[51] P. Bohn *et al.*, "Radiation damage studies of silicon photomultipliers," *Nucl. Instrum. Meth. A*, vol. 598, pp. 722–736, 2009.

[52] D. Townsted *et al.*, "Multimodality imaging of structure and function," *Phys. Med. Biol.*, vol. 53, pp. R1–R39, 2008.

[53] C. V. Eijk *et al.*, "Radiation detector developments in medical applications: inorganic scintillators in positron emission tomography," *Radiat. Protect. Dosimetry*, vol. 129, pp. 13–21, 2008.

[54] A. Berra *et al.*, "Shashlik Calorimeters With Embedded SiPMs for Longitudinal Segmentation," *IEEE Trans. on Nuclear Science*, vol. 64, pp. 1056–1061, 2017.

[55] G. Ambrosi *et al.*, "Large size SiPM matrix for Imaging Atmospheric Cherenkov Telescopes applications," *Nucl. Intrum. Meth. A*, vol. 824, pp. 125–127, 2016.

[56] A. D. Mora *et al.*, "Towards next-generation time-domain diffuse optics for extreme depth penetration and sensitivity," *Biomedical Optics Express*, vol. 6, pp. 1749–1760, 2015.

[57] S. Vinogradov *et al.*, "Performance of X-ray detectors with SiPM readout in cargo accelerator-based inspection systems," in *2013 IEEE Nuclear Science Symposium and Medical Imaging Conference*, 2013.

[58] "Centre for Materials and Microsystems (CMM)," www.cmm.fbk.eu/.

[59] "Integrated Radiation and Image Sensors (IRIS) Group (FBK)," www.iris.fbk.eu.

[60] F. Zappa *et al.*, "Principles and features of single-photon avalanche diode arrays," *Sens. Actuators A*, vol. 140, pp. 103–112, 2007.

[61] S. Cova *et al.*, "Avalance photodiodes and quenching circuits for single-photon detection," *Appl. Opt.*, vol. 35, pp. 1956–1976, 1996.

[62] V. Golovin, "Patent no. RU 2142175," 1998.

[63] Z. Sadygov, "Patent no. RU 2102820," 1998.

[64] R. McIntyre, "Theory of microplasma instability in silicon," *J. Appl. Phys.*, vol. 32, pp. 983–995, 1961.

[65] R. Haitz, "Model for the electrical behavior of a microplasma," *J. Appl. Phys.*, vol. 35, pp. 983–995, 1964.

[66] S. Seifert *et al.*, "Simulation of Silicon Photomultiplier Signals," *IEEE Trans. on Nuclear Science*, vol. 56, pp. 3726–3733, 2009.

[67] H. Otono *et al.*, "Study of MPPC at Liquid Nitrogen Temperature," in *International Workshop on new Photon-Detectors*, 2007.

[68] S. Sze *et al.*, *Physics of Semiconductor Devices*, ch. p-n Junctions, pp. 102–112. Springer, $3^{rd}$ ed., 2007.

[69] "Pveducation," www.pveducation.org.

[70] W. Oldham *et al.*, "Triggering phenomena in avalanche diodes," *IEEE Trans. Electron Devices*, vol. 19, pp. 1056–1060, 1972.

[71] R. V. Overstraeten and H. D. Man, "Measurement of the ionization rates in diffused silicon p-n junctions," *Solid-State Electron.*, vol. 13, pp. 583–608, 1970.

[72] W. Grant, "Electron and hole ionization rates in epitaxial silicon at high electric fields," *Solid-State Electron.*, vol. 16, pp. 1189–1203, 1973.

[73] C. Piemonte *et al.*, "A new Silicon Photomultiplier structure for blue light detection," *Nucl. Instrum. Meth. A*, vol. 568, pp. 224–232, 2006.

[74] N. Serra *et al.*, "Characterization of new FBK SiPM technology for visible light detection," *JINST*, vol. 8, p. P03019, 2013.

[75] F. Acerbi, V. Regazzoni, *et al.*, "High-Density Silicon Photomultipliers for high efficiency and dynamic-range applications," *Submitted on Photonics Technology Letters*, 2017.

[76] F. Acerbi, V. Regazzoni, *et al.*, "High Efficiency, Ultra high-density Silicon Photomultipliers," *IEEE Journal of Selected Topics in Quantum Electronics*, vol. 24, pp. 1–8, 2018.

[77] T. Pro *et al.*, "New Developments of Near-UV SiPMs at FBK," *Nucl. Instrum. Meth. A*, vol. 60, pp. 2247–2253, 2013.

[78] F.Acerbi *et al.*, "First Silicon Photomultipliers and Single-photon Avalanche Diodes with Enhanced NIR Detection Efficiency at FBK," in *New Developments in Photodetection 2017 (NDIP)*, 2017.

[79] C. Rethmeier, "Characterization of VUV sensitive SiPMs for nEXO," *JINST*, vol. 11, p. C03002, 2016.

[80] G. Zappalà *et al.*, "Set-up and methods for SiPM photo-detection efficiency measurements," *JINST*, vol. 11, p. P08014, 2016.

[81] G. Zappalà, V. Regazzoni, *et al.*, "Study of the photo-detection efficiency of FBK High-Density silicon photomultipliers," *JINST*, vol. 11, p. P11010, 2016.

[82] S. Yang *et al.*, "Precision measurement of the photon detection efficiency of silicon photomultipliers using two integrating spheres," *Opt. Express*, vol. 22, pp. 716–726, 2014.

[83] G. Bonanno *et al.*, "Precision measurement of Photon Detection Efficiency for SiPM detectors," *Nucl. Instrum. Meth. A*, vol. 610, pp. 93–97, 2009.

[84] P. Eckert *et al.*, "Characterisation studies of silicon photomultipliers," *Nucl. Instrum. Meth. A*, vol. 620, pp. 217–226, 2010.

[85] W. Shockley and W. T. Read, "Statistics of the Recombinations of Holes and Electrons," *Phys. Rev.*, vol. 87, pp. 835–842, 1952.

[86] W. Kindt, *Geiger Mode Avalanche Photodiode Arrays*. PhD thesis, Technische Universiteit Delft, 1999.

[87] A. Lacaita *et al.*, "On the bremsstrahlung origin of hot-carrier-induced photons in silicon devices," *IEEE Trans. Electron Devices*, vol. 40, pp. 577–582, 1993.

[88] P. Buzhan *et al.*, "The cross-talk problem in SiPMs and their use as light sensors for imaging atmospheric Cherenkov telescopes," *Nucl. Instrum. Meth. A*, vol. 610, pp. 131–134, 2009.

[89] C. Piemonte *et al.*, "Development of an automatic procedure for the characterization of silicon photomultipliers," in *2012 IEEE Nuclear Science Symposium and Medical Imaging Conference*, 2012.

[90] A. Gola *et al.*, "The DLED Algorithm for Timing Measurements on Large Area SiPMs Coupled to Scintillators," *IEEE Trans. on Nuclear Science*, vol. 59, pp. 358–365, 2012.

[91] F. Acerbi *et al.*, "Characterization of Single-Photon Time Resolution: From Single SPAD to Silicon Photomultiplier," *IEEE Trans. on Nuclear Science*, vol. 61, pp. 2678–2686, 2014.

[92] S. Seifert *et al.*, "The lower bound on the timing resolution of scintillation detectors," *Phys. Med. Biol.*, vol. 57, pp. 1797–1814, 2012.

[93] M. V. Nemallapudi *et al.*, "Sub-100 ps coincidence time resolution for positron emission tomography with LSO:Ce codoped with Ca," *Phys. Med. Biol.*, vol. 60, pp. 4635–4649, 2015.

[94] F. Acerbi, "Development of Ultra-High-Density (UHD) Silicon Photomultipliers with improved Detection Efficiency," in *12$^{th}$ Trento Workshop On Advanced Silicon Radiation Detectors (TREDI2017)*, 2017.

[95] G. F. Knoll, *Radiation detection and measurement.* John Wiley and Sons, 1979.

[96] "Nuclear Power," www.nuclear-power.net.

[97] "Saint-Gobain," www.crystals.saint-gobain.com.

[98] K. Kamanda *et al.*, "2 inch diameter single crystal growth and scintillation properties of Ce:$Gd_3Al_2Ga_3O_12$," *J. Cryst. Growth*, vol. 352, pp. 88–90, 2012.

[99] C. Melcher *et al.*, *Crystal growth and scintillation properties of the rare earth oxyorthosilicates*, pp. 309–316. Delft University Press, 1995.

[100] "Saint-gobain," www.crystals.saint-gobain.com/products/prelude-420-LYSO.

[101] M. Grodzicka *et al.*, "Energy resolution of scintillation detectors with SiPM light readout," *Nuclear Science Symposium Conference Record (NSS/MIC)*, pp. 1940–1948, 2010.

[102] M. Moszynski *et al.*, "Energy resolution of scintillation detectors," *SPIE proceedings*, vol. 5922, pp. 1–14, 2005.

[103] S.Vinogradov *et al.*, "Probability distribution and noise factor of solid state photomultiplier signals with cross-talk and afterpulsing," in *2009 IEEE Nuclear Science Symposium Conference Record*, pp. 1496–1500, 2009.

[104] S.Vinogradov *et al.*, "Performance of X-ray detectors with SiPM readout in cargo accelerator-based inspection systems," in *2013 IEEE Nuclear Science Symposium and Medical Imaging Conference*, 2013.

[105] V. Regazzoni *et al.*, "Characterization of High Density SiPM Non-linearity and Energy Resolution for Prompt Gamma Imaging Applications," *JINST*, vol. 12, p. P07001, 2017.

[106] P. Lecoq *et al.*, *Inorganic Scintillators for Detector Systems*, ch. Spectrometry of Low Energy $\gamma$-Quanta. Non-linearity of Scintillator Response, pp. 54–55. Springer, $2^{nd}$ ed., 2016.

[107] P. Lecoq *et al.*, *Inorganic Scintillators for Detector Systems*, ch. Non-proportionality of the Scintillator Response, pp. 188–190. Springer, $2^{nd}$ ed., 2016.

[108] P. Lecoq *et al.*, *Inorganic Scintillators for Detector Systems*, ch. Light collection, pp. 327–329. Springer, $2^{nd}$ ed., 2016.

[109] Y. A. Tsirlin, "Light collection in scintillators," *Atomizdat*, 1975.

[110] Y. A. Tsirlin *et al.*, "Optimization of gamma detection in scintillation crystals," *Energoatomizdat*, 1991.

[111] P. Dorenbos, "Light output and energy resolution of Ce3+-doped scintillators," *Nucl. Instrum. Meth. A*, vol. 486, pp. 208–213, 2002.

[112] I. G. Valais *et al.*, "Evaluation of the light emission efficiency of LYSO:Ce scintillator under X-ray excitation for possible applications in medical imaging," *Nucl. Instrum. Meth. A*, vol. 569, pp. 201–204, 2006.

[113] "Hilger LYSO(Ce) crystal data sheet," www.hilger-crystals.co.uk/materials-index/lutetium-yttrium-silicate.asp.

[114] C. Piemonte *et al.*, "Characterization of the First FBK High-Density Cell Silicon Photomultiplier Technology," *IEEE Trans. Electron Devices*, vol. 60, pp. 2567–2573, 2013.

[115] A. Gola *et al.*, "SiPM optical crosstalk amplification due to scintillator crystal: effects on timing performance," *Phys. Med. Biol.*, vol. 59, pp. 3615–3635, 2014.

[116] W. Chewpraditkul *et al.*, "Scintillation Properties of LuAG:Ce, YAG:Ce and LYSO:Ce Crystals for Gamma-Ray Detection," *IEEE Trans. Nucl. Sci.*, vol. 56, pp. 3800–3805, 2009.

[117] C. Wanarak *et al.*, "Luminescence and Scintillation Properties of Ce-Doped LYSO and YSO Crystals," *Advanced Materials Research*, vol. 199-200, pp. 1796–1803, 2011.

[118] F. Loignon-Houle *et al.*, "Simulation of scintillation light output in LYSO scintillators through a full factorial design," *Phys. Med. Biol.*, vol. 62, pp. 669–683, 2017.

[119] C. Levin, "Design of a High Resolution and High Sensitivity Scintillation Crystal Array with Nearly Perfect Light Collection," *IEEE Trans. on Nuclear Science*, vol. 49, pp. 2236–2243, 2002.

[120] P. Trigilio *et al.*, "ANGUS: A multichannel CMOS circuit for large capacitance silicon photomultiplier detectors for SPECT applications," in *2014 IEEE Nuclear Science Symposium and Medical Imaging Conference*, pp. 1–4, 2014.

[121] G. Cozzi, V. Regazzoni, *et al.*, "Development of a SiPM-based Detection Module for Prompt Gamma Imaging in Proton Therapy," in *2016 IEEE Nuclear Science Symposium and Medical Imaging Conference*, 2016.

[122] C.Fiorini, "Gamma detectors for spectroscopy and imaging based on scintillators coupled to semiconductor detectors," vol. 4141, pp. 97–110, 2000.

# List of publications

1. G. Gambarini, E. Massari, **V. Regazzoni**, D. Giove, A. Mirandola, M. Ciocca. *Study on corrections of dose images obtained with gafchromic EBT3 films for measurements in phantoms irradiated with proton beams.* Conference Paper of $4^{th}$ International Conference on Advancements in Nuclear Instrumentation Measurement Methods and their Applications (2015), DOI: 10.1109/AN-IMMA.2015.7465580.

2. G. Gambarini, **V. Regazzoni**, E. Artuso, D. Giove, A. Mirandola, M. Ciocca. *Measurements of 2D distributions of absorbed dose in protontherapy with Gafchromic EBT3 films.* Applied Radiation And Isotopes, $n^o104$ (2015), pp.192-196.

3. C. Piemonte, F. Acerbi, A. Ferri, A. Gola, G. Paternoster, **V. Regazzoni**, G. Zappalá, N. Zorzi. *Performance of NUV-HD Silicon Photomultiplier technology.* IEEE Transactions On Electron Devices, $n^o63$ (2016), pp.1111-1116.

4. G. Zappalá, F. Acerbi, A. Ferri, A. Gola, G. Paternoster, **V. Regazzoni**, N. Zorzi, C. Piemonte. *Study of the photo-detection efficiency of FBK High–Density silicon photomultipliers.* Journal of Instrumentation, $n^o11$ (2016), P11010.

5. Darkside collaboration. *The DarkSide experiment.* Nuovo Cimento della Societá Italiana di Fisica, $n^o40$ (2017).

6. F. Acerbi, A. Gola, **V. Regazzoni**, G. Paternoster, G. Borghi N. Zorzi, C. Piemonte. *Ultra-high cell-density Silicon photomultipliers with high detection efficiency.* Conference Paper of of SPIE-The International Society for Optical Engineering, (2017), DOI: 10.1117/12.2261966.

7. F. Acerbi, S. Davini, A. Ferri, C. Galbiati, A. Gola, A. Mandarano, A. Razeto, **V. Regazzoni**, D. Sablone, C. Savarese et al. *Cryogenic Characterization of the FBK NUV-HD SiPMs.* IEEE Transactions On Electron Devices, $n^o64$ (2017) pp.521-526.

8. **V. Regazzoni**, F. Acerbi, G. Cozzi, A. Ferri, C. Fiorini, G. Paternoster, C. Piemonte, D. Rucatti, G.Zappalá, N. Zorzi, A. Gola. *Characterization of High Density SiPM Non-linearity and Energy Resolution for Prompt Gamma Imaging Applications*, Journal of Instrumentation $n^o12$ (2017) P07001.

9. C.E. Aalseth, F. Acerbi, P. Agnes, **V.Regazzoni**, D. Sablone, C. Savarese et al. *Cryogenic Characterization of FBK RGB-HD SiPMs.* IEEE Transactions On Electron Devices, $n^o64$ (2017) pp.521-526.

10. G. Gambarini, D. Bettega, G. Camoni, M. Felisi, A. Gebbia, E. Massari, **V. Regazzoni**, I. Veronese, D. Giove, A. Mirandola, M. Ciocca. *Correction method of measured images of absorbed dose for quenching effects due to relatively high LET.* Radiation Physics and Chemistry, $n^o140$ (2017), pp.15-19.

11. F. Acerbi, A. Gola, **V. Regazzoni**, G. Paternoster, N. Zorzi, C. Piemonte. *High Efficiency, Ultra high density Silicon Photomultipliers.* IEEE Journal of Selected Topics in Quantum Electronics, $n^o24$ (2018), DOI:10.1109/JSTQE.2017. 2748927.

12. G. Cozzi, P. Busca, M. Carminati, G. L. Montagnani, C. Fiorini, F. Acerbi, A. Gola, **V. Regazzoni**, G. Paternoster, C. Piemonte, N. Blasi, F. Camera and

B. Million. *High-Resolution SiPM-Based Gamma-Ray Detection Module for 1" and 2" LaBr$_3$:Ce Spectroscopy.* Accepted for the publication on " Transactions on Nuclear Science" in August 2017.

13. F. Acerbi, A. Gola, **V. Regazzoni**, G. Paternoster, N. Zorzi, C. Piemonte. *High-Density Silicon Photomultipliers for high efficiency and dynamic-range applications.* Submitted in July 2017 on "Photonics Technology Letters".

14. Darkside collaboration. *DarkSide-20k: A 20 Tonne Two-Phase LAr TPC for Direct Dark Matter Detection at LNGS.* Submitted in August 2017 on "The European Physical Journal Plus".

15. F. Acerbi, A. Gola, **V. Regazzoni**, G. Paternoster, N. Zorzi, C. Piemonte. *High-Density Silicon Photomultipliers: performance and linearity evaluation for high efficiency and dynamic-range applications.* Submitted in November 2017 on "IEEE Journal of Quantum Electronics".